Stability Assessment of Inverter-fed Power Systems

Wang, Yanbo

DOI (link to publication from Publisher):
10.5278/vbn.phd.eng.00034

Publication date:
2017

Document Version
Publisher's PDF, also known as Version of record

STABILITY ASSESSMENT OF INVERTER-FED POWER SYSTEMS

BY
YANBO WANG

DISSERTATION SUBMITTED 2017

AALBORG UNIVERSITY
DENMARK

STABILITY ASSESSMENT OF INVERTER-FED POWER SYSTEMS

by

YANBO WANG

AALBORG UNIVERSITY
DENMARK

Dissertation submitted to
the Faculty of Engineering and Science at Aalborg University

for the degree of
Doctor of Philosophy in Electrical Engineering

.

Dissertation submitted: March2017

PhD supervisor: Prof. Zhe Chen,
Aalborg University

PhD committee: Professor Francesco Iannuzzo, (Chairman)
Aalborg University

Ralph M. Kennel,
Technische Universitaet Muenchen (Germany)

Dr. Don Tan
Senior staff manager and distinguished engineer
Northrop Grumman Corporation

PhD Series: Faculty of Engineering and Science, Aalborg University

ISSN (online): 2446-1636
ISBN (online): 978-87-7112-971-7

Published by:
Aalborg University Press
Skjernvej 4A, 2nd floor
DK – 9220 Aalborg Ø
Phone: +45 99407140
aauf@forlag.aau.dk
forlag.aau.dk

Printed in Denmark by Rosendahls, 2017

Mandatory page in Ph D thesis:

1. Thesis title:

   Stability Assessment of Inverter-Fed Power Systems

2. Name of PhD student.

   Yanbo Wang

3. Name and title of supervisor and any other supervisors.

   Supervisor: Zhe Chen, Professor;

4. List of published papers:

Paper 1: **Y. B. Wang**, X. Wang, F. Blaabjerg, and Z. Chen, "Harmonic instability assessment using state-space modeling and participation analysis in inverter-fed power systems," ***IEEE Transactions on Industrial Electronics***., vol. 64, no. 1, pp. 806-816, Jan, 2017.

Paper 2: **Y. B. Wang**, X. Wang, Z. Chen, and F. Blaabjerg, "Distributed Optimal Control of Reactive Power and Voltage in Islanded Microgrids," ***IEEE Transactions on Industrial Application***, vol. 53, no. 1, pp. 340-349, Jan, 2017.

Paper 3: **Y. B. Wang**, X. Wang, F. Blaabjerg, and Z. Chen, "Small-signal stability analysis of inverter-fed power systems using component connection method," ***IEEE Transactions on Smart Grid.*** (Early Access).

Paper 4: **Y. B. Wang**, Z. Chen, "Harmonic Resonance Assessment of Multiple Paralleled Grid-Tied Inverters system," ***IEEE Transactions on Power Electronics***. (Reviewing).

Paper 5: **Y. B. Wang**, X. Wang, F. Blaabjerg, and Z. Chen, "Eigenvalue-based harmonic stability analysis method in inverter-fed power systems," *in Proc. 41th Annu. Conf. IEEE Industrial Electronics Society*, 2015, pp. 3277-3282.

Paper 6: **Y. B. Wang**, X. Wang, Z. Chen, and F. Blaabjerg, "Distributed Optimal Control of Reactive Power and Voltage in Islanded Microgrids," *in Proc. Applied Power Electronics Conference and Exposition (APEC)*, pp.3431-3438, 20-24 Mar, 2016.

Paper 7: **Y. B. Wang**, X. Wang, F. Blaabjerg and Z. Chen, "Harmonic Stability Analysis of Inverter-Fed Power Systems Using Component Connection Method." *in Proc. of the 9th International Conference on Power Electronics – ECCE Asia* (ICPE 2016-ECCE Asia), June 1-June 5, Hefei, China. 2016.

Paper 8: **Y. B. Wang**, Z. Chen, and F. Deng, "Dynamic droop scheme considering effect of intermittent renewable energy source". *in Proc. 2016 IEEE 7th International Symposium on Power Electronics for Distributed Generation Systems*, 2016, pp. 1-6.

Paper 9: **Y. B. Wang**, X. Wang, Z. Chen, and F. Blaabjerg, "State-space-based harmonic stability assessment of paralleled grid-connected inverters system," *in Proc. 42th Annu. Conf. IEEE Industrial Electronics Society*, 2016.

Paper 10: **Y. B. Wang**, Z. Chen, X. Wang, and F. Blaabjerg, "Frequency scanning-based impedance stability criterion for grid-connected inverters system." T*he 10th International Conference on Power Electronics – ECCE Asia* (ICPE 2017-ECCE Asia). (Accepted).

Paper 11: **Y. B. Wang**, Z. Chen, X. Wang, and F. Blaabjerg, "Eigenvalue-based impedance stability analysis for multiple paralleled grid-tied inverters system." T*he 10th International Conference on Power Electronics – ECCE Asia* (ICPE 2017-ECCE Asia). (Accepted).

5. This present report combined with the above listed scientific papers has been submitted for assessment in partial fulfilment of the PhD degree. The scientific papers are not included in this version due to copyright issues. Detailed publication information is provided above and the interested reader is referred to the original published papers. As part of the assessment, coauthor statements have been made available to the assessment committee and are also available at the Faculty of Engineering and Science, Aalborg University.

ABSTRACT

As the increase of renewable energy utilization, the power electronic-enabled power plants such as wind farms and photovoltaic plants are becoming promising architectures to integrate renewable energy sources. However, the new emerging power electronic-fed power plants also give rise to potential challenges. Stability issue is matter of concern. The low frequency oscillation phenomenon may be caused by droop-based power controllers, constant power loads, and grid synchronization loop of grid-connected inverters. In addition, the interaction of the wideband control system of power converters with passive components maybe brings about in harmonic-frequency oscillation phenomena. These phenomena are challenging the system stability and power quality. Hence, it is essential to develop the modeling and analytical technique for the stability assessment of power electronic-fed power systems.

The aim of this project is to develop the stability assessment methods and reveal the oscillation mechanism of inverter-fed islanded power system as well as paralleled grid-connected inverters system. The main contents of this thesis are organized as following. Chapter1 introduces the motivation and background of this project. Also, the problem statements and structure of the thesis are described. Chapter 2 presents a state-space-based harmonic instability assessment method for inverter-fed power system, where the effect of time delay is considered in details. Furthermore, the participation analysis is developed to evaluate and identify the contributions of different components on harmonic-frequency oscillation modes. Chapter 3 develops a component connection method-based stability analytical approach to assess low frequency oscillation and high-frequency resonance of inverter-fed power systems. Chapter 4 develops a state-space-based impedance stability analytical method for paralleled grid-connected inverters system, where the resonance mechanism of paralleled inverters with grid-current feedback and converter-current feedback is investigated. In addition, a frequency scanning-based impedance analysis for stability assessment of grid-connected inverters system is presented, which can be easily performed for stability assessment without using the detailed mathematical model. Main conclusions of this project are drawn and future research topics are explained in Chapter 5.

The main contributions and conclusions are summarized as following. (1) The influence of time delay of digital controller on harmonic instability is considered in proposed stability analysis. (2) Participation analysis is adopted to assess and identify the contributions of different components on harmonic-frequency oscillation phenomenon. (3) The component connection method (CCM)-based small signal model of voltage-source inverters with multiple control loops is proposed, where the

frequency response and eigenvalue analysis explain the contributions of different control parameters on terminal characteristic in a wide frequency range. (4) A state-space-based impedance stability analysis for multiple paralleled grid-connected inverters system is presented, which establishes the bridge between the state-space-based modelling and impedance stability criterion, and combines the advanced merits of the two methods. Finally, the application of these stability analysis methods in different situations is demonstrated.

DANSK RESUME

I takt med at udnyttelsen af vedvarende energi forøges, bliver elektriske kraftværker såsom vindmølle- og solcelleparker mere attraktive at konstruere, som energiressource. Udviklingen indenfor den vedvarende energi skaber også visse udfordringer. Stabilitetsudfordringer i energisystemerne skaber blandt andet problemstillinger. Fænomener som lavfrekvente udsving kan skyldes reduceret energistyring, konstant energi belastninger og netværkssynkronisering loops forårsaget af vekselrettere i netværket. Interaktionen af de kontrolsystemer styret af radiobølger brugt til energi omformere med passive komponenter, vil muligvis resultere i harmonisk frekvensudsvingsfænomen. Disse fænomener skaber udfordringer for systemets stabilitet og energikvalitet. Af den grund er det afgørende at udvikle modellerings- og analyseteknikker for at vurdere stabiliteten af elektricitetsforsynende energisystemer.

Målet med dette projekt er at udvikle stabilitetsvurderingsmetoder og afklare udsvingsmekanismerne i isolerede energisystemer forsynet med vekselrettere såvel som paralleliserede vekselrettere i højspændingsnettet. Det hovedsaglige indhold af rapporten er struktureret på følgende måde: Det første kapitel introducere motivationen og baggrunden for projektet, desuden bliver problemformuleringen og strukturen af rapporten beskrevet. Andet kapitel præsenterer en tilstandsbaseret harmonisk ustabilitetsvurderingsmetode for energisystemer forsynet af vekselrettere, hvor indflydelsen af forsinkelse i tid er taget i betragtning. Derudover er en indflydelsesanalyse udarbejdet til at evaluere og identificere bidragene fra forskellige komponenter i harmoniske frekvenssvingninger. Kapitel tre skaber en komponentforbindelsesmetode baseret på analytisk stabilitetstilgang, til at vurdere lavfrekvente svingninger og højfrekvent resonans af energisystemer forsynet af vekselrettere. I fjerde kapitel udvikles en tilstandsbaseret impedans, udarbejdet med stabilitetsanalysemetode for paralleliserede forbundne vekselrettere på højspændingsnettet, hvor resonansmekanismen af paralleliserede vekselrettere med strømfeedback bliver undersøgt. Yderligere præsenteres en frekvensskanning baseret på impedansanalyse for stabilitets vurdering af vekselrettere på højspændingsnettet, som ubesværet kan fungere som en stabilitetsvurdering, uden brugen af detaljerede matematiske modeller. Hovedkonklusionen af dette projekt bliver udredt, og fremtidige forskningsemner bliver beskrevet i kapitel fem.

De hovedsaglige bidrag og konklusioner er opsummeret som følgende:(1) Indflydelsen af forsinkelse i tid i den digitale fjernbetjening på harmonisk ustabilitet er taget i betragtning i stabilitetsanalysen.(2) Deltagelsesanalysen tages i brug for at vurdere og identificere bidrag fra forskellige komponenter i harmonisk frekvenssvingningsfænomen.(3) Den CCM-baserede lav signal model af spændingskildens vekselrettere med flere kontrol loops foreslås, hvor frekvensrespons og egenværdianalyse forklarer bidrag fra forskellige kontrol

parametre på terminalkarakteristik i et bredt frekvensformat.(4) En tilstandsbaseret impedansstabilitetsanalyse for flere paralleliserede vekselretter systemer i højspændingsnettet bliver præsenteret, hvilket skaber en sammenkobling mellem tilstandsbaseret modellering og impedansstabilitetskriterium, og kombinerer de teknologiske fremskridt i de to verdener. Endeligt bliver applikationsmulighederne for disse stabilitetsanalysemetoder i forskellige situationer demonstreret.

ACKNOWLEDGEMENTS

I would like to thank the Danish Council for Strategic Research for providing the financial support under the project ‘‘Development of a Secure, Economic and Environmentally-friendly Modern Power System’’ (DSF 09-067255), and the project HIGHE. Also, I would like to acknowledge the financial support from Aalborg University and Otto Mønsteds Fond for conference participation and study abroad.

The research project was performed under the supervision of Prof. Zhe Chen in the Department of Energy Technology, Aalborg University, Denmark. I would like to express the sincere gratitude to my supervisor Prof. Zhe Chen, who is a smart and trusted supervisor throughout my Ph. D research. I would like to thank Prof. Frede Blaabjerg and Dr. Xiongfei Wang. They have given me huge supports and contributions for my Ph. D project.

My Ph. D project was done in the help of many colleagues in the Department of Energy Technology, Aalborg University, Denmark. I would like to give my sincere acknowledgement to my friends Mr. Zhen Xin. He gives me huge guidance and encouragements for my Ph. D project, and helps me to overcome the difficulties in my hard times, so that I can make the rapid progress in my project.

Also, I would like to acknowledge my friend Dr. Yanjun Tian, he gave me the great supports and helps for experiment implementation.

I would like to acknowledge the huge supports and helps from Prof. Ani Gole in Power System Research Group, University of Manitoba, Canada during my study abroad.

Many thanks are given to my colleagues Dr. Rafael, Dr. Zian Qin, Dr. Fujin Deng, Dr. Dan Wu, Dr. Huai Wang, Dr. Yi Tang, Dr. Yongheng Yang for their kind supports.

Sincere gratitude and wishes are given to my colleagues and friends Dr. Chi Su, Dr. Jiakun Fang, Dr. Weihao Hu, Dr. Dao Zhou, Dr. Chao Wang, Dr. Zhou Fan, Dong Liu, Rui Hu, QingSong Wang, Rui Wu, Ming Huang, Lexuan Meng, and other friends. My sincere acknowledgement is also given to Corina, Tina, Eva Janik, Walter, Mads and Frunk for their supports and assistances during my Ph. D study period.

Finally, the sincere acknowledgements are given to my parents, and my brother for their endless love and support.

Yanbo Wang

November, 2016
Department of Energy Technology, Aalborg University
Aalborg Øst, Denmark

LIST OF ACRONYMS

ADN Active Distribution Network

CPL Constant Power Load

DG Distributed Generation

DQ Direct Quadrature

HVDC High Voltage Direct Current

MMC Multi-level Modular Converter

PCC Point of Common Coupling

PI Proportional Integral

PV Photovoltaic

PWM Pulse Width Modulation

PM Phase Margin

LIST OF ACRONYMS

K_{pv} Proportional gain of PI Voltage Controller

K_{iv} Integral gain of PI Voltage Controller

K_{pc} Proportional gain of PI Current Controller

K_{ic} Integral gain of PI Current Controller

L_{fi} Inverter-side Filter Inductor

L_{ci} Grid-side Filter Inductor

C_{fi} Filter Capacitor

i_{abc} Output current of three phase inverter

i_{abc}^{*} Command current of three phase inverter

i_{ldqi} Converter-side current of *i*-th inverter in *dq*-frame

v_{oi} Output voltage of *i*-th inverter

i_{oi} Output current of *i*-th inverter

v_{odqi} Output voltage of *i*-th inverter in *dq*-frame

i_{odqi} Output current of *i*-th inverter in *dq*-frame

v^{*}_{odqi} Output voltage demand of *i*-th inverter in *dq*-frame

i^{*}_{ldqi} Output current demand of *i*-th inverter in *dq*-frame

v^{*}_{i} Reference voltage of modulator

v_i Output voltage of inverter

φ_{dqi} State variable of voltage controller of *i*-th inverter in *dq*-frame

γ_{dqi} State variable of current controller of *i*-th inverter in *dq*-frame

τ Delay time of control system

v_{bi} Voltage at *i*-th bus

v_{bDQi} Voltage at *i*-th bus in *DQ*-frame

R_{Loadi} The resistance value of *i*-th load

L_{Loadi} The inductance value of *i*-th load

R_{Linei} The resistance value of *i*-th line

L_{Linei} The inductance value of *i*-th line

i_{Loadi} The *i*-th load current

i_{Linei} The *i*-th line current

T_{s} Sampling period of digital control system

f_{s} Sampling frequency of digital control system

p_i Instantaneous active power

q_i Instantaneous reactive power

P_i Average active power

Q_i Average reactive power

ω_c Cut-off frequency of low-pass filter

m_{pi} Active power droop coefficient of *i*-th DG unit

n_{qi} Reactive power droop coefficient of *i*-th DG unit

ω_i Angle frequency of output voltage of *i*-th inverter

TABLE OF CONTENTS

TABLE OF FIGURES

operation. (d) The A-Phase output currents (10A/div) of inverters when inverter 2 is connected to grid. (e) The A-Phase output currents (10A/div) of inverters when inverter 3 is connected to grid.

Fig. 4-32. The experimental results of paralleled inverters with converter-current feedback. ($L_{f1}/L_{f2}/L_{f3}$=3mH/3mH/3mH, $C_{f1}/C_{f2}/C_{f3}$=5uF/10uF/10uF, $L_{c1}/L_{c2}/L_{c3}$=2.6mH/2.6mH/2.6mH) [112]. *(a) The A-phase current of inverters in stable case. (b) The A-phase current of 3 inverters if the 3th inverter operation with underdamping.*

CHAPTER 1. INTRODUCTION

This chapter primarily introduces the background and motivation of the Ph. D project, and state-of-art of the power electronics-fed power system is reviewed. Then, the objectives and contributions of this project are explained. Finally, the research layout and relationship among chapters are illustrated.

1.1 Background and motivation

With the increasing demand of electricity consumption and low-carbon economy, the renewable and clean energies such as wind energy, photovoltaic energy are being widely exploited to generate electricity energy. The exploration of renewable energy sources is critical element for human being substantial development. Renewable energy source is clean and inexhaustible energy that is able to minimize environmental pollution, and improve the reliability and flexibility of modern energy system. Because of government policies and incentives for non-fossil energy sources, renewable energy has become the fastest-growing energy source at an average rate of 2.6% per year throughout the world [1]. Nowadays, some magnificent goals have been planned throughout the world [1]-[2]. For example, the EUROPE 2020 [1] has been presented, which indicates the greenhouse gas emissions in 2020 will be 20% lower than that in 2012. Note that the 20% of electricity energy will be generated by renewable energy such as wind energy and photovoltaic energy. Fig. 1-1 shows the development trend of energies demand in future decades. It can be seen that the potential demand of renewable energies will be dramatically increased. Undoubtedly, the renewable energy power generation will play a critical role in modern power system.

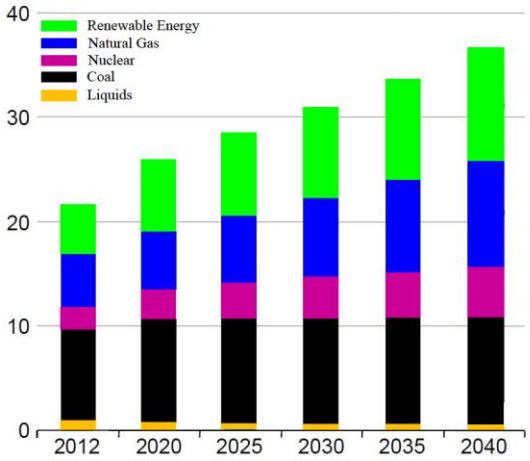

Fig.1-1 The development trend of renewable energies demand in future decades.

1.1.1 Renewable energy and its application

Renewable energy is a new emerging energy type that is extracted from natural resources such as wind energy, sunlight, hydro, hydrogen, biofuel, geothermal energy and so on. Renewable energy resources exist inherently in wide geographical areas. Rapid deployment of renewable energy promotes energy efficiency and economic benefits. As main types of renewable energy source, wind power, hydro power and photovoltaic power generation have been intensively studied and exploited throughout the world.

Wind power generation is main type of renewable energy source application. Wind power is generated by wind energy between wind turbines to power generators for power generation, and the power generators are connected into grid by power converters [3]. Wind energy production throughout the world is growing rapidly, and global wind power capacity expanded 16% to 369553 MW [4] in 2014. The large-scale exploration is being performed in many countries. It is reported from Navigant research that China is ranked a booming market for wind capacity growth and has the highest wind power generation capacity so far. The installed capacity in China will expand from 149 GW in 2015 to rough 495 GW by 2030 [4].

Hydro power also contributes to the renewable energy generation significantly. Hydro power is usually from the potential energy of dammed water driving a water turbine and generator. Hydropower has a good ability to increase the flexibility and stability of the electrical grid, and support the integration of intermittent renewable resources like wind energy and solar energy. Hydropower has been widely utilized in 150 countries. In 2015, hydropower contributes to 16.6% of the total electricity consumption and 70% of all renewable electricity throughout the world, and the hydropower was expected to increase about 3.1% each year for the following 25 years [5].

Photovoltaics power generation also plays an important role in renewable energy generation, where the conversion of sunlight into electricity is implemented by using photovoltaic panel. PV generation as an environment-friendly solution has been intensively addressed. Photovoltaics generation is growing rapidly and worldwide installed capacity reached at least 177 GW by the end of 2014 [6]. It is reported that the total power output of the world's PV capacity is beyond 200 TWh of electricity. After hydro and wind power, the photovoltaic generation has become the third most important renewable energy source.

Apart from renewable energy-based power generation, renewable energies also have been exploited in other fields [7]-[9] such as transportation and heating/cooling supply. For example, a hydrogen fuel cell-driven electric locomotive has been used in railway transportation [7], where the hydrogen energy is utilized as tractive force and no any carbon emission is generated. Also, heat pump has been adopted as an

energy-efficient way to provide heating and cooling [8], which collected renewable heat source in our surroundings. It extracts heat from a source and concentrates it to obtain a high temperature and applies to water for domestic heating.

1.1.2 Power electronics-based power system

Compared with the conventional fossil fuel-dominated power plant, the renewable energy-dominated power plant such as wind farm and PV plant has become a promising way to provide electricity energy. Different with the conventional synchronous generator in power system, the power electronic devices tend to dominate the renewable energy-based power plant. Power converters, as an efficient interface between the energy sources and power system, are playing an important role in power conversion and power generation. For example, in wind power generation system, the AC-DC and DC-AC power converter establishes the bridge between the wind generator and power grid. In photovoltaic generation system, the DC-DC and DC-AC power converters are adopted to convert the photovoltaic energy into power grid. A general diagram of power electronic-fed distributed generator is shown as Fig. 1-2.

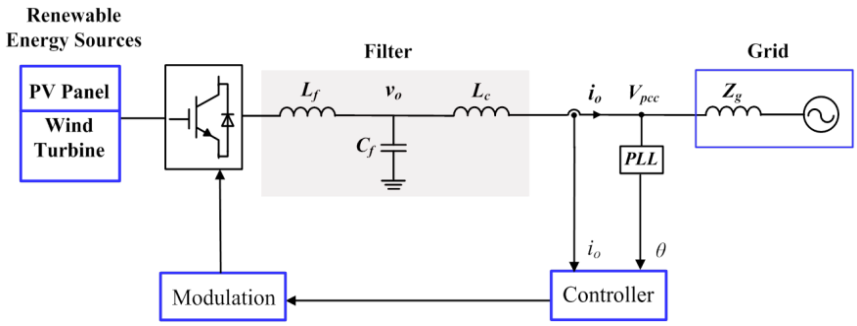

Fig.1-2 The block diagram of power electronic-fed distributed generator.

As the increasing exploitation of renewable energies, the power electronic-enabled power systems [10]-[16] such as microgrid, virtual power plants and so on have become promising architectures for future active distribution networks. These emerging power system structures are able to combine various renewable energies and improve the efficiency of electricity services [16]. Fig. 1-3 shows a diagram of power electronic-fed power system, which consists of wind generator, photovoltaic panel, power converter, *LC* filters and local loads.

However, the emerging power electronic-fed power plants also pose potential challenges. Stability issue is one of main challenges. Instability phenomenon of power electronics-fed power system in different frequency range have been intensively reported in renewable energy systems [17]-[28], which are challenging the system stability and power quality. Hence, it is essential to explore the modeling

and analytical techniques for dealing with the stability issues in power electronic-fed power systems.

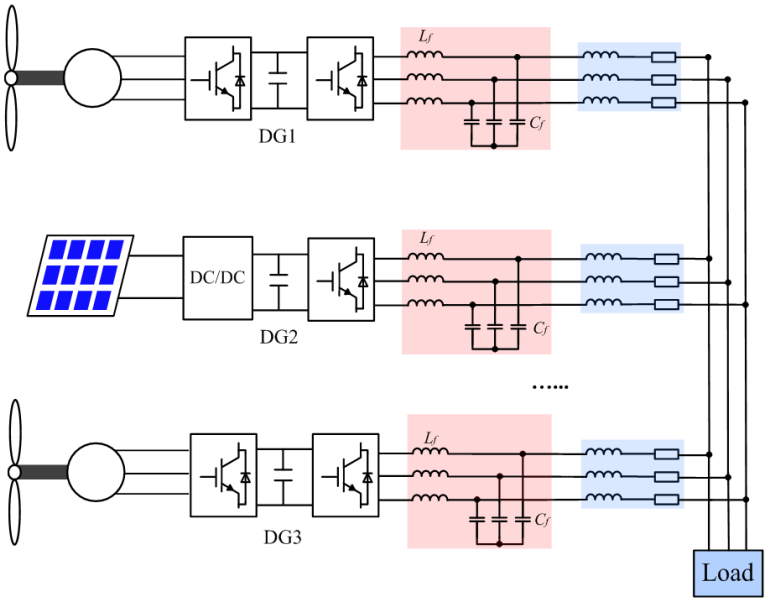

Fig. 1-3 The diagram of power electronic-enabled power system.

Therefore, the main objective of this project is to develop the stability assessment methods of inverter-fed power system, and reveal the root causes of oscillation phenomenon in different frequency range.

1.2 Stability concept and issues

1.2.1 Stability definition and issues in power system

Power system stability [29]-[31] is defined as the ability of system given an initial operating condition to regain a state of operating equilibrium after being subjected to a disturbance. Power system stability can be classified as rotor angle stability, frequency stability and voltage stability according to physical nature of the root cause of instability. Fig. 1-4 shows the basic classification of power system stability.

Rotor angle stability [29] means the ability of synchronous generators of an interconnected power system to remain in synchronism after being subjected to a disturbance. Rotor angle stability can be divided into small-disturbance stability and transient stability. Small-disturbance stability refers to the ability of power system to maintain synchronism under sufficient small disturbances. Transient stability [29] is commonly concerned with the ability of the power system to maintain synchronism

after severe disturbances. Voltage stability means the ability of power system to maintain steady voltages at all buses after suffering a disturbance from a given initial operating condition [29], which mainly depends on the ability to maintain equilibrium state between load demand and load supply. In addition, the frequency stability means the system ability to maintain steady-state frequency when suffering a serious system disturbance, which tends to cause power imbalance between generation and load [29]. Unfortunately, the sustained frequency fluctuations may lead to absent of generators or loads.

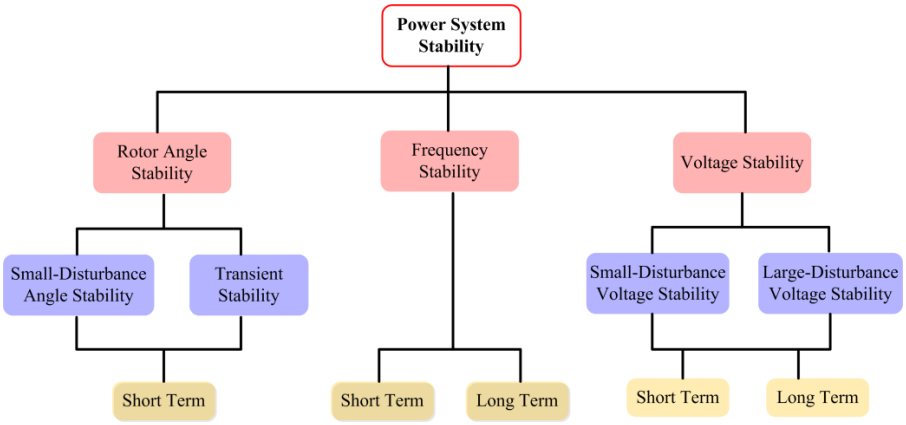

Fig.1-4 The classification of power system stability [30].

1.2.2 Stability issues of power electronic-fed power system

With the development of renewable energy sources, the power electronic-fed power plant or power system is becoming attractive structures to integrate various renewable energies. However, some emerging stability issues have been reported. Fig. 1-3 shows the diagram of an inverter-fed power system, which is composed of renewable energy sources, power inverters, *LC* filters, and local loads. Each energy source may be controlled by a local controller.

In such inverter-interfaced power systems, instability phenomena in different frequency range have been frequently reported [32]. Fig. 1-5 shows the diagram of multiple control loops in an islanded inverter-fed power system, which consists of paralleled inverters, local controller and local loads. The active and reactive power can be automatically distributed among paralleled inverters by droop-fed power controller. However, the low-frequency oscillation phenomenon may be triggered by droop-fed power controller [32]-[35] in independent power systems, or constant power control of active loads [36]-[37]. Fig. 1-6(a) shows the diagram of grid-connected inverter system, which consists of current controller, DC link voltage controller, and PLL. Compared with the control system of traditional synchronous

generator, the grid-connected inverter system tend to have higher bandwidth in multiple control loops as shown in Fig. 1-6(b). However, the low-frequency oscillation may be caused by grid synchronization control loops of grid-connected inverters [38]-[40]. In addition, the interaction of the inner current or voltage loops with passive components may bring harmonic-frequency instability phenomena [41]-[47]. Undoubtedly, these oscillation phenomena will cause the power quality and stability issues in whole power system.

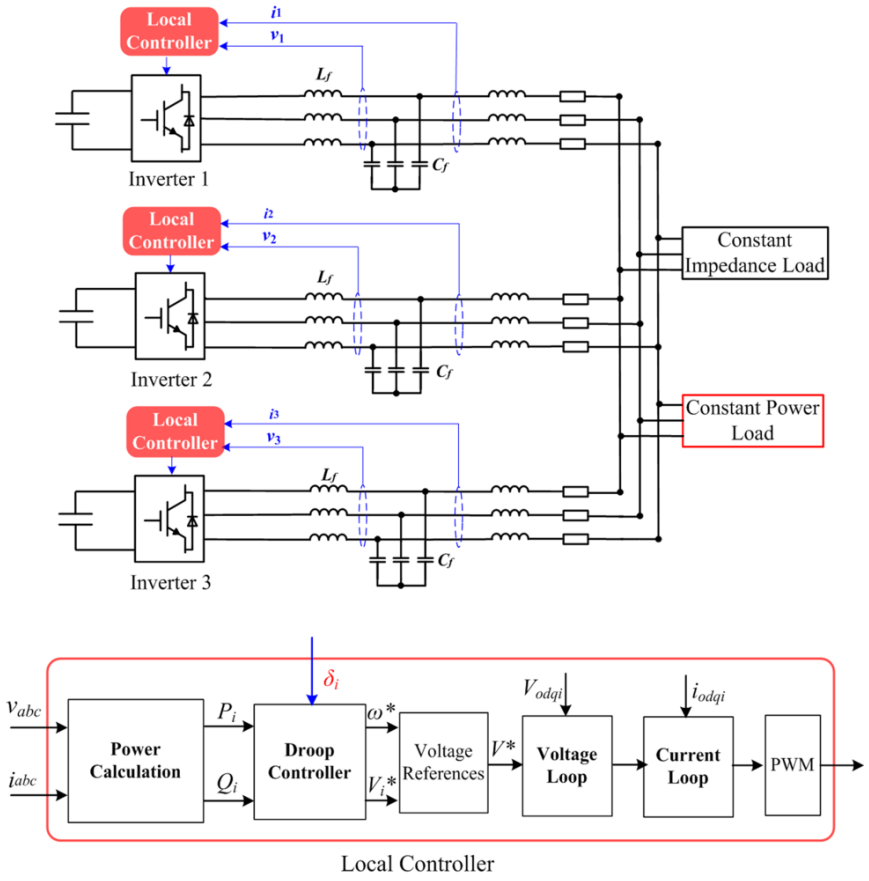

Fig. 1-5 The system diagram of islanded inverter-fed power system [34]

The harmonic resonance issue in the grid-connected inverter system also has been reported in [48]-[53]. The resonance mechanism of individual grid-connected inverter with *LCL* filter is revealed in [48], where the stable region and unstable region are identified and studied considering the effects of digital computation delay and PWM delay. Also, the stability assessment of grid-connected inverter with grid-current feedback and converter-current feedback is conducted considering the effect of time delay in [44], where a delay compensation method is also proposed to extend

the stable region of the grid-current feedback control. The inherent resonance performance of *LCL*-filter for grid-connected voltage source inverter is explored in [50]. And the different current control modes (grid-current feedback and converter-current feedback) are investigated, which shows the converter-current feedback is able to implement a more stable closed-loop control system due to the damping characteristic of *LCL*-filters [50].

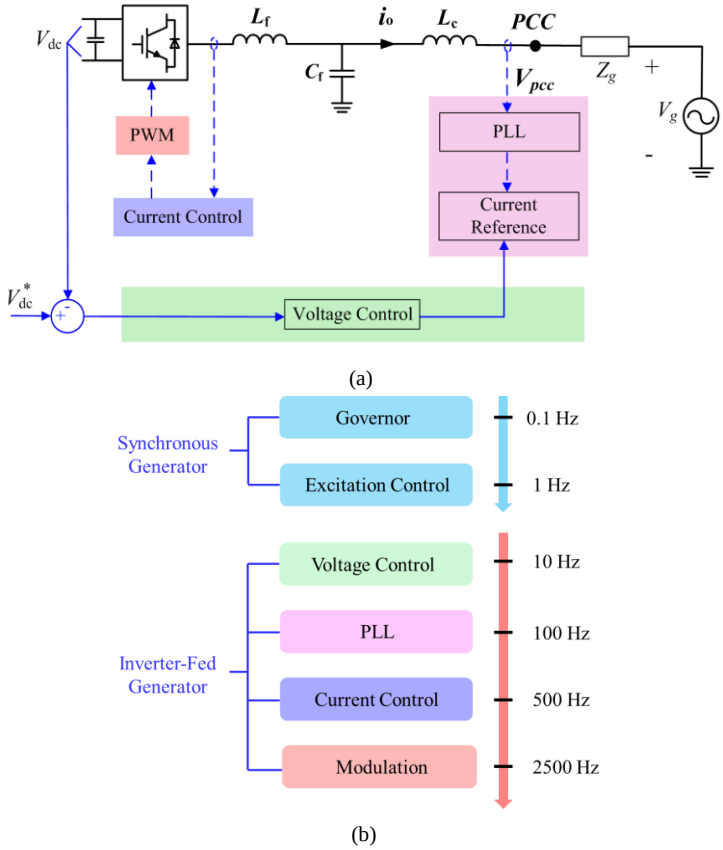

Fig. 1-6 The dynamic interactions of distributed generator with the grid.

Different from individual grid-connected inverter, the oscillation mechanism of multiple paralleled grid-connected inverters is complicated [54]. The dynamic interactions and coupling of paralleled inverters maybe trigger system resonance behavior and result in the system instability due to coupled grid impedance [54]-[60]. Resonance phenomenon in PV plant has been addressed in [58], where an equivalent model of paralleled grid-connected inverters system is established and the coupling effect is studied. The resonance problem caused by the interactions of multi-paralleled inverters with *LCL*-filters is addressed in [59], which shows an interactive resonant current circulating among the paralleled inverters may happen in

weak grid. A state-space-based harmonic stability analysis of paralleled grid-connected inverters system is addressed in [60], where the eigenvalue trajectories associated with time delay and coupled grid impedance are obtained. The analysis accounts for how the unstable inverter triggers the harmonic resonance and results in the oscillation of whole paralleled system.

1.2.3 Modeling and stability analytical techniques of inverter-fed power system

To handle the low-frequency oscillation and high-frequency instability issue, some modeling and analytical techniques have been widely proposed.

The eigenvalue analysis is an effective approach to investigate small signal stability in power system. For given equilibrium points, the system may be linearized around the operating points and a linearized state-space model may be formulated. The small signal stability then can be predicted by computing and analyzing eigenvalues of state matrix [61]-[66]. These methods are able to identify oscillation modes and mode shape to reveal system damping characteristic. Furthermore, the contribution of each component on system oscillation modes may be investigated by means of the participation analysis, where the participation factors indicate the relative participations of the respective state in the corresponding modes [61]. In addition, the full-order state-space model can be simplified as a reduced-order model by removing certain irrelevant states to specific oscillation modes. The eigenvalue-based small signal stability analysis for inverter-fed power systems has initially been presented in [35], which merely focuses on the low-frequency oscillations performance caused by droop control loop. A more comprehensive approach to modeling the inverter-fed power system has been established in [21], where the state-space model of individual inverter is first built, and then all other inverters and network components are modeled on the common frame. Finally, the oscillation modes associated with the different control loops are identified. To further study the microgrid dynamics with active loads, a full-order state-space model including active rectifiers is presented in [36], where the participation analysis is performed for analyzing the significant interactions between the inverters and active load. In [16], a more accurate state-space model with the influence of PLL for the inverter-fed islanded microgrid is developed. However, the aforementioned works mainly focus on the low-frequency oscillations due to the interactions of power controllers and PLL within the DG units and active loads. In addition, recent studies [67]-[71] show that the time delay maybe has a critical effect on harmonic-frequency oscillations, which are commonly ignored in these previous works.

Note that the harmonic state-space modeling method is also presented to reveal the frequency-coupling and phase dependent characteristic of nonlinear and time-varying systems in recent studies [72]-[76]. In fact, the effect of switching dynamics tend to be neglected by using the state-space averaging model if the switching

frequency is much higher than the bandwidth of the inner current and voltage control loops [72].

The impedance-based approaches also have been developed as a promising method to reveal the instability mechanism in [77]-[84]. The impedance-based stability criterion was originally introduced in [65], which is able to predict the system stability at local points based on the ratio of the output impedance of inverter and the equivalent system impedance seen from the inverter. The contribution of each DG inverter on system stability can be assessed in the frequency domain. An impedance-based approach is developed for an inverter-fed power system that includes multiple current- and voltage-controlled inverters with *LCL*- and *LC*-filters [80]. In addition, the passivity-based stability analysis methods for grid-connected inverters are developed in [85]-[89], which are able to assess resonance destabilization by negative-conductance behavior identification. These studies show that the time delay and current controller dynamics bring about a negative conductance and contribute to resonance destabilization.

However, the aforementioned linearized model-based methods tend to require the detailed representation of electrical system and control system.

It should be noted that frequency-scanning-based resonance assessment criterions have been earlier studied and used in [90]-[94]. The frequency scanning-based impedance analysis is originally presented to explain sub-synchronous oscillation phenomena in power system. The small signal disturbance is injected into grid-connected inverter system in particular frequency range, and the impedance is computed according to harmonic voltage response by Fourier analysis, then the stability is predicted on the basis of impedance stability criterion [94].

Although these aforementioned modeling and analytical approaches have been developed in previous works, there still exist some drawbacks and remaining problems. For instance, (1) The influences from time delay of digital control system on instability phenomenon tend to be overlooked. (2) The existing methods fail to identify the contributions of different components on harmonic instability. (3) The resonance mechanism of multiple paralleled grid-connected inverters system is not investigated completely. (4) In large-scale inverter-fed power system, the formulation of small signal model is commonly complicated, which is not easy to perform stability assessment in industry application.

Therefore, the objective of this project is to address aforementioned problems, and to develop effective modelling and analysis tools for stability assessment in power-electronics-fed power system.

1.3 Project Objectives

In this project, the low-frequency and high-frequency instability phenomenon in islanded inverter-fed power system is investigated. Furthermore, the resonance phenomenon of multiple paralleled grid-connected inverters system is analyzed. The contributions of this work can be described as following.

(1) A state-space-based method is presented to address high-frequency instability of inverter-fed power system, where the participation analysis is adopted to evaluate and identify the contributions of different component on harmonic-frequency oscillation. On the basis of participation analysis, a reduced-order model applied in harmonic instability assessment is developed.
(2) The time delay of digital control system is incorporated into state-space model by using Pade approximation, and the influence of time delay on the harmonic instability is revealed.
(3) A computationally-efficient approach to assess low-frequency oscillation and high-frequency resonance of inverter-fed power system is presented.
(4) A state-space-based impedance stability analysis method for grid-connected inverters system is presented. The proposed approach establishes the bridge between the state-space-based modelling and impedance-based stability criterion, which combines the advanced merits of the two worlds.
(5) A frequency scanning-based impedance analysis for stability assessment of grid-connected inverters system, which mitigates the requirement of small signal models applied in stability analysis and inherit the superior feature of impedance stability criterion with consideration of the inverter nonlinearities. The frequency scanning-based impedance stability criterion can be easily performed for stability assessment without using the detailed mathematical model.

1.4 Thesis outline

This thesis is composed of five sections. The chapter1 first introduces the background of this project and the problem statements, where the existing modelling and analytical approaches for inverter-fed power system are reviewed. Then, thesis structure and relationship between chapters is clarified. The chapter 2 presents a state-space-based modeling and analysis of inverter-fed power system. The chapter 3 developed a CCM-based (Component Connection Method) modelling and analytical method of inverter-fed power system. The chapter 4 presents the instability assessment methods of grid-connected inverter systems. The chapter 5 draws main conclusions in this project. Fig. 1-7 shows the thesis structure and interconnection relationship between chapters.

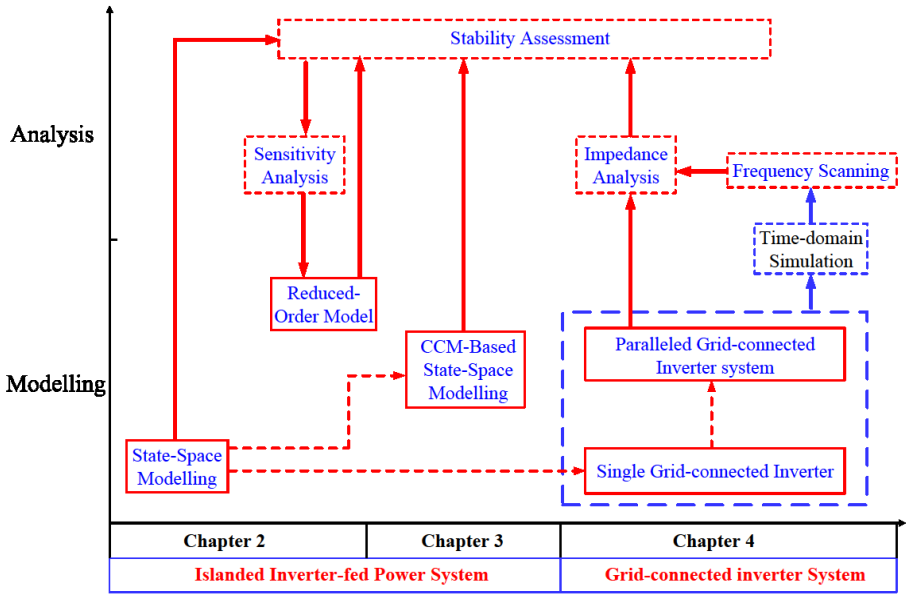

Fig. 1-7. Thesis structure and relationship between chapters

1.5 List of publications

Journal papers:

J1. **Y. B. Wang**, X. Wang, F. Blaabjerg, and Z. Chen, "Harmonic instability assessment using state-space modeling and participation analysis in inverter-fed power systems," ***IEEE Transactions on Industrial Electronics***, vol. 64, no. 1, pp. 806-816, Jan, 2017.

J2. **Y. B. Wang**, X. Wang, Z. Chen, and F. Blaabjerg, "Distributed Optimal Control of Reactive Power and Voltage in Islanded Microgrids," ***IEEE Transactions on Industrial Application***, vol. 53, no. 1, pp. 340-349, Jan-Feb, 2017.

J3. **Y. B. Wang**, X. Wang, Z. Chen, and F. Blaabjerg, "Small-signal stability analysis of inverter-fed power systems using component connection method," ***IEEE Transactions on Smart Grid***. (Early access).

J4. **Y. B. Wang**, Z. Chen, X. Wang, "Eigenvalue-based Harmonic Resonance Assessment of Multiple Paralleled Grid-Tied Inverters system," ***IEEE Transactions on Power Electronics***. (Reviewing).

Conference papers:

C1. **Y. B. Wang**, X. Wang, F. Blaabjerg, and Z. Chen, "Eigenvalue-based harmonic stability analysis method in inverter-fed power systems," *in Proc. of IEEE Industrial Electronics Society 41st Annual Conference, (IECON, 2015)*, pp. 3277-3282, 9-12 November, 2015.

C2. **Y. B. Wang**, Z. Chen and X. Wang, "Distributed Optimal Control of Reactive Power and Voltage in Islanded Microgrids," *in Proc. Applied Power Electronics Conference and Exposition (APEC)*, pp.3431-3438, 20-24 Mar, 2016.

C3. **Y. B. Wang**, X. Wang and Z. Chen, "Harmonic Stability Analysis of Inverter-Fed Power Systems Using Component Connection Method." *in Proc. of the 9th International Conference on Power Electronics – ECCE Asia* (ICPE 2016-ECCE Asia), pp. 1-8, 1-5 June, 2016.

C4. **Y. B. Wang**, Z. Chen, and F. Deng, "Dynamic droop scheme considering effect of intermittent renewable energy source," *in Proc. IEEE 7th International Symposium on Power Electronics for Distributed Generation systems (PEDG)*, pp. 1-6, 27-30 June, 2016.

C5. **Y. B. Wang**, X. Wang, Z. Chen, and F. Blaabjerg, "State-space-based harmonic stability assessment of paralleled grid-connected inverters system," *in Proc. 42th Annu. Conf. IEEE Industrial Electronics Society*, 2016.

C6. **Y. B. Wang**, X. Wang, Z. Chen, and F. Blaabjerg, "Frequency scanning-based impedance stability criterion for grid-connected inverters system." *The 10th International Conference on Power Electronics – ECCE Asia* (ICPE 2017-ECCE Asia). (Accepted).

C7 **Y. B. Wang**, X. Wang, Z. Chen, and F. Blaabjerg, "Harmonic resonance assessment of multiple paralleled grid-connected inverters system." T*he 10th International Conference on Power Electronics – ECCE Asia* (ICPE 2017-ECCE Asia). (Accepted).

CHAPTER 2. HARMONIC-FREQUENCY STABILITY ASSESSMENT OF INVERTER-FED POWER SYSTEM

This chapter concentrates on the harmonic instability investigation of inverter-interfaced power system. A state-space model of the system is first built. And the eigenvalue-based stability assessment approach is presented. Moreover, participation analysis is performed to identify the contributions of different components on harmonic-frequency oscillation modes.

2.1. Modeling of inverter-interfaced power system

This section describes the circuit topology of the inverter-interfaced power system in this study. The small-signal model of individual inverter with consideration of time delay influences of digital control system. Also, a linearized small signal model of network and loads is built. Finally, the whole small signal model of the system is founded [72].

2.1.1 System configuration

Fig. 2-1 shows the single line diagram of the three-phase power system. It can be seen that two inverters are paralleled to form an independent power system. As illustrated in Fig. 2-2, individual inverter is enabled by local control system, containing voltage, current and power control loop. The control objectives of voltage and current loop are to track reference voltage and output current. And the control objective of power controller is to distribute the active and reactive power among inverters. In this independent power system, droop scheme is employed to distribute the active and reactive power without using communication links in the presence of load disturbances [21]. In the proposed model, the switching-frequency harmonics are neglected since the switching frequency of inverters (10 kHz) is much higher than fundamental frequency.

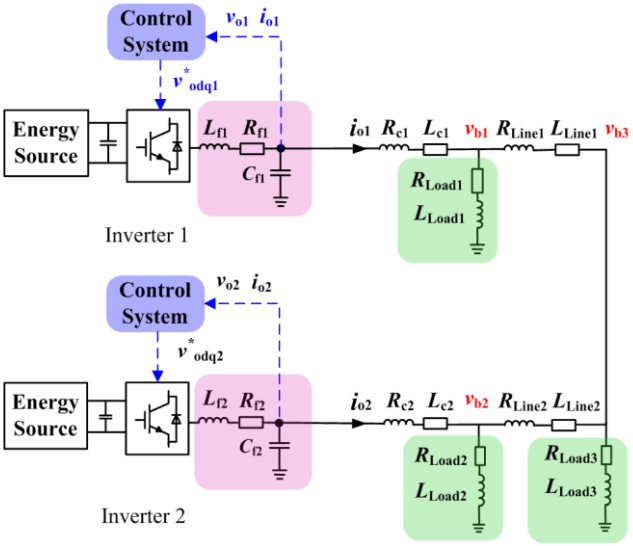

Fig. 2-1. System diagram of an inverter-interfaced power system [72].

2.1.2 Small signal modeling of individual inverter

The previous linearized models of voltage-source converters have been presented and the stability assessment has been performed in [21], which primarily concentrates on inner control loop, as well as the droop-driven power control loop. However, the dynamics of control loop and the time delay of digital control system maybe give rise to key effects on high-frequency oscillation performance. But the effects of delay plant are always overlooked in previous models. Thus, the main work of this section is to develop a state-space model with consideration of delay influence [72].

The system diagram of single inverter is depicted in Fig. 2-2, containing control system, time delay, filter and output inductance. In this modeling procedure, the local *dq*-frame of inverter1 is defined as common frame, and the dynamics of all other inverters, network and loads are converted into the common frame [21].

(1) Voltage and Current Control Loop

The structure diagram of inner voltage and current controller is demonstrated in Fig.2-2. The dynamic equations of voltage controller is given as (2-1)-(2-3) [72].

$$\dot{\varphi}_{di} = v^*_{odi} - v_{odi}, \qquad \dot{\varphi}_{qi} = v^*_{oqi} - v_{oqi} \tag{2-1}$$

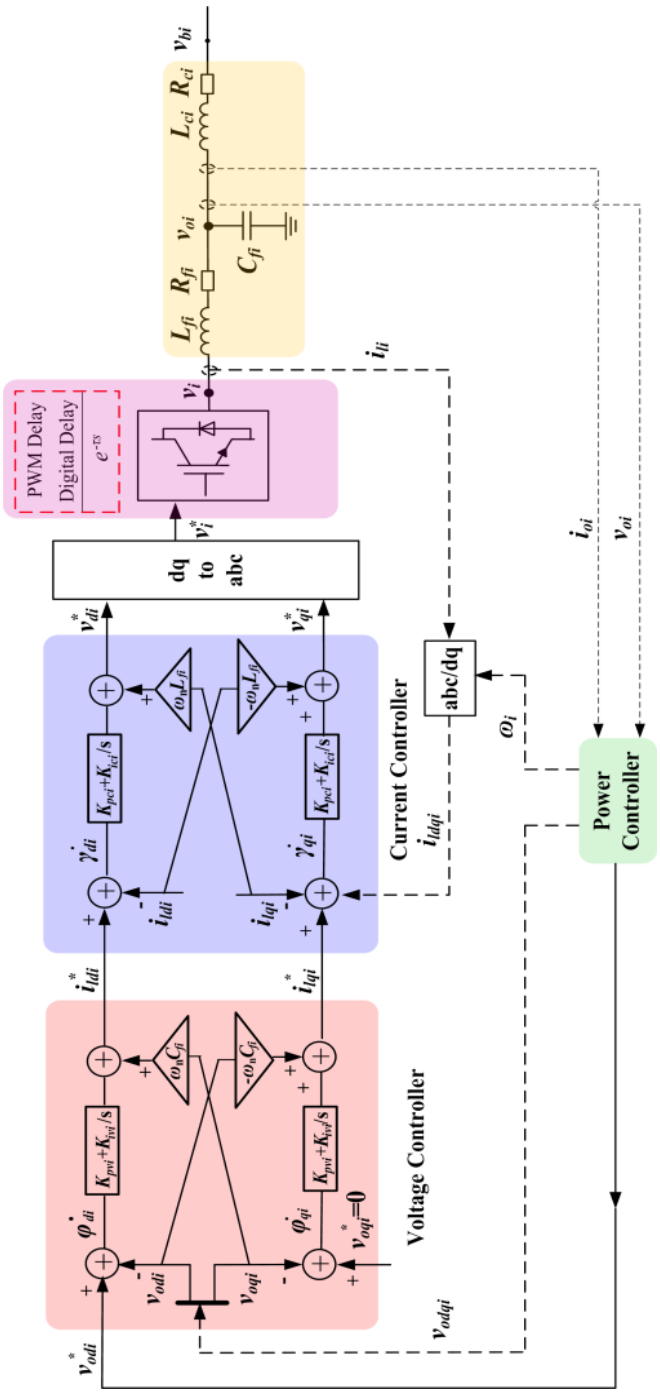

Fig. 2-2. The system diagram of individual inverter.

$$i_{ldi}^{*} = \omega_n C_{fi} v_{oqi} + K_{pvi}(v_{odi}^{*} - v_{odi}) + K_{ivi}\varphi_{di} \tag{2-2}$$

$$i_{lqi}^{*} = -\omega_n C_{fi} v_{odi} + K_{pvi}(v_{oqi}^{*} - v_{oqi}) + K_{ivi}\varphi_{qi} \tag{2-3}$$

Then, small signal dynamics of voltage control loop is obtained by linearizing (2-1)-(2-3) as (2-4) and (2-5) [72].

$$\Delta\dot{\varphi}_{dqi} = [0][\Delta\varphi_{dqi}] + B_{V1}[\Delta v_{odqi}^{*}] + B_{V2}[\Delta i_{ldqi}, \Delta v_{odqi}, \Delta i_{odqi}]^{T} \tag{2-4}$$

$$\Delta i_{ldqi}^{*} = C_V[\Delta\varphi_{dqi}] + D_{V1}[\Delta v_{odqi}^{*}] + D_{V2}[\Delta i_{ldqi}, \Delta v_{odqi}, \Delta i_{odqi}]^{T} \tag{2-5}$$

where $B_{V1} = \begin{bmatrix} 1 & 0 \\ 0 & 1 \end{bmatrix}$, $B_{V2} = \begin{bmatrix} 0,0,-1,0,0,0 \\ 0,0,0,-1,0,0 \end{bmatrix}$, $C_V = \begin{bmatrix} K_{ivi} & 0 \\ 0 & K_{ivi} \end{bmatrix}$, $D_{V1} = \begin{bmatrix} K_{pvi} & 0 \\ 0 & K_{pvi} \end{bmatrix}$

$$D_{V2} = \begin{bmatrix} 0,0,-K_{pvi},\omega_n C_{fi},0,0 \\ 0,0,-\omega_n C_{fi},-K_{pvi},0,0 \end{bmatrix}$$

The mathematical representation of current loop is written as (2-6)-(2-8) according to Fig. 2-2 [72].

$$\dot{\gamma}_{di} = i_{ldi}^{*} - i_{ldi}, \qquad \dot{\gamma}_{qi} = i_{lqi}^{*} - i_{lqi} \tag{2-6}$$

$$v_{idi}^{*} = \omega_n L_{fi} i_{lqi} + K_{pci}(i_{ldi}^{*} - i_{ldi}) + K_{ici}\gamma_{di} \tag{2-7}$$

$$v_{iqi}^{*} = -\omega_n L_{fi} i_{ldi} + K_{pci}(i_{lqi}^{*} - i_{lqi}) + K_{ici}\gamma_{qi} \tag{2-8}$$

Then, the linearized representation of current controller is derived by linearizing (2-6)-(2-8) as (2-9) and (2-10) [72].

$$\Delta\dot{\gamma}_{dqi} = [0][\Delta\gamma_{dqi}] + B_{C1}[\Delta i_{ldqi}^{*}] + B_{C2}[\Delta i_{ldqi}, \Delta v_{odqi}, \Delta i_{odqi}]^{T} \tag{2-9}$$

$$\Delta v_{idqi}^{*} = C_C[\Delta\gamma_{dqi}] + D_{C1}[\Delta i_{ldqi}^{*}] + D_{C2}[\Delta i_{ldqi}, \Delta v_{odqi}, \Delta i_{odqi}]^{T} \tag{2-10}$$

$B_{C1} = \begin{bmatrix} 1 & 0 \\ 0 & 1 \end{bmatrix}$, $B_{C2} = \begin{bmatrix} -1,0,0,0,0,0 \\ 0,-1,0,0,0,0 \end{bmatrix}$, $C_C = \begin{bmatrix} K_{ici} & 0 \\ 0 & K_{ici} \end{bmatrix}$, $D_{C1} = \begin{bmatrix} K_{pci} & 0 \\ 0 & K_{pci} \end{bmatrix}$,

$$D_{C2} = \begin{bmatrix} -K_{pci},\omega_n L_{fi},0,0,0,0 \\ -\omega_n L_{fi},-K_{pci},0,0,0,0 \end{bmatrix}$$

(2) Time Delay Model of Digital Control Loop

The digital control loop delay can be shown as (2-11) [72].

$$v_i = e^{-\tau \bullet s} v_i^{*}, \ (i = 1, \ 2) \tag{2-11}$$

where T_s is the sampling period of control system, and $\tau = 1.5T_s$ is delay time caused by digital computation delay (T_s) and the PWM delay ($0.5T_s$) [95]-[96]. In order to perform oscillation mode analysis and explain the coupling relationship among the

different states, the delay plant (2-11) is represented by Pade approximation, which is an effective method to investigate nonlinear plant characteristic. In this work, the third-order Pade approximation is performed. The exponential term can be given as (2-12) [97]-[99].

$$e^{-\tau \bullet s} \approx \frac{120-60(\tau s)+12(\tau s)^2-(\tau s)^3}{120+60(\tau s)+12(\tau s)^2+(\tau s)^3} \tag{2-12}$$

The aforementioned delay representation (2-12) can be transferred into the linearized state-space form as (2-13) and (2-14).

$$\Delta \dot{x}_{del} = A_{del}\Delta x_{del} + B_{del}\Delta v_i^* \tag{2-13}$$

$$\Delta v_i = C_{del}x_{del} + D_{del}\Delta v_i^* \tag{2-14}$$

where $x_{del} = \left[x_{dq1}, x_{dq2}, x_{dq3}\right]^T$ are state variables of delay plant (2-13), $A_{del}, B_{del}, C_{del}, D_{del}$ are the mathematical matrices of the delay plant. $A_{del} = \begin{bmatrix} A_d & \\ & A_d \end{bmatrix}$, $B_{del} = \begin{bmatrix} B_d & \\ & B_d \end{bmatrix}$, $C_{del} = \begin{bmatrix} C_d & \\ & C_d \end{bmatrix}$, $D_{del} = \begin{bmatrix} D_d & \\ & D_d \end{bmatrix}$, $A_d = \begin{bmatrix} 0 & 1 & 0 \\ 0 & 0 & 1 \\ -120/\tau^3 & -60/\tau^2 & -12/\tau \end{bmatrix}$, $B_d = \begin{bmatrix} 0 & 0 & 1 \end{bmatrix}^T$, $C_d = \begin{bmatrix} 240/\tau^3 & 0 & 24/\tau \end{bmatrix}^T$, $D_d = \begin{bmatrix} -1 \end{bmatrix}^T$, $v_i^* = \left[v_{id}^*, v_{iq}^*\right]$, $v_i = \left[v_{id}, v_{iq}\right]$.

(3) Droop-driven Power Controller

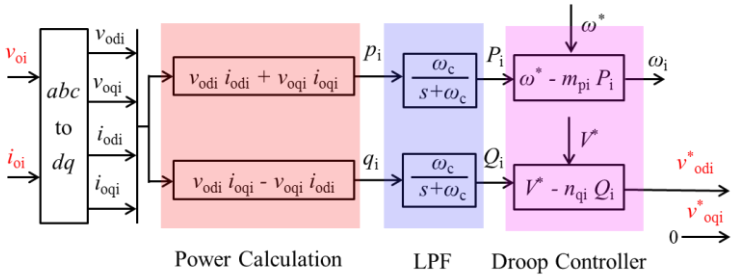

Fig. 2-3. The block diagram of droop-based power controller [72].

Fig. 2-3 shows the detailed representation of the droop-driven power controller, including the power calculation block, low pass filter and droop controller. The power controller is employed to achieve power sharing in islanded mode [12]. To carry out the power sharing proportionally, the frequency and voltage reduction relationship is introduced to adjust command reference in the presence of loads disturbance. The active power-frequency (*P-f*) and reactive power-voltage (*Q-V*) droop relationship [21] can be given as (2-15) and (2-16).

$$\omega_i = \omega^* - m_{pi}P_i \tag{2-15}$$

$$V_{odi}^{*} = V^{*} - n_{qi}Q_i \tag{2-16}$$

The instantaneous powers in *dq*-frame are obtained by the power calculation block as shown in Fig. 2-3. Moreover, the average powers are computed from instantaneous powers, which are given as (2-17) and (2-18) [12].

$$P_i = \frac{\omega_c}{s+\omega_c} p_i \tag{2-17}$$

$$Q_i = \frac{\omega_c}{s+\omega_c} q_i \tag{2-18}$$

where the instantaneous active and reactive power can be described in *dq*-frame as (2-19) and (2-20) [12].

$$p_i = v_{odi} i_{odi} + v_{oqi} i_{oqi} \tag{2-19}$$

$$q_i = v_{odi} i_{oqi} - v_{oqi} i_{odi} \tag{2-20}$$

(4) *LC* Filters and Line Impedance

The differential equations of filter and line impedance of inverter (i=1,2,…n) can be established according to Fig. 2-2 as (2-21) and (2-22) [12].

$$\frac{di_{ldi}}{dt} = -\frac{R_{fi}}{L_{fi}} i_{ldi} - \omega_i i_{lqi} + \frac{1}{L_{fi}} v_{di} - \frac{1}{L_{fi}} v_{odi} \tag{2-21}$$

$$\frac{di_{lqi}}{dt} = -\frac{R_{fi}}{L_{fi}} i_{lqi} + \omega_i i_{ldi} + \frac{1}{L_{fi}} v_{qi} - \frac{1}{L_{fi}} v_{oqi} \tag{2-22}$$

$$\frac{dv_{odi}}{dt} = -\omega_i v_{oqi} + \frac{1}{C_{fi}} i_{ldi} - \frac{1}{C_{fi}} i_{odi} \tag{2-23}$$

$$\frac{dv_{oqi}}{dt} = \omega_i v_{odi} + \frac{1}{C_{fi}} i_{lqi} - \frac{1}{C_{fi}} i_{oqi} \tag{2-24}$$

$$\frac{di_{odi}}{dt} = -\frac{R_{ci}}{L_{ci}} i_{odi} - \omega_i i_{oqi} + \frac{1}{L_{ci}} v_{odi} - \frac{1}{L_{ci}} v_{bdi} \tag{2-25}$$

$$\frac{di_{oqi}}{dt} = -\frac{R_{ci}}{L_{ci}} i_{oqi} + \omega_i i_{odi} + \frac{1}{L_{ci}} v_{oqi} - \frac{1}{L_{ci}} v_{bqi} \tag{2-26}$$

Then, state-space dynamic model of *LC* filter plant and the line impedance is formulated by combining and linearizing (2-21)-(2-26) as (2-27) [12].

$$\begin{bmatrix} \Delta \dot{i}_{ldqi} \\ \Delta v_{odqi} \\ \Delta i_{odqi} \end{bmatrix} = B_1 \Delta\omega_i + B_2 \Delta v_{dqi} + B_3 \begin{bmatrix} \Delta i_{ldqi} \\ \Delta v_{odqi} \\ \Delta i_{odqi} \end{bmatrix} + B_4 \Delta v_{bdqi} \tag{2-27}$$

where $B_1 = \left[I_{lqi0}, -I_{ldi0}, V_{oqi0}, -V_{odi0}, I_{oqi0}, -I_{odi0}\right]^T$, $B_2 = \left[-A_{12}, O_{2\times4}\right]^T$, $B_4 = \left[O_{2\times4}, -A_{31}\right]^T$

$$B_3=\begin{bmatrix} A_{11} & A_{12} & 0 \\ A_{21} & A_{22} & -A_{21} \\ 0 & A_{31} & A_{32} \end{bmatrix},\ A_{11}=\begin{bmatrix} -\frac{R_{fi}}{L_{fi}} & \omega_{i0} \\ -\omega_{i0} & -\frac{R_{fi}}{L_{fi}} \end{bmatrix},\ A_{12}=\begin{bmatrix} -\frac{1}{L_{fi}} & 0 \\ 0 & -\frac{1}{L_{fi}} \end{bmatrix},\ A_{21}=\begin{bmatrix} \frac{1}{C_{fi}} & 0 \\ 0 & \frac{1}{C_{fi}} \end{bmatrix}$$

$$A_{22}=\begin{bmatrix} 0 & \omega_{i0} \\ -\omega_{i0} & 0 \end{bmatrix},A_{31}=\begin{bmatrix} \frac{1}{L_{ci}} & 0 \\ 0 & \frac{1}{L_{ci}} \end{bmatrix},A_{32}=\begin{bmatrix} -\frac{R_{ci}}{L_{ci}} & \omega_{i0} \\ -\omega_{i0} & -\frac{R_{ci}}{L_{ci}} \end{bmatrix}$$

The linearized small signal model of individual inverter can be finally established by combining dynamic equations of the voltage controller (2-4)-(2-5), current controller (2-9)-(2-10), droop controller (2-15)-(2-16), time delay model (2-3), *LC* filter and output inductance (2-27) as (2-28) [72].

$$\Delta \dot{x}_{invi}=A_{invi}\Delta x_{invi}+B_{invi}\Delta v_{bdqi}+B_{inv2i}\Delta\omega_i \tag{2-28}$$

$\Delta x_{invi}=\left[\Delta P_i,\Delta Q_i,\Delta\varphi_{dqi},\Delta\gamma_{dqi},\Delta i_{ldqi},\Delta x_{di},\Delta v_{odqi},\Delta i_{odqi}\right](i=1,2)$ is state vector of *i*th inverter. v_{bdqi} is *i*th bus voltage connecting inverter *i*. ω_i is angle frequency of output voltage of *i*th inverter, where the angle frequency of inverter1 is selected as common frequency [72]. Input variables of inverter are the bus voltage (v_{bdqi}) and angle frequency (ω_i). A_{invi}, B_{invi}, B_{inv2i} are parameter matrices of each inverter.

2.1.3 STATE-SPACE MODELING OF OVERALL SYSTEM

In this section, the current and voltage equations of the network and load are first founded. As illustrated in Fig. 2-1, the voltage equations at different buses are formulated as (2-29) [72]

$$\begin{aligned} V_{b1}&=R_{Load1}i_{Load1}+L_{Load1}\frac{di_{load1}}{dt} \\ V_{b2}&=R_{Load2}i_{Load2}+L_{Load2}\frac{di_{Load2}}{dt} \\ V_{b3}&=R_{Load3}i_{Load3}+L_{Load3}\frac{di_{Load3}}{dt} \end{aligned} \tag{2-29}$$

According to KCL, the bus voltage equations are rewritten as (2-30)

$$\begin{aligned} V_{b1}&=R_{Load1}(i_{o1}+i_{Line1})+L_{Load1}\frac{d(i_{o1}+i_{Line1})}{dt} \\ V_{b2}&=R_{Load2}(i_{o2}+i_{Line2})+L_{Load2}\frac{d(i_{o2}+i_{Line2})}{dt} \\ V_{b3}&=R_{Load3}(-i_{Line1}-i_{Line2})+L_{Load3}\frac{d(-i_{Line1}-i_{Line2})}{dt} \end{aligned} \tag{2-30}$$

Also, the current dynamic equations of lines can be formulated on DQ frame as (2-31) and (2-32) [72]

$$\frac{di_{LineD1}}{dt} = \frac{-R_1}{L_1} i_{LineD1} + \omega i_{LineQ1} + \frac{1}{L_1} V_{bD1} - \frac{1}{L_1} V_{bD2} \tag{2-31}$$

$$\frac{di_{LineQ1}}{dt} = \frac{-R_1}{L_1} i_{LineQ1} - \omega i_{LineD1} + \frac{1}{L_1} V_{bQ1} - \frac{1}{L_1} V_{bQ2}$$

$$\frac{di_{LineD2}}{dt} = \frac{-R_2}{L_2} i_{LineD2} + \omega i_{LineQ2} + \frac{1}{L_2} V_{bD2} - \frac{1}{L_2} V_{bD3} \tag{2-32}$$

$$\frac{di_{LineQ2}}{dt} = \frac{-R_2}{L_2} i_{LineQ2} - \omega i_{LineD2} + \frac{1}{L_2} V_{bQ2} - \frac{1}{L_2} V_{bQ3}$$

Similarly, the current dynamic equations of loads can be established on common frame as (2-33) [72]

$$\frac{di_{LoadDi}}{dt} = \frac{-R_{Loadi}}{L_{Loadi}} i_{LoadDi} + \omega i_{LoadQi} + \frac{1}{L_{Loadi}} V_{bDi} \qquad (i = 1,2,3) \tag{2-33}$$

$$\frac{di_{LoadQi}}{dt} = \frac{-R_{Loadi}}{L_{Loadi}} i_{LoadQi} - \omega i_{LoadDi} + \frac{1}{L_{Loadi}} V_{bQi} \qquad (i = 1,2,3)$$

Finally, a linearized small signal model can be established by combining DG inverters (2-21), voltage equations (2-30), network (2-31)-(2-32), loads equation (2-33) as (2-34).

$$\Delta \dot{x} = A \Delta x \tag{2-34}$$

where Δx is the state vector of the whole system. Δx=[Δx_{inv1},Δx_{inv2},Δi_{line1},Δi_{line2},Δi_{load1},Δi_{load2},Δi_{load3}]. Δi_{line1} and Δi_{line2} are state variables of line currents. Δi_{load1}, Δi_{load2} and Δi_{load3} are state variables of loads currents. A is state matrix of small signal model.

2.2. Harmonic Stability Assessment

Eigenvalue analysis has been intensively adopted to predict small signal stability in traditional power system [30]. It is able to indicate oscillation modes and damping characteristic in different frequency range. The imaginary part of eigenvalues indicates the oscillation frequency and the real part identifies the stability area. The eigenvalue trajectories of the state matrix (A) in (2-34) are obtained to assess the dynamic characteristic [72]. The system parameters and controller parameters are listed in Table I and Table II. And the initial steady-state equilibrium point for the stability analysis applied in this study is given in Table III.

Fig. 2-4(a)-(b) illustrates the eigenvalue trajectories with 3-order and 5-order Pade approximation. The harmonic-frequency (10000 rad/s) oscillation modes and low-frequency (150 rad/s) oscillation mode then can be observed [72]. The oscillation modes indicate that the harmonic-frequency eigenvalues ($\lambda_{1\text{-}2}$, $\lambda_{3\text{-}4}$, $\lambda_{5\text{-}6}$, $\lambda_{7\text{-}8}$) go to right-half plane as the increase of proportional parameter of voltage controllers (K_{pv}) [72]. However, it also can be observed that low-frequency modes ($\lambda_{9\text{-}10}$) are insensitive to the current and voltage controller parameter [72].

TABLE I

SYSTEM PARAMETERS [72]

Parameters	Value	Parameters	Value
Phase Voltage	220 V	DC Voltage	800 V
Sampling Frequency	10 kHz	L_{Line1}/R_{Line1}	2mH/0.2Ω
L_{f1}/R_{f1}	1.5mH/0.1Ω	L_{Line2}/R_{Line2}	2mH/0.2Ω
L_{f2}/R_{f2}	1.5mH/0.1Ω	C_{f1}/C_{f2}	25μF/25μF
L_{c1}/R_{c1}	1.8mH/0.1Ω	L_{Load2}/R_{Load2}	160mH/64Ω
L_{c2}/R_{c2}	1.8mH/0.1Ω	L_{Load3}/R_{Load3}	240mH/80Ω
L_{Load1}/R_{Load1}	155mH/64Ω		

TABLE II

THE PARAMETERS IN MULTIPLE CONTROL LOOPS [72]

Parameters	Value	Parameters	Value
m_{p1}/m_{p2}	1e-4/1e-4	K_{pv1}/K_{pv2}	(0-0.07)/(0-0.07)
n_{q1}/n_{q2}	1e-3/1e-3	K_{iv1}/K_{iv2}	200/200
K_{pc1}/K_{pc2}	(2-13)/(2-13)	K_{ic1}/K_{ic2}	4/4

TABLE III

STEADY-STATE OPERATION POINT [72]

Parameter	Value	Parameter	Value
I_{od10}/I_{od20}	[4.2,4.1]	I_{oq10}/I_{oq20}	[3.3,3.4]
V_{od10}/V_{od20}	[310,310]	V_{oq10}/V_{oq20}	[0,0]
I_{ld10}/I_{ld20}	[4,4]	I_{lq10}/I_{lq20}	[1,1]
ω_{10}/ω_{20}	[314,314]	ω_c	31.4
ω_n	314		

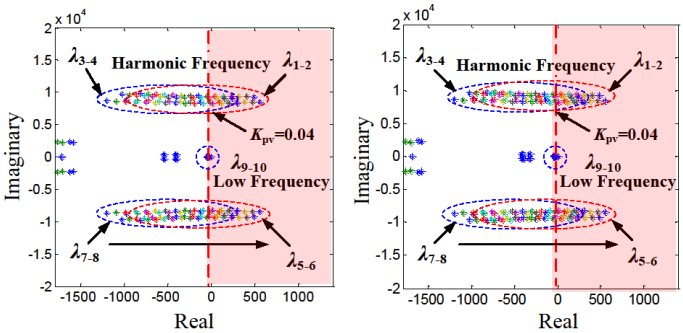

Fig. 2-4 Harmonic-frequency oscillation modes as a function of proportional coefficient of voltage controllers for 3-order (a) *and 5-order* (b) *Pade approximation* [72].

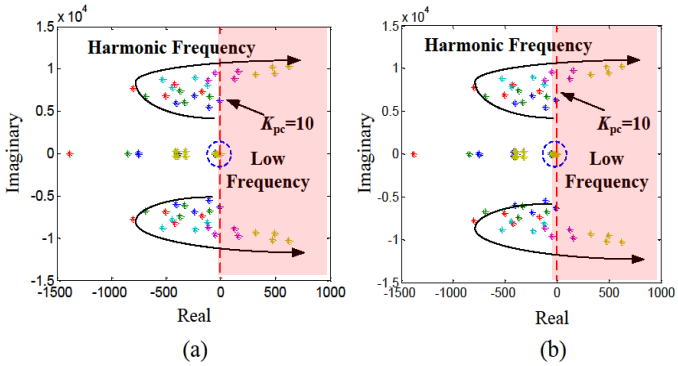

*Fig. 2-5 Harmonic-frequency oscillation modes as a function of the proportional coefficient of current controller for 3-order (*a) *and 5-order* (b) *Pade approximation* [72].

Fig. 2-5 indicates the high-frequency oscillation modes as increase of the proportional coefficient of current controllers (K_{pc}) from 2 to 12 [72]. It can be observed that the oscillation modes go toward right-half plane. The power system gets unstable if the proportional coefficient is higher than 10 [72]. Fig. 2-5(a)-(b) demonstrate the eigenvalue trajectories with the 3-order and 5-order Pade approximations of time delay [72].

Fig. 2-6 illustrates the harmonic-frequency oscillation modes if the sampling frequency of DG2 control system decreases from 10kHz to 6kHz [72]. It can be seen from the Fig. 2-6(a)-(b) that the oscillation modes for 3-order and 5-order Pade approximation go towards unstable region as the decrease of the sampling fequency [72]. The results obtained from Fig. 2-4 - Fig. 2.6 show the Pade order hardly affects on the accuracy of harmonic stability assessment [72].

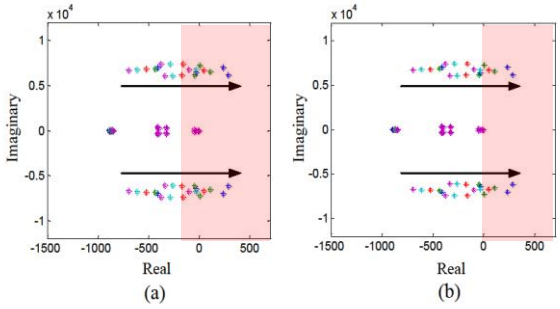

Fig. 2-6 Harmonic-frequency oscillation modes as a function of sampling frequency (f_d=10kHz, 9kHz, 8kHz, 6kHz) for 3-order and 5-order Pade approximation [72].

Besides, oscillation phenomenon of the paralleled inverters with the unequal proportional parameter of voltage controllers is also investigated [72]. Fig. 2-7 shows that the eigenvalues $\lambda_{1\text{-}2}$ and $\lambda_{5\text{-}6}$ go to right-half plane as increase of the proportional parameter of inverter1 voltage controller (K_{pv1}) [72]. However, the

eigenvalues $\lambda_{3\text{-}4}$ and $\lambda_{7\text{-}8}$ are still located in stable region. Hence, the harmonic-frequency oscillation phenomenon is caused by the modes $\lambda_{1\text{-}2}$ and $\lambda_{5\text{-}6}$ [72].

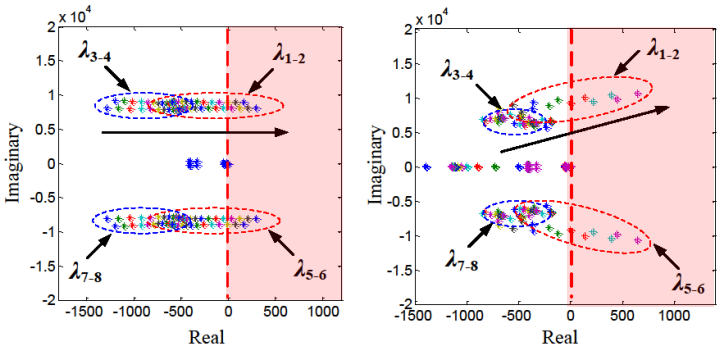

Fig. 2-7 Harmonic-frequency oscillation modes. (a) Oscillation modes as a function of proportional parameter of inverter1 voltage controller from 0 to 0.07 [72]. *(b) Oscillation modes as a function of the proportional parameter of inverter1 current controller from 2 to 13* [72].

2.3. Participation Analysis and Reduced-order Model

Participation analysis [100]-[104] is a useful solution to investigate the actions of components on oscillation modes, which is able to establish a bridge between state variables and oscillation modes, and identify the influences of parameters on system stability.

The participation factor p_{ki} of the k th state and i-th mode [100]-[104] can be given as.

$$p_{ki} = \frac{\partial \lambda_i}{\partial a_{kj}} = u_{ik} v_{ji} \tag{2-35}$$

Note that the sensitivity of eigenvalue λ_i to the element α_{kj} of the state matrix is obtained by product of the left eigenvector element u_{ik} and the right eigenvector element v_{ji}.

2.3.1 Participation analysis

Participation analysis also can be performed by caculating the participation of state variables in special modes [72], which reveals the different contribution of states on oscillation modes [72]. The participation matrix can be computed by left and right eigenvectors as (2-36) [72].

$$\mathbf{P=[p_1, p_2, \ldots, p_n]} \tag{2-36}$$

with

$$\mathbf{p_1} = [p_{1i}, p_{2i}, \cdots p_{ni}]^T = [u_{1i}v_{i1}, u_{2i}v_{i2}, \cdots u_{ni}v_{in}]^T$$

where $p_{ki} = u_{ki}v_{ik}$ is defined as the participation factor [100]-[104].

$U = [u_{1i}, u_{2i}, \cdots, u_{ni}]^T$ is matrix of right eigenvector, and $V = [v_{i1}, v_{i2}, \cdots, v_{in}]$ is matrix of left eigenvector. u_{ki} refers to the component on the *k*-th row and *i*-th column of matrix *U*. v_{ik} refers to the component on the *i*-th row and *k*-th column of the matrix *V*, which is able to reveal the participation of this component on certain oscillation modes [72].

Table 2-4 shows the participation analysis results of high-frequency oscillation modes, where current controller (i_{l1}/i_{l2}), voltage controller (v_{o1}/v_{o2}) and time delay (x_{p1}/x_{p2}) have high participation factors on $\lambda_{1\text{-}2}$, $\lambda_{3\text{-}4}$, $\lambda_{5\text{-}6}$, $\lambda_{7\text{-}8}$ [72]. But the states of network and loads slightly affect harmonic-frequency modes. The participation factor indicates that the current loop, voltage loop as well as time delay of digital controller produce dominant influence on harmonic-frequency oscillation modes [72]. The participation analysis shows the control loops of both inverters have identical contribution on harmonic oscillation [72].

Similarly, Table2-5 shows the participation analysis results of inverters with unequal controller parameters. Obviously, the inverter1 mainly affects the modes $\lambda_{1\text{-}2}$, $\lambda_{5\text{-}6}$ and inverter2 mainly affects the modes $\lambda_{3\text{-}4}$, $\lambda_{7\text{-}8}$ [72]. It is understood that the origin of the instability problem is caused by inverter1, which also verifies the analytical results from Fig. 2-7 [72].

TABLE 2-4

THE PARTICIPATION ANALYSIS RESULT FOR INVERTERS WITH EQUAL CONTROLLER PARAMETERS[72]

$\lambda_{1\text{-}2}$		$\lambda_{3\text{-}4}$	
State	Participation	State	Participation
x_{p1}/x_{p2}	0.29/0.29	x_{p1}/x_{p2}	0.33/0.33
v_{o1}/v_{o2}	0.14/0.14	v_{o1}/v_{o2}	0.12/0.12
i_{o1}/i_{o2}	0.02/0.02	i_{o1}/i_{o2}	0.0006/0.0006
i_{l1}/i_{l2}	0.33/0.33	i_{l1}/i_{l2}	0.36/0.36
Remaining states	< 0.01	Remaining states	< 0.01
$\lambda_{5\text{-}6}$		$\lambda_{7\text{-}8}$	
State	Participation	State	Participation
x_{p1}/x_{p2}	0.28/0.28	x_{p1}/x_{p2}	0.33/0.33
v_{o1}/v_{o2}	0.15/0.15	v_{o1}/v_{o2}	0.13/0.13
i_{o1}/i_{o2}	0.02/0.02	i_{o1}/i_{o2}	0.0005/0.0006
i_{l1}/i_{l2}	0.34/0.34	i_{l1}/i_{l2}	0.38/0.38
Remaining states	< 0.01	Remaining states	< 0.01

TABLE 2-5

THE PARTICIPATION ANALYSIS RESULT FOR INVERTERS WITH UNEQUAL CONTROLLER PARAMETERS [72]

$\lambda_{1\text{-}2}$		$\lambda_{3\text{-}4}$	
State	Participation	State	Participation
i_{l1}/i_{l2}	0.64/0.03	i_{l1}/i_{l2}	0.02/0.73
v_{o1}/v_{o2}	0.28/0.015	v_{o1}/v_{o2}	0.006/0.24
i_{o1}/i_{o2}	0.023/0.005	i_{o1}/i_{o2}	0.002/0.015
x_{p1}/x_{p2}	0.58/0.024	x_{p1}/x_{p2}	0.024/0.70
Remaining states	< 0.01	Remaining states	< 0.01
$\lambda_{5\text{-}6}$		$\lambda_{7\text{-}8}$	
State	Participation	State	Participation
i_{l1}/i_{l2}	0.65/0.03	i_{l1}/i_{l2}	0.02/0.79
v_{o1}/v_{o2}	0.3/0.016	v_{o1}/v_{o2}	0.006/0.25
i_{o1}/i_{o2}	0.026/0.006	i_{o1}/i_{o2}	0.002/0.016
x_{p1}/x_{p2}	0.54/0.02	x_{p1}/x_{p2}	0.023/0.69
Remaining states	< 0.01	Remaining states	< 0.01

Thus, the participation analysis can identify the states and parameters leading to harmonic oscillation, which is an useful solution to investigate oscillation origins and reveals the contribution of components on the instability phenomenon [72].

2.3.2 Reduced-order model based on participation analysis

Note that the incorporation of inner control loops and the digital control delay undoubtedly increases the order of the system state matrix. The model-order reduction based on the specific oscillation modes is then needed for the system with a large number of inverters [72].

On the basis of participation analysis, certain modes slightly related with harmonic-frequency oscillation can be removed to establish a order-reduced model [72]. As shown in Table 2-4 and Table 2-5, the inner control loops and digital control delay have high participation on harmonic oscillation. Thereby, these states are reserved while the other states can be removed [72].

The harmonic-frequency eigenvalue traces of the order-reduced model are depicted in Fig. 2-8. It can be seen that the order-reduced model indicates identical oscillation performance compared with original model, which thus validates the correctness of the reduced-order model [72].

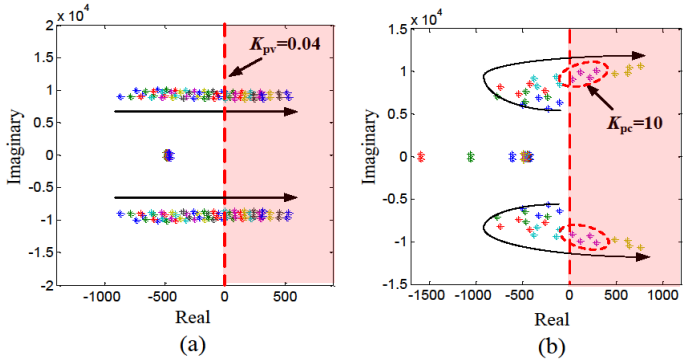

Fig. 2-8. Harmonic-frequency oscillation modes in the order-reduced model. (a) The oscillation modes with increase of voltage controller proportional parameter (K_{pv}) from 0 to 0.07 [72]. *(b) The oscillation modes with increase of current controller proportional parameter (K_{pc}) from 2 to 12* [72].

2.4. Simulation and Experimental Verification

Fig. 2-9 illustrates the experimental platform of the exemplified system, where the circuit structure and parameters are given in Fig. 2-1 and Table 2-1. In the exemplified system, two Danfoss inverters with 800V dc voltage source are used as distributed generators [72]. The whole power system is controlled by dSPACE1006 system with the sampling frequency of 10 kHz.

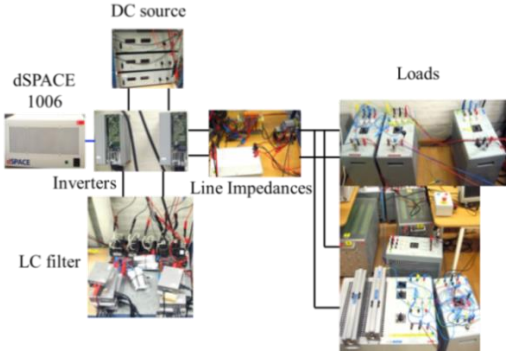

Fig. 2-9 Experimental setup [72]

2.4.1 Simulation Verification

To validate the effectiveness of the proposed eigenvalue-based analysis method, the simulations are performed in MATLAB/SIMULINK. The test system parameters have been given in Table 2-1 and Table 2-2.

(1) Harmonic instability phenomena associated with voltage controller

Fig. 2-10 demonstrates the simulated results of unstable case, where the oscillation phenomenon happens when the proportional parameters (K_{pv}) of voltage controllers are within unstable region [33]. Also, the output current of inverters and voltages are shown in Fig. 2-10. On the other hand, the system is stablized as shown in Fig. 2-11 once the proportional parameters are reduced. Thus, the simulation results, accompanying with the theoretical analysis results shown in Fig. 2-4 and Fig.2-5, explain that the inverter with the high proportional parameter of inner control loop brings about the oscillation phenomenon [33].

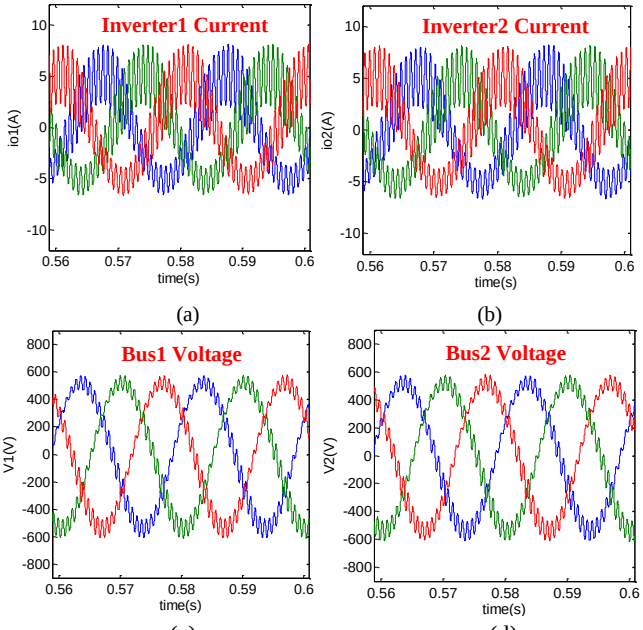

Fig. 2-10 Simulated unstable case if the proportional parameters (K_{pv}) are within unstable region (K_{pv}=0.055, K_{pc}=9) [33]. *(a) Inverter1 current. (b) Inverter2 current. (c) Bus1 voltage. (d) Bus2 voltage.*

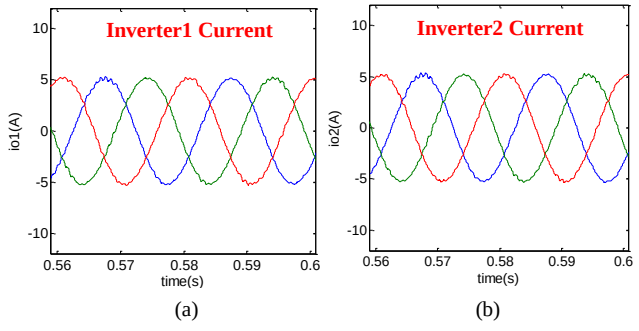

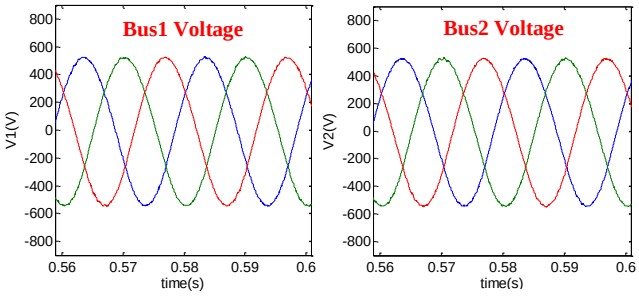

(c) (d)

Fig. 2-11 Simulated stable case if the proportional parameters (K_{pv}) are within stable region (K_{pv}=0.04, K_{pc}=9) [33]. *(a) Inverter1 current. (b) Inverter2 current. (c) Bus1 voltage. (d) Bus2 voltage.*

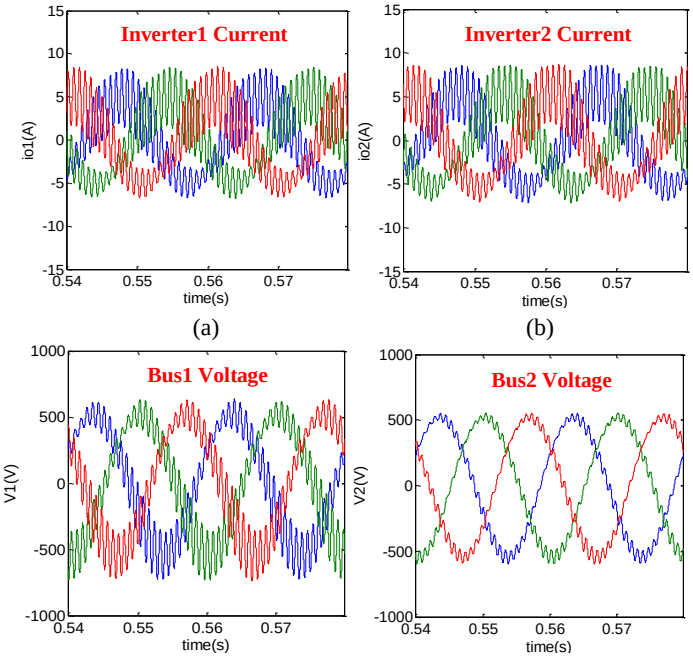

(a) (b)

(c) (d)

Fig. 2-12 Simulated unstable case (K_{pv1}=0.07, K_{pv2}=0.02, K_{pc1}=K_{pc2}=8) [33]. *(a) Inverter1 current. (b) Inverter2 current. (c) Bus1 voltage. (d) Bus2 voltage.*

Fig. 2-12 shows the simulated unstable case with different proportional parameters of voltage controller, where the instability phenomena verify the analytical results from the eigenvalue trace in Fig. 2-7(a) [33].

(2) Harmonic instability phenomena associated with current controller

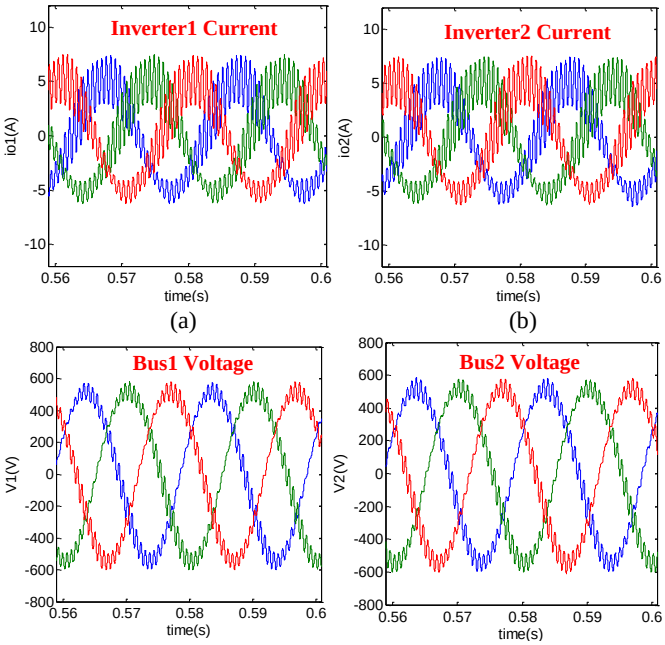

Fig. 2-13 Simulated unstable case if the proportional parameters of current controller (K_{pc}) are within unstable region (K_{pv}=0.04, K_{pc}=12) [33]. *(a) Inverter1 current. (b) Inverter2 current. (c) Bus1 voltage. (d) Bus2 voltage.*

Fig. 2-13 demonstrates the simulated results of unstable case. It can be observed that the oscillation phenomenon happens if the proportional parameters (K_{pc}) of current controller are within unstable region [33]. The inverter currents and bus voltages are depicted in Fig. 2-13(a)-(b) and Fig. 2-13(c)-(d), respectively.

Fig. 2-14 illustrates the simulated unstable case with unequal proportional coefficients (K_{pc}) of the current controller, where the oscillation phenomena validate the analysis results from Fig. 2-7(b) [33]. Besides, the Fig. 2-15 shows that the simulated results of paralleled inverters in stable case when the proportional coefficients (K_{pc}) of current controllers are within the stable region [33].

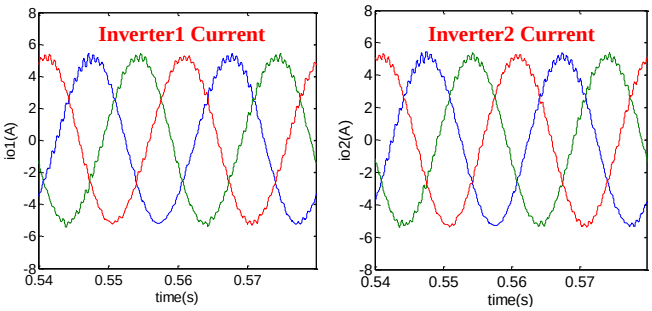

Fig. 2-14 Simulated unstable case (K_{pv1}=K_{pv2}=0.03, K_{pc1}=13, K_{pc2}=8) [33]. *(a) Inverter1 current. (b) Inverter2 current.*

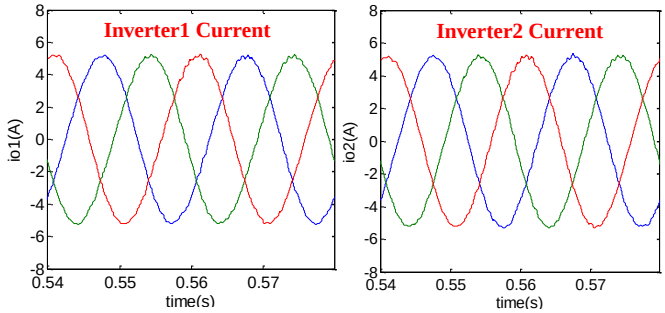

Fig. 2-15 Simulated stable case (K_{pv1}=K_{pv2}=0.03, K_{pc1}=9, K_{pc2}=8) [33]. *(a) Inverter1 current. (b) Inverter2 current.*

2.4.2 Experimental Verification

(1) The effect of voltage controller on harmonic instability

The experimental waveforms of unstable case caused by voltage controller are demonstrated in Fig. 2-16. Once the proportional parameter (K_{pv}) of voltage controller is located in unstable region, the high-frequency oscillation phenomenon will happen [72]. Fig. 2-16(a)-(b) and Fig. 2-16(c)-(d) depict inverters current and network voltages, respectively.

In contrast, the inverter currents and network voltages can be stablized as demonstrated in Fig. 2-17(a)-(b) and Fig. 2-17(c)-(d) once the proportional coefficients of the controllers are reduced. Fig. 2-18 demonstrates the experimental results of unstable case for inverters with unequal coefficients of the voltage controller [72]. The oscillation will occur if the proportional coefficients higher than critcal value of stable region in Fig. 2-18(a) [72].

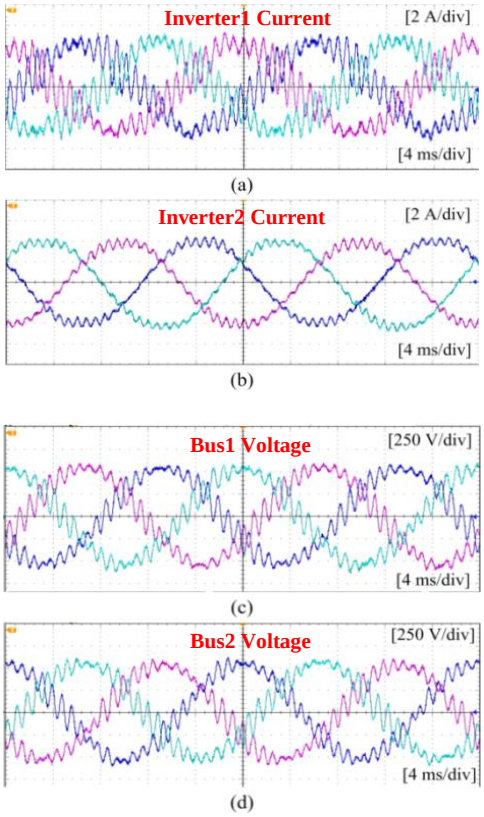

Fig. 2-16. The unstable case induced by the proportional coefficients of voltage controller (K_{pv}=0.053, K_{pc}=8) [72]. *(a) The inverter1 current. (b) The inverter2 current. (c) Voltage at bus1. (d) Voltage at Bus2.*

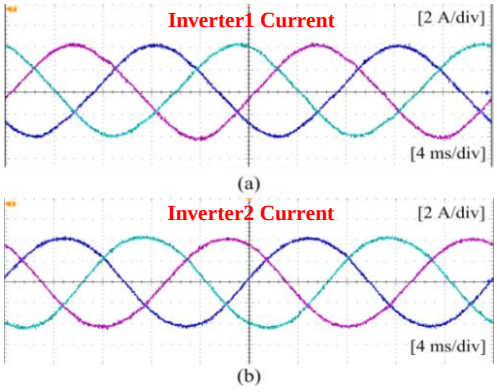

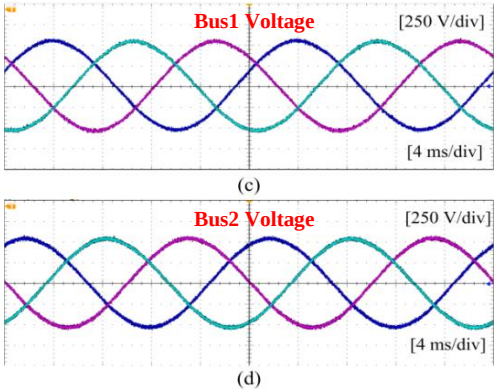

Fig. 2-17. The stable case (K_{pv}=0.035, K_{pc}=8) [72]. *(a) The inverter1 current. (b) The inverter2 current. (c) Voltage at bus1. (d) Voltage at bus2.*

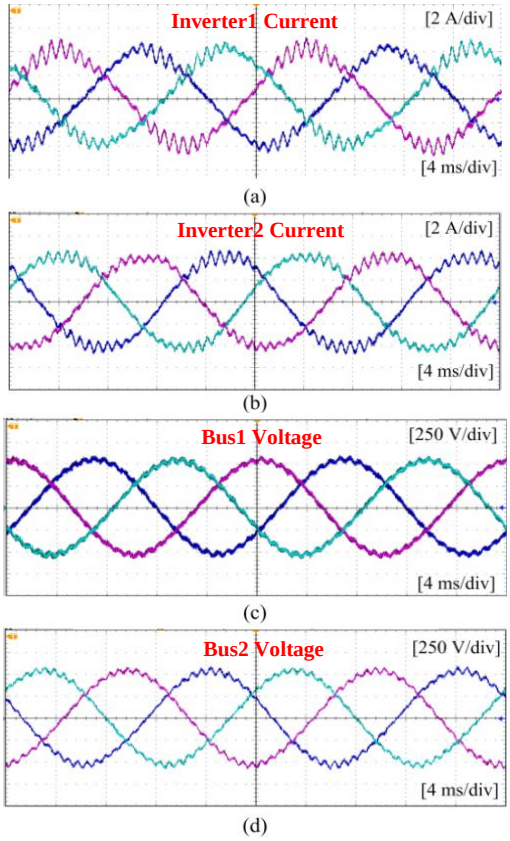

Fig. 2-18. The unstable case (K_{pv1}=0.072, K_{pv2}=0.02, K_{pc1}=K_{pc2}=8) [72]. *(a) The inverter1 current. (b) The inverter2 current. (c) Bus1 Voltage. (d) Bus2 Voltage.*

(2) The effect of current controller on harmonic instability

Fig. 2-19 gives the results of unstable case induced by the coeffcients (K_{pc}) of current controller. The inverter currents and network voltages are given in Fig. 2-19(a)-(b) and Fig. 2-19(c)-(d). It shows that harmonic oscillation phenomenon happens if the proportional coefficients (K_{pc}) of the current controller are higher than 10 [72]. Fig. 2-20 illustrates that the experimental results of unstable case for inverters with unequal proportional coefficients of current controller [72]. The instability phenomena occur once the proportional coefficients are located into unstable region shown in Fig. 2-7(b) [72].

As illustrated in Fig. 2-21, the inverter currents and network voltages are stablized if the proportional coefficients of inverter1 current controller are reduced [72]. The experimental results together with eigenvalue analysis results shown in Fig. 2-5 and Fig. 2-6, indicate that inverters with high proportional coefficients of inner control loop results in the harmonic oscillations [72].

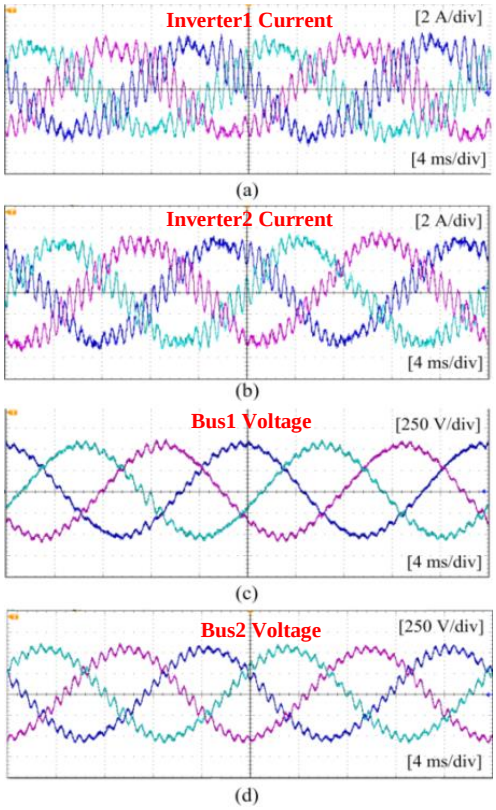

Fig. 2-19. The unstable case (K_{pv}=0.035, K_{pc}=10) [72]. *(a) The inverter1 current. (b) The inverter2 current. (c) Bus1 Voltage. (d) Bus2 Voltage.*

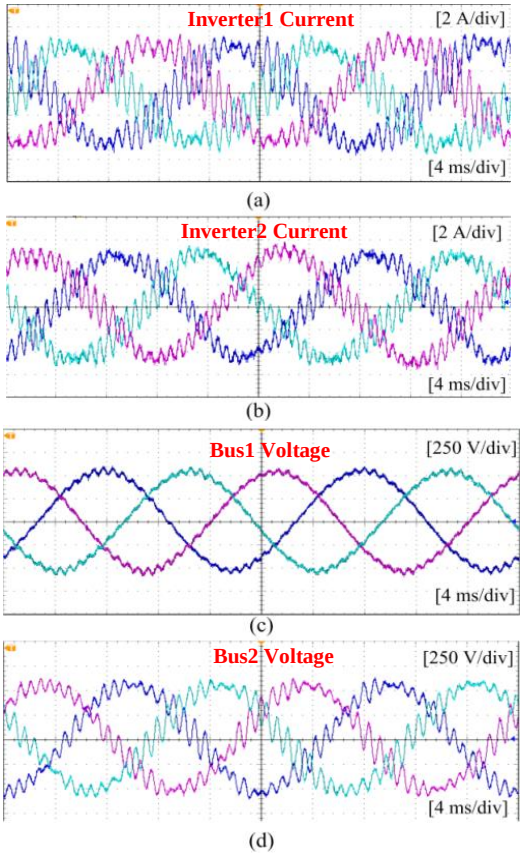

Fig. 2-20. The unstable case (K_{pv1}=K_{pv2}=0.02, K_{pc1}=10, K_{pc2}=8) [72]. *(a) The inverter1 current. (b) The inverter2 current. (c) Bus1 Voltage. (d) Bus2 Voltage.*

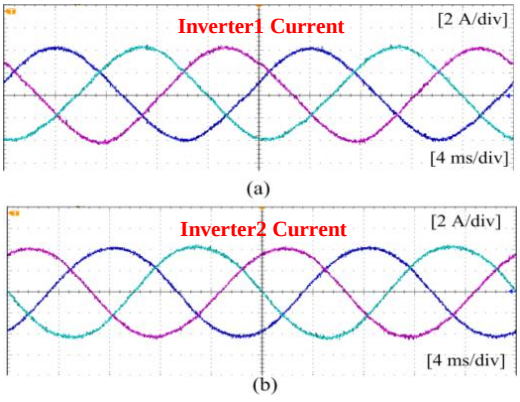

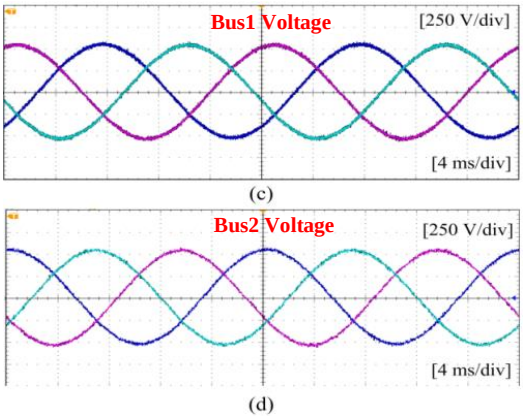

Fig. 2-21. The stable case (K_{pv1}=0.02, K_{pv2}=0.02, K_{pc1}=K_{pc2}=8) [72]. *(a) The inverter1 current. (b) The inverter2 current. (c) Bus1 Voltage. (d) Bus2 Voltage.*

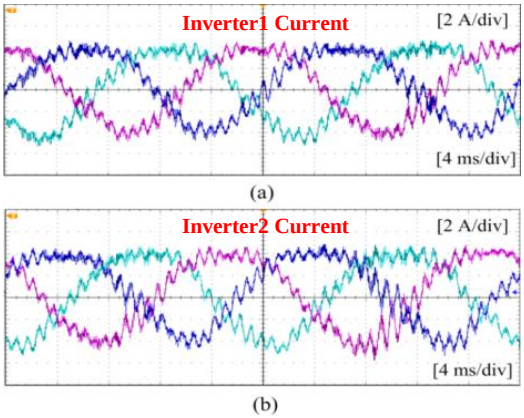

Fig. 2-22. The unstable case with the sampling frequency f_d=8kHz [72]. *(a) The inverter1 current. (b) The inverter2 current.*

Fig. 2-22 depicts the experimental results of unstable case. The experimental result agrees with the eigenvalue analysis results shown in Fig. 2-6.

2.5 Summary

This section develops an eigenvalue-based harmonic-frequency instability assessment method. First, a state-space-based small signal model of individual inverter including time delay, current controller, voltage controller and droop-driven power controller is built. Then, an overall state-space model including inverters, lines and loads is developed. Furthermore, harmonic instability is investigated by analyzing eigenvalue traces, where the contribution of each state on harmonic-frequency oscillation modes can be evaluated through participation analysis [72]. In addition, a reduced-order model applied for harmonic instability assessment is

proposed according to the participation analysis. The analytical results show that the inner current controller, voltage controller and time delay have a critical effect on harmonic instability [72]. The experimental results are given for validating the proposed harmonic instability analysis method.

CHAPTER 3. SMALL SIGNAL STABILITY ASSESSMENT USING COMPONENT CONNECTION METHOD

As reviewed in Chapter1, there are some inherent drawbacks in the state-space modeling and the impedance-based analysis. In order to overcome the drawbacks, this chapter develops a system-level stability criterion by means of Component Connection Method (CCM) [34]. Different from the conventional state-space modeling, the CCM is able to reformulate system model in a computationally-efficient way [105]-[108]. In this procedure, the whole system is divided into different components. These components can be combined together by algebra matrices according to their terminal relationships. Finally, a sparse state matrix can be formulated to represent the composite system model [34].

The CCM is a modular-based modeling approach, which is applicable for the large-scale inverter-fed power system [34]. It is also able to perform sensitivity analysis and identify oscillation origin. The CCM-based modeling and analysis methods have been presented for high voltage direct current systems and the transmission power grid with the Thyristor-based Static Var Compensator [107], [108]. But the implementation of this method for inverter-fed power system has not been studied. The aim of this chapter is to present the CCM-based modeling procedure of inverter-fed power system.

3.1. System description and component connection method

An inverter-fed power system is first illustrated, and then the component connection method applied for small-signal modeling and analysis is demonstrated, which can be applied in large-scale inverter-fed power systems [34].

Fig. 3-1 depicts a circuit configuration of inverter-fed power system with i inverters and i+1 loads. The power system may be divided into different components and each component is connected by internal input-output relationships [34].

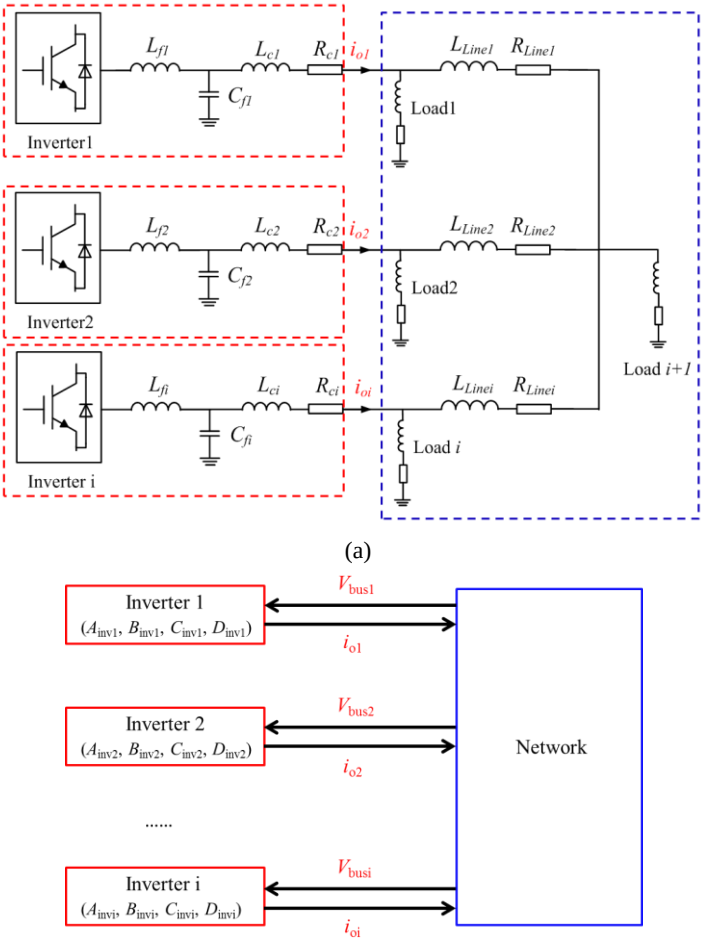

Fig. 3-1. The circuit diagram of inverter-fed power system. (a) Circuit structure. (b) The CCM-based system modeling [34].

The system model of *i*-th component could be given by a set of nonlinear equations [109]-[110] as follows.

$$\dot{x}_i = f_i(x_i, u_i) \tag{3-1}$$

$$y_i = g_i(x_i, u_i) \tag{3-2}$$

where x_i, u_i, y_i means the state variable, input variable, and output variable. The linearized small signal equation of (3-1) and (3-2) can be obtained as (3-3) and (3-4).

$$\Delta\dot{x}_i = A_i \Delta x_i + B_i \Delta u_i \tag{3-3}$$

$$\Delta y_i = C_i \Delta x_i + D_i \Delta u_i \tag{3-4}$$

To permit a simple representation, the sign Δ in (3-3) and (3-4) is neglected in the following. Then, an overall system model can be formulated by combining all the component models as given in (3-5) and (3-6) [34].

$$\dot{x} = Ax + Bu \tag{3-5}$$

$$y = Cx + Du \tag{3-6}$$

where *A,B,C,D* are parameter matrices of system model. $A = diag(A_1, \cdots A_i, \cdots, A_n)$, $B = diag(B_1, \cdots, B_i, \cdots, B_n)$, $C = diag(C_1, \cdots, C_i, \cdots, C_n)$, $D = diag(D_1, \cdots, D_i, \cdots, D_n)$. They are diagonal matrices since these components are connected in diagonal. $x = [x_1, \cdots, x_i, \cdots, x_n]^T$, $u = [u_1, \cdots, u_i, \cdots, u_n]^T$, $y = [y_1, \cdots, y_i, \cdots, y_n]^T$.

As illustrated in Fig. 3-1(b), each component may be represented by a small-signal model with inputs and outputs, the input-output relationship among the different components can be explained by the following equations (3-7) and (3-8) [34]

$$u = L_1 y + L_2 a \tag{3-7}$$

$$b = L_3 y + L_4 a \tag{3-8}$$

where *u* and *y* are seen as component input and output vectors, *a* and *b* are seen as system input and output vectors. L_1, L_2, L_3, L_4 are parameter matrices explaining connection relationship. Finally, the small-signal model based on CCM may be established by combining (3-5)-(3-7) and (3-6)-(3-8) as (3-9) and (3-10) [34].

$$\dot{x} = Fx + Ga \tag{3-9}$$

$$b = Hx + Ja \tag{3-10}$$

where $F = A + BL_1(I - DL_1)^{-1}C$, $G = BL_1(I - DL_1)^{-1}DL_2 + BL_2$, $H = L_3(I - DL_1)^{-1}C$, $J = L_3(I - DL_1)^{-1}DL_2 + L_4$. Then, the small signal stability of system can be investigated by analyzing the eigenvalue traces of the state matrix *F* [34].

3.2. Implementation of the CCM for system modeling

The proposed modeling procedure is demonstrated with reference to the exemplified microgrid shown in Fig. 3-1(a). As illustrated in Fig. 3-1(b), the system is divided into inverter component and network component. The inverter component consists of power controller, voltage controller, current controller, modulation block and filter [34]. All of the components are collected together to formulate the composite model. The modeling and analysis procedure is briefly described in this section.

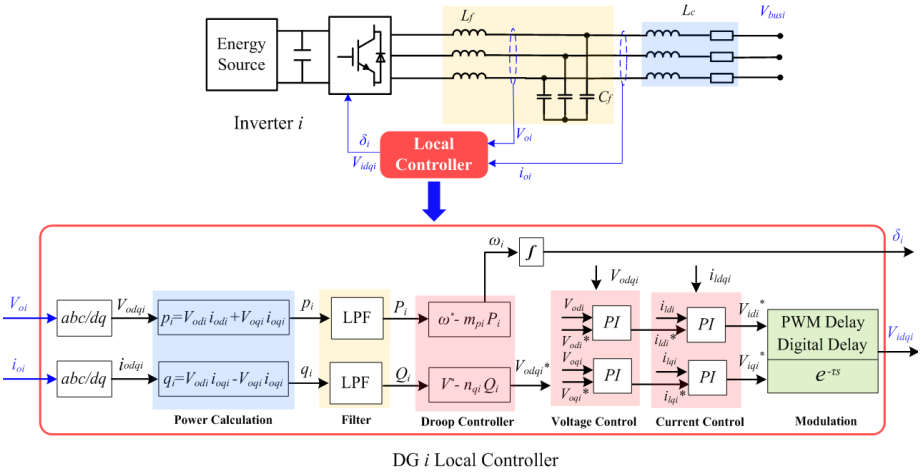

Fig. 3-2. The circuit and control diagram of individual inverter [34].

Fig. 3-2 illustrates the circuit and control diagram of individual inverter, including *LCL*-filter, droop controller, the voltage control loop, the current control loop and the Pulse Width Modulator (PWM) [34].

The droop controller is able to distribute powers among the paralleled inverters. The instantaneous powers can be computed by output voltage and current in *dq* frame [34]. The mean powers obtained from low pass filter are input variables of droop controller. The inner voltage control loop and current control loop are performed by classical PI regulator [34].

To study the influence of digital control delay, the delay model can be represented as (3-11), containing digital computation delay (T_s) and the zero-order hold influence of PWM ($0.5T_s$) [34].

$$V_i = e^{-\tau \bullet s} V_i^* \tag{3-11}$$

Note that V_i^* and V_i are the reference and output voltage. $\tau = 1.5T_s$ is the delay time. The delay representation can be given as (3-12) by the 3-order Pade approximation [34].

$$e^{-\tau \bullet s} \approx \frac{120 - 60(\tau s) + 12(\tau s)^2 - (\tau s)^3}{120 + 60(\tau s) + 12(\tau s)^2 + (\tau s)^3} \tag{3-12}$$

Moreover, the state-space formulation of small-signal model (3-11) can be given as (3-13) and (3-14) [34].

$$\dot{x}_{del} = A_{del} x_{del} + B_{del} V_i^* \tag{3-13}$$

$$V_i = C_{del} x_{del} + D_{del} V_i^* \tag{3-14}$$

where $A_{del}, B_{del}, C_{del}, D_{del}$ are the system matrices. $A_{del} = \begin{bmatrix} A_d & \\ & A_d \end{bmatrix}$, $B_{del} = \begin{bmatrix} B_d & \\ & B_d \end{bmatrix}$, $C_{del} = \begin{bmatrix} C_d & \\ & C_d \end{bmatrix}$, $D_{del} = \begin{bmatrix} D_d & \\ & D_d \end{bmatrix}$, $A_d = \begin{bmatrix} 0 & 1 & 0 \\ 0 & 0 & 1 \\ -120/\tau^3 & -60/\tau^2 & -12/\tau \end{bmatrix}$, $B_d = [0 \quad 0 \quad 1]^T$, $C_d = [240/\tau^3 \quad 0 \quad 24/\tau]^T$, $D_d = [-1]^T$, $V_i^* = [V_{id}^*, V_{iq}^*]$, $V_i = [V_{id}, V_{iq}]$. $x_{del} = [x_{dq1}, x_{dq2}, x_{dq3}]^T$ is state vector of small signal model (3-13).

Fig. 3-3 depicts the power angle relationship among different inverters, where the *dq* frame of inverter1 is defined as common frame (DQ), and the small signal dynamics of remaining inverters and power network are converted into common frame [21].

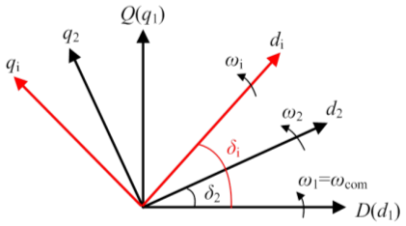

Fig. 3-3. Power angle relationship among different inverters.

The power angle relationship of the *i*th inverter is given as (3-15) [34].

$$\delta_i = \int (\omega_i - \omega_{com}) dt \tag{3-15}$$

Furthermore, the state-space form of (3-15) may be written as (3-16) and (3-17) [34].

$$\dot{x}_c = A_c x_c + B_c u_c \tag{3-16}$$

$$y_c = C_c x_c + D_c u_c \tag{3-17}$$

where $x_c = [\delta_i]$, $u_c = [\omega_i, \omega_{com}]^T$, $y_c = [\delta_i]$, $A_c = 0$, $B_c = [1 \quad -1]$, $C_c = 1$, $D_c = [0 \quad 0]$.

The small signal dynamic of power controller is shown in Fig. 3-2. The mathematical model of the power controller is formulated by assembling these component models, which is represented as (3-18) and (3-19) [34].

$$\dot{x}_1 = A_1 x_1 + B_1 u_1 \tag{3-18}$$

$$y_1 = C_1 x_1 + D_1 u_1 \tag{3-19}$$

where $x_1 = [P_1, Q_1]^T$ are state variables of active power and reactive power, $u_1 = [V_{odi}, V_{oqi}, i_{odi}, i_{oqi}]^T$ is the input vector, $y_1 = [V_{odi}^*, V_{oqi}^*, \omega_i]^T$ is the output vector, and A_1, B_1, C_1, D_1 are parameter matrices of the droop controller model (3-18)-(3-19).

$A_1 = \begin{bmatrix} -\omega_c & 0 \\ 0 & -\omega_c \end{bmatrix}$, $B_1 = \begin{bmatrix} \omega_c i_{odi0} & \omega_c i_{oqi0} & \omega_c V_{odi0} & \omega_c V_{oqi0} \\ \omega_c i_{oqi0} & -\omega_c i_{odi0} & -\omega_c V_{oqi0} & \omega_c V_{odi0} \end{bmatrix}$, $C_1 = \begin{bmatrix} 0 & -n_{qi} \\ 0 & 0 \\ -m_{pi} & 0 \end{bmatrix}$, $D_1 = [0_{2\times 4}]$.

$i_{odi0}, i_{oqi0}, V_{odi0}, V_{oqi0}$ are the initial operation point of the inverter currents and voltages.

As illustrated in Fig. 3-2, each inverter includes droop controller, inner current and voltage loop, as well as PWM block [34]. The state-space form of each inverter is derived by combining delay model, angle relationship, droop controller, inner voltage and current control loops as well as filter as (3-20) and (3-21) [34].

$$\dot{x}_{invi} = A_{invi} x_{invi} + B_{invi} u_i \tag{3-20}$$

$$y_i = C_{invi} x_{invi} \tag{3-21}$$

$x_{invi} = \left[\delta_i, P_i, Q_i, \varphi_{dqi}, \gamma_{dqi}, i_{ldqi}, v_{odqi}, i_{odqi}, x_{del}\right]^T$ is inverter state variable, containing the power angle state (δ_i), active power and reactive power (P_i, Q_i), states of voltage controller (φ_{dqi}), states of current controller (γ_{dqi}), states of *LCL* filter (i_{ldqi}, v_{odqi}, i_{odqi}), as well as delay states (x_{del}). u_i = [i_{odqi}^*, V_{busi}] is input vector, including bus voltages (V_{busi}) and command current (i_{odqi}^*). The component output (y_i) is inverter current (i_{odqi}), which connects power network.

In fact, the closed-loop output admittance gain may be obtained through the ratio of output current to inverter input from (3-20) and (3-21), which accounts for inverter terminal characteristic [78].

$$Y_o = \frac{i_{oi}(s)}{u_i(s)} = C_{invi}(sI - A_{invi})^{-1} B_{invi} \tag{3-22}$$

It is understood that closed-loop admittance can be obtained by the ratio of output to input if the voltage (V_{busi}) is defined as inverter input. Also, the closed-loop gain can be derived if the reference current (i_{odqi}^*) is defined as input [34]. The terminal performance revealing oscillation factors of inverter will be investigated in section 3.3.

Fig. 3-4 depicts the circuit diagram of network and loads, which is modeled as individual components.

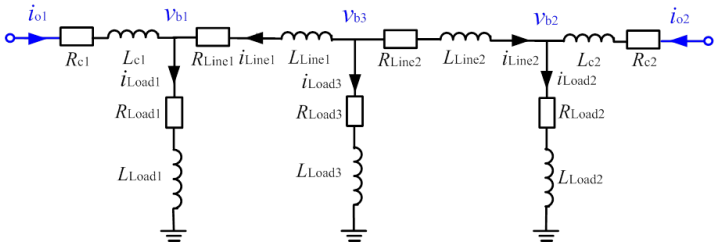

Fig. 3-4. Circuit diagram of network and loads [34].

The current dynamic equation of network on common rotating frame may be established as (3-23)

$$\dot{i}_{LineDi} = \frac{-R_{Linei}}{L_{Linei}} i_{LineDi} - \omega i_{LineQi} - \frac{1}{L_{Linei}} v_{bDi} + \frac{1}{L_{Linei}} v_{bD3} \quad (i=1,2,3) \tag{3-23}$$
$$\dot{i}_{LineQi} = \frac{-R_{Linei}}{L_{Linei}} i_{LineQi} + \omega i_{LineDi} - \frac{1}{L_{Linei}} v_{bQi} + \frac{1}{L_{Linei}} v_{bQ3}$$

The small signal model of lines can be built as (3-24) by linearizing (3-23) [34]

$$\Delta \dot{i}_{LineDQi} = A_{Line1i} \Delta\omega_1 + A_{Line2i} \Delta i_{LineDQi} + A_{Line3i} v_{bDQi} + A_{Line4i} v_{bDQ3} \tag{3-24}$$

where $A_{Line1i} = \begin{bmatrix} -i_{LineQi0} \\ i_{LineDi0} \end{bmatrix}$, $A_{Line2i} = \begin{bmatrix} \frac{-R_{Linei}}{L_{Linei}} & -\omega_0 \\ \omega_0 & \frac{-R_{Linei}}{L_{Linei}} \end{bmatrix}$, $A_{Line3i} = \begin{bmatrix} \frac{-1}{L_{Linei}} & 0 \\ 0 & \frac{-1}{L_{Linei}} \end{bmatrix}$,

$A_{Line4i} = \begin{bmatrix} \frac{1}{L_{Linei}} & 0 \\ 0 & \frac{1}{L_{Linei}} \end{bmatrix}$

The small signal equations of loads on common frame are established as (3-25).

$$\dot{i}_{LoadDi} = \frac{-R_{Loadi}}{L_{Loadi}} i_{LoadDi} - \omega i_{LoadQi} + \frac{1}{L_{Loadi}} v_{bDi} \quad (i=1,2,3) \tag{3-25}$$
$$\dot{i}_{LoadQi} = \frac{-R_{Loadi}}{L_{Loadi}} i_{LoadQi} + \omega i_{LoadDi} + \frac{1}{L_{Loadi}} v_{bQi}$$

The small signal model of loads may be built as (3-26) through (3-25)

$$\Delta \dot{i}_{LoadDQi} = A_{Load1i} \Delta\omega + A_{Load2i} \Delta i_{LoadDQi} + A_{Load3i} v_{bDQi} \quad (i=1,2,3) \tag{3-26}$$

where $A_{Load1i} = \begin{bmatrix} -i_{LoadQi0} \\ i_{LoadDi0} \end{bmatrix}$, $A_{Load2i} = \begin{bmatrix} \frac{-R_{Loadi}}{L_{Loadi}} & -\omega_0 \\ \omega_0 & \frac{-R_{Loadi}}{L_{Loadi}} \end{bmatrix}$, $A_{Load3i} = \begin{bmatrix} \frac{1}{L_{Loadi}} & 0 \\ 0 & \frac{1}{L_{Loadi}} \end{bmatrix}$

Then, artificial resistors are adopted to define bus voltages between node and ground for simplifying network model [21]. The bus voltages may be established on DQ common frame by linear combinations of current states as (3-27) and (3-28) [34]

$$v_{bDQi} = r_N (i_{oDQi} + i_{LineDQi} - i_{LoadDQi}) \tag{3-27}$$

$$v_{bDQ(i+1)} = r_N (-i_{LineDQ1} - \cdots - i_{LineDQi} - \cdots - i_{LoadDQ(i+1)}) \tag{3-28}$$

Further, the small-signal dynamic model of the network and loads are built by (3-24), (3-26)-(3-28) as (3-29) [34]

$$\dot{x}_{net} = A_{net} x_{net} + B_{net} u_{net} \tag{3-29}$$
$$y_{net} = C_{net} x_{net} + D_{net} u_{net}$$

$x_{net} = \left[i_{LineDQ1}, \cdots, i_{LineDQi}, i_{LoadDQ1}, \cdots, i_{LoadDQi} \right]^T$ are state variables of lines current and loads current, $A_{net} = diag(A_{Line21}, A_{Line22}, A_{Load21}, A_{Load22}, A_{Load23})$, $u_{net} = \left[i_{odq1}, \cdots, i_{odqi}, \delta_1, \cdots, \delta_i, \omega_1 \right]^T$, $y_{net} = \left[i_{odq1}, \cdots, i_{odqi} \right]^T$.

A composite system model can be obtained by combining component models as (3-30) [34]

$$\begin{aligned} \dot{x} &= A_T x + B_T u \\ y &= C_T x + D_T u \end{aligned} \tag{3-30}$$

$A_T = diag(A_{DG1}, \cdots, A_{DGi}, A_{net})$, $B_T = diag(B_{DG1}, \cdots, B_{DGi}, B_{net})$, $C_T = diag(C_{DG1}, \cdots, C_{DGi}, C_{net})$, $D_T = diag(D_{DG1}, \cdots, D_{DGi}, D_{net})$, $x = \left[x_{DG1}, \cdots, x_{DQi}, x_{net} \right]^T$ are state variables of inverter and network. Interconnection relationship among components can be represented as (3-31) [34]

$$u = L_T y \tag{3-31}$$

The final small signal model of whole system then may be derived by combining (3-30) and (3-31) according to (3-9) and (3-10) as (3-32) [34]

$$\dot{x} = Fx \tag{3-32}$$

where $F = A_T + B_T L_T (I - D_T L_T)^{-1} C_T$. The small-signal stability of the whole system may be predicted by analyzing the eigenvalue traces of state matrix (*F*), which will be done in the next part [34].

To investigate the steady-state performance of the proposed small signal model, the experimental verification is performed, where a step load of 4kw and 6kvar is arranged at bus3. Fig. 3-5 - Fig. 3-6 show the experimental results of small signal model, where the state responses of the active power, reactive power, d-axis current and q-axis current are shown in Fig. 3-5(a)-(d) and Fig. 3-6(a)-(d). It can be seen that the responses obtained from the small signal model matches with the state responses obtained from the experimental system.

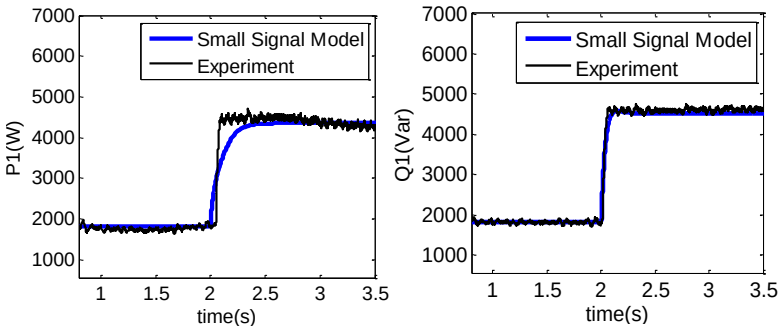

(a) (b)

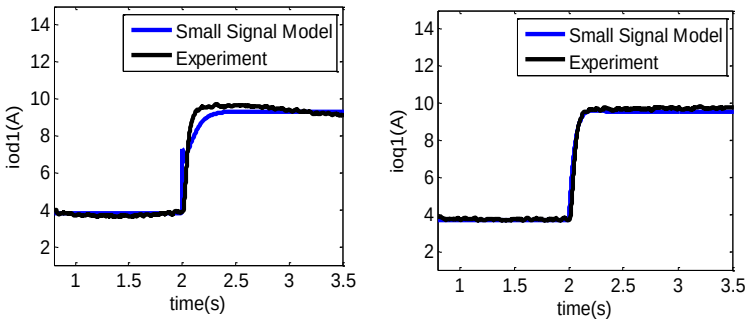

(c) (d)

Fig. 3-5. Step response of inverter 1. (a) Active power response. (b) Reactive power response. (c) Output current (d-axis) response of stable case. (d) Output current (q-axis) response of stable case.

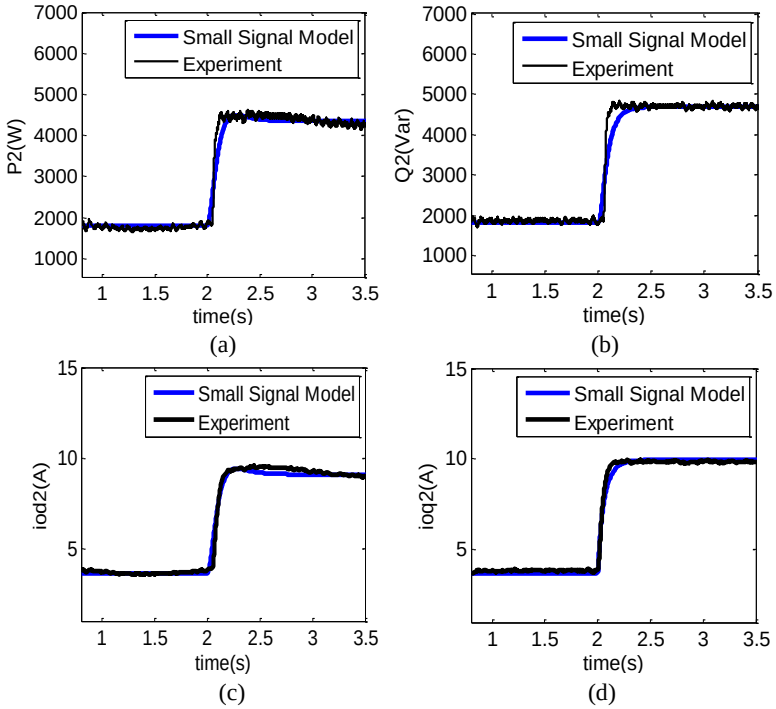

(a) (b)

(c) (d)

Fig. 3-6. Step responses of inverter 2. (a) Active power response. (b) Reactive power response. (c) Output current (d-axis) response. (d) Output current (q-axis) response.

3.3 Terminal performance of inverter

Terminal performance may be revealed by frequency response of inverter output admittance, which is able to explain the contributions of control loops parameters in

different frequency region [34]. Fig. 3-7 demonstrates that terminal performance of single inverter as the growth of reactive power-voltage droop parameter (n_p) from 1e-3 to 5e-3, where the frequency characteristic and eigenvalues of inverter is demonstrated in Fig. 3-7(a) and Fig. 3-7(b). To explain the influence of controller parameters, the time delay is not incorporated in the case [34]. It can be observed that the terminal performance of inverter in low frequency range (1Hz-40Hz) is primarily influenced by the reactive power droop gain, whereas the terminal performance in high-frequency region is hardly influenced [34].

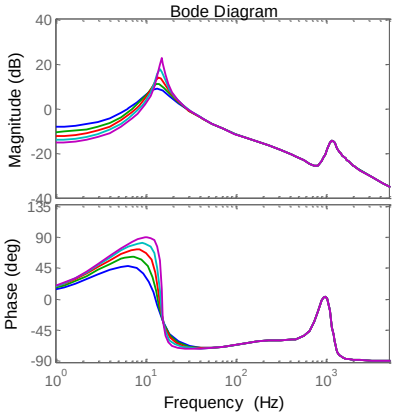

(a)

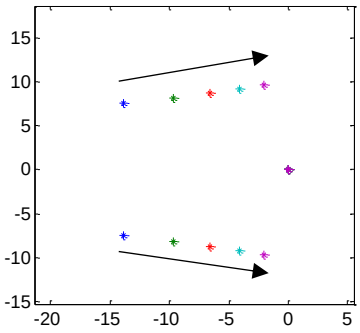

(b)

Fig. 3-7. Terminal behavior of inverter as the growth of droop gain from 1e-3 to 5e-3 without incorporating time delay [34]. *(a). Frequency characteristic at inverter terminal. (b). Eigenvalue trajectory of individual inverter.*

Fig. 3-8 illustrates the terminal behavior of inverter when the proportional coefficient of voltage control loop increases, where the frequency response is depicted in Fig. 3-8(a) and eigenvalue trace is depicted in Fig. 3-8(b). In addition, the Fig. 3-9 demonstrates the inverter terminal behavior when the proportional coefficient of current controller increases [34]. In summary, the proportional parameters associated with current and voltage control loops have essential

influences on harmonic-frequency characteristic (500 Hz-1000 Hz). Meanwhile, the eigenvalue trajectory of inverter reveals the identical influence in harmonic-frequency range [34].

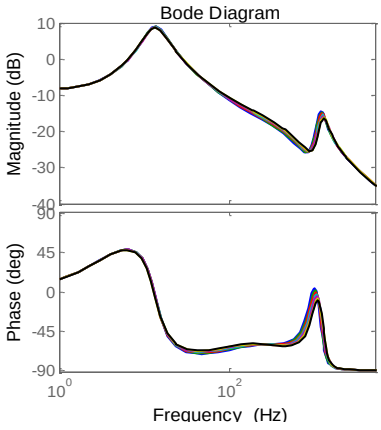

(a)

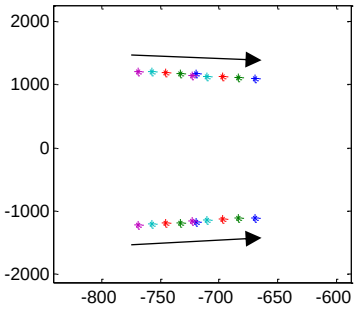

(b)

Fig. 3-8. Terminal behavior of inverter when the proportional parameter of voltage controller increases from 0.01 to 0.05 without inserting time delay [34]. *(a). Inverter terminal frequency behavior. (b). Inverter eigenvalue trajectory.*

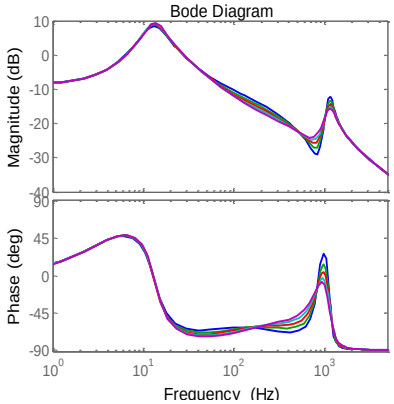

(a)

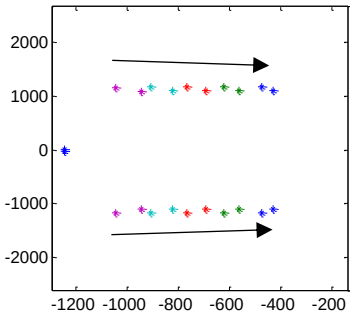

(b)

Fig. 3-9. Inverter terminal performance when the proportional coefficient of current controller increases from 2 to 6 without incorporating time delay [34]. *(a). Inverter terminal frequency response. (b). Eigenvalue trajectory of individual inverter.*

Furthermore, the terminal characteristic would be primarily affected if digital control delay is considered [34]. Fig. 3-10 depicts the inverter frequency response with the decrease of sampling frequency.

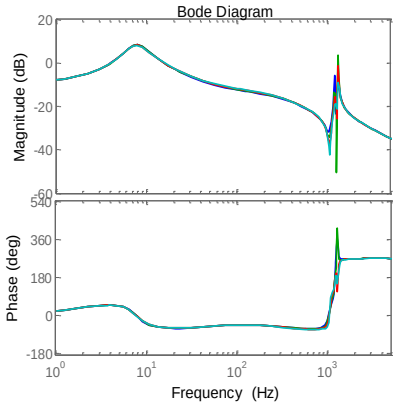

(a)

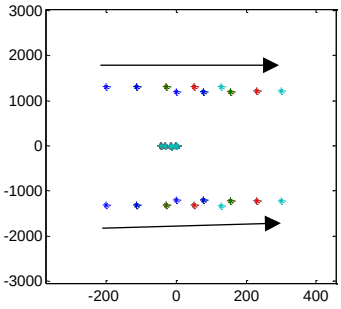

(b)

Fig. 3-10. Inverter terminal performance when the proportional parameters of voltage controller increase considering time delay [34]. *(a). Inverter terminal frequency response. (b). Inverter eigenvalue trajectory.*

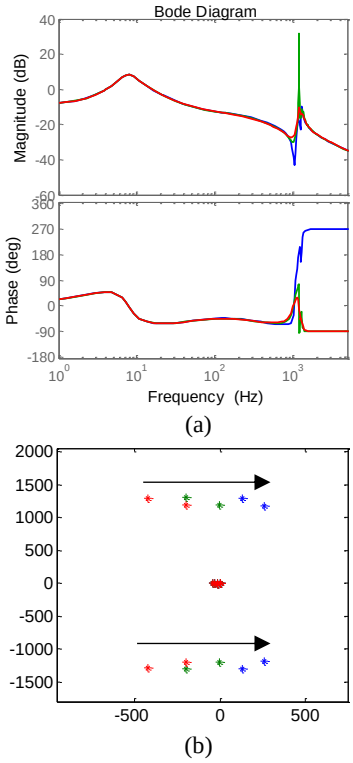

Fig. 3-11. Inverter terminal characteristic if the sampling time increases (T_s=1/10000, 1/8000, 1/6000) [34]. *(a). Inverter terminal frequency response. (b). Inverter eigenvalue trajectory.*

Fig. 3-11 demonstrates the frequency response of inverter output admittance when the sampling time increases, where the digital control delay exerts an essential effect on harmonic-frequency characteristic of inverter [34].

The frequency response shown in Fig. 3-8-Fig. 3-11 explains that the controller parameters in multiple control loops have different contributions on inverter dynamic performance in wide frequency range [34].

3.4 Low-frequency stability

Oscillation and damping characteristic of the power system can be revealed according to the eigenvalues of state matrix [30]. In this section, the eigenvalue trace of state matrix (F) may be obtained to predict the system dynamic stability in different frequency range [34]. The parameters of exemplified system are given in Table 3-1.

TABLE 3-1 Test System Parameters [34]

Parameter	Value	Parameter	Value
Rated Voltage (Phase-to-Ground)	220 V	Frequency	50 Hz
DC-link Voltage	750V	Switching Frequency	10 kHz
L_{f1}/L_{f2}	1.5 mH/1.5 mH	T_s	100 μs
C_{f1}/C_{f2}	25 μF/25 μF	L_{Load1}/R_{Load1}	155 mH/64 Ω
L_{c1}/L_{c2}	1.8 mH/1.8 mH	L_{Load2}/R_{Load2}	156 mH/64 Ω
L_{Line1}/R_{Line1}	1.8 mH/0.2 Ω	L_{Load3}/R_{Load3}	245 mH/80 Ω
L_{Line2}/R_{Line2}	1.8 mH/0.2 Ω		

3.4.1 Low-frequency stability assessment

A power system with 2 paralleled inverters shown in Fig. 3-2 is first modelled to investigate low-frequency oscillation, which is highly sensitive to active power and reactive power droop coefficients [34]. As depicted in Fig. 3-12, the low-frequency (20-70 rad/s) eigenvalue trajectory moves toward right-half plane (unstable region) as the increase of droop coefficient (m_p) from 0.1e-3 to 3e-3 [34]. Hence, the low-frequency modes are highly sensitivie to the dynamics of active power sharing [34].

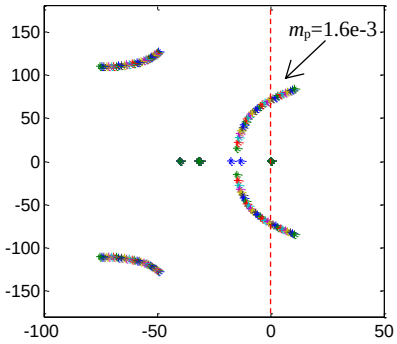

Fig. 3-12. Low-frequency eigenvalue trajectory with an increase of active power droop coefficients of power controller (m_p) from 0.1e-3 to 3e-3 [34].

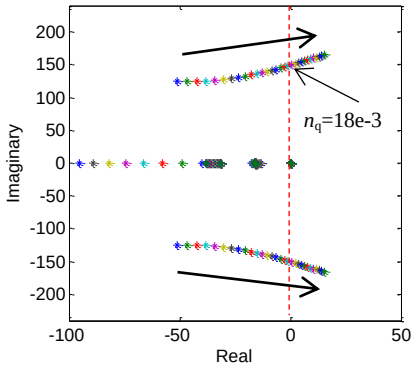

Fig. 3-13. Low-frequency eigenvalue trajectory with the increase of reactive power droop gain of power controllers (n_q) from 1e-3 to 30e-3 [34].

Also, Fig. 3-13 depicts that the low-frequency eigenvalue trajectory moves towards the right-half plane (unstable region) when reactive power droop coefficient increases.

3.4.2 Simulation and experiment

To verify the proposed stability analysis method, the simulation and experimental verification are performed in this section. The parameters of test system are provided in Table 3-1. And the circuit configuration is depicted in Fig. 3-14. In the implementation of simulation and experiments, the control is performed in the discrete domain with a sampling frequency of 10 kHz.

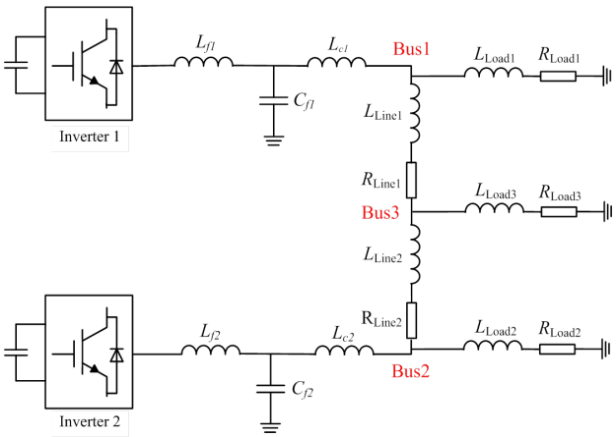

Fig. 3-14. System circuit configuration [34].

(1) Simulation results

Fig. 3-15 depicts that the simulated results of low-frequency oscillation phenomenon with the increase of the active power droop coefficient (m_p) [34]. And the Fig. 3-

15(a)-(b) shows the three-phase output current of inverters. Also, Fig. 3-15(c)-(d) shows the active and reactive power of inverters, respectively. It can be seen that the low-frequency oscillation phenomenon (10 Hz) happens in current and power responses [34], which verifies the analysis results shown in Fig. 3-12.

Fig. 3-16 shows that the simulated current responses in the low-frequency oscillation when the reactive power droop gain (n_q) of the power controllers increase [34]. Fig. 3-16(a)-(b) shows the output current of inverters. Also, Fig. 3-16(c)-(d) shows the output power of inverter 1 and inverter2, respectively. It can be seen that the low-frequency oscillation phenomenon (20 Hz) happens in the current and power responses [34], which agrees with the analysis results shown in Fig. 3-13.

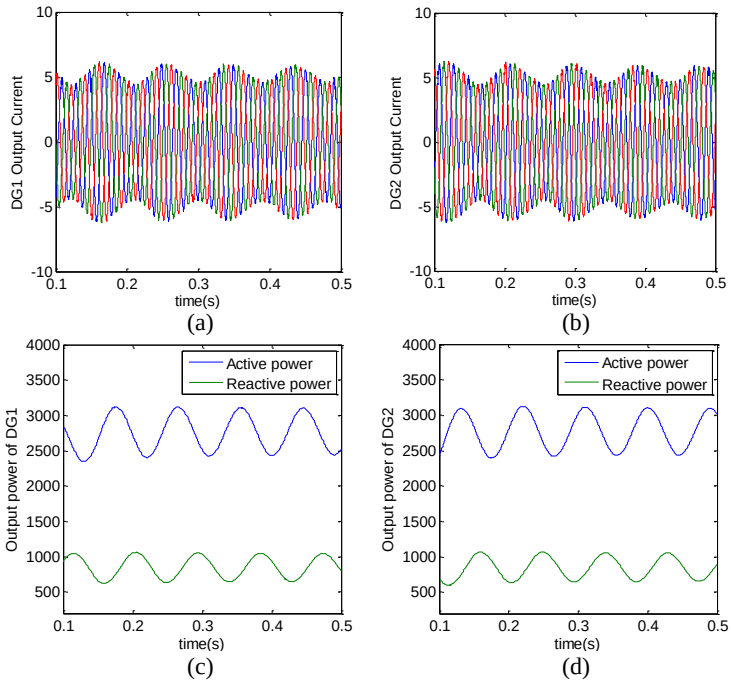

Fig. 3-15. Simulation results in low-frequency oscillation case (m_p=0.62e-3, n_p=1e-3) [34]. *(a) Output current of inverter1. (b) Output current of inverter2. (c) Output power of inverter1. (c) Output power of inverter2.*

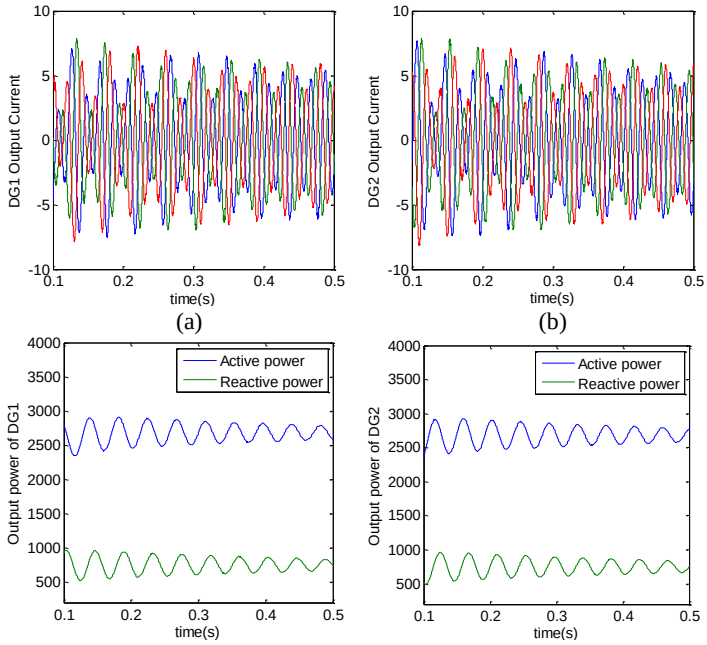

Fig. 3-16. Simulation results of the low-frequency oscillation case (m_p =1e-4, n_p =12e-3) [34]. *(a) Inverter1 output current. (b) Inverter2 output current. (c) Inverter1 output power. (c) Inverter2 output power.*

(2) Experimental results

The experimental results of low-frequency oscillation case are shown in Fig. 3-17 when the active power droop gain (m_p) is increased, where the Fig. 3-17(a)-(b) and Fig. 3-17(c)-(d) show the output current and output power of inverters [34].

The experimental results of the low-frequency oscillation case are depicted in Fig. 3-18 when the reactive power droop gain (n_q) is increased, where the Fig. 3-18(a)-(b) and Fig. 3-18(c)-(d) depicts the output current and output power of inverters [34].

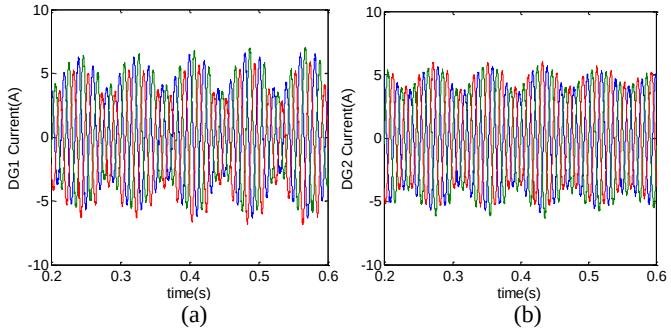

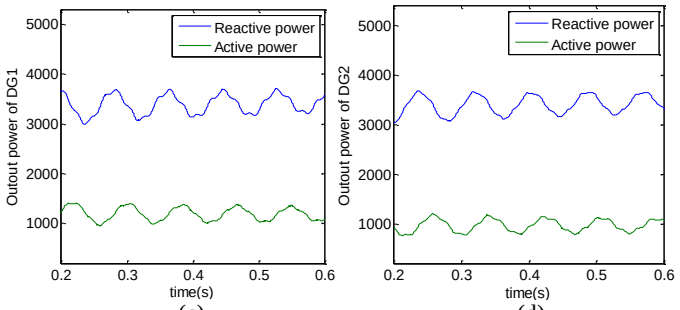

Fig. 3-17. Experimental results of the low-frequency oscillation phenomenon (m_p=0.62e-3, n_p=1e-3) [34]. *(a) Output current of inverter1. (b) Output current of inverter2. (c) Output power of inverter1. (c) Output power of inverter2.*

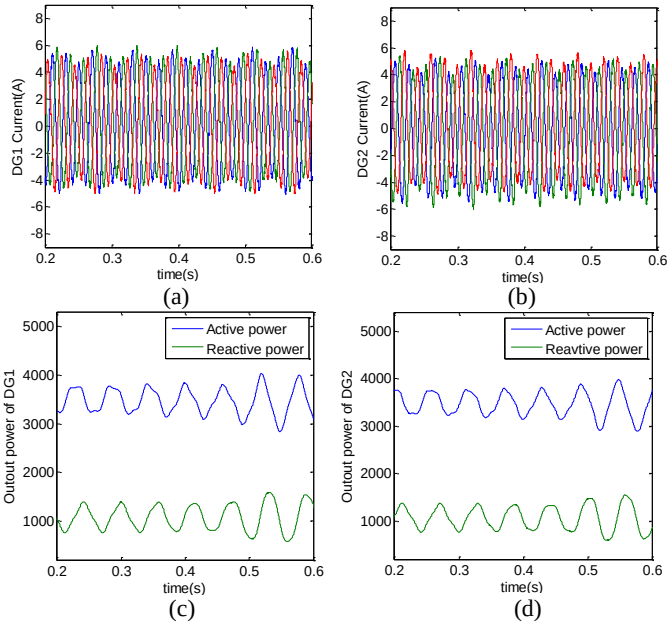

Fig. 3-18. Experimental results of low-frequency oscillation phenomenon (m_p = 0.1e-3, n_p = 18e-3) [34]. *(a) Output current of inverter1. (b) Output current of inverter2. (c) Output power of inverter1. (c) Output power of inverter2.*

3.5 Harmonic-frequency stability

3.5.1 Harmonic-frequency stability assessment

The harminic-frequency oscillation is also studied for the inverter-fed power system shown in Fig. 3-1. Fig. 3-19 depicts the eigenvalue trajectory of the overall model (3-32) as variation of the proportional coefficient of voltage controllers [34]. It can

be observed that two harmonic-frequency conjugate pairs are to large extent sensitive to the parameter, which reveals the dynamics of harmonic frequency [34].

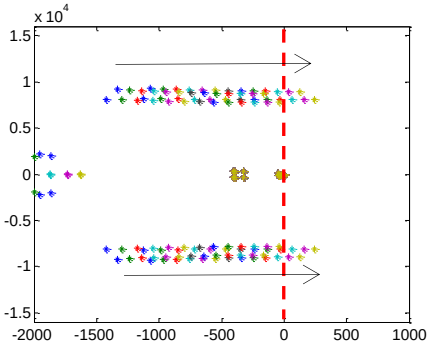

Fig. 3-19. Harmonic-frequency eigenvalue trace with the increase of proportional coefficient of voltage controller (K_{pv}) from 0 to 0.06 [34].

Fig. 3-19 demonstrates the harmonic frequency eigenvalue trace as the increase of the proportional coefficient of current controller from 2 to 12, where the modes move toward the unstable region if the parmaeter (K_{pc}) is increased [34]. The system would become unstable if K_{pc} is higher than 9 [34].

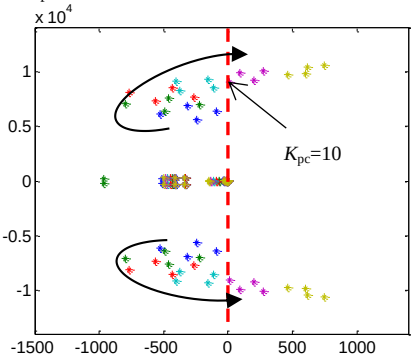

Fig. 3-20 Harmonic-frequency eigenvalue trace when the proportional coefficient of current controller (K_{pc}) is increased from 2 to 12 [34].

To simplify the network equations, virtual resistors can be introduced to define node voltages in some previous work [34]. Fig. 3-21 depicts that the movement of eigenvalue trace if the virtual resistor is increased from 600 Ω to 800 Ω [34]. It shows that virtual resistors exert important influence on the fundamental frequency oscillation modes (50Hz), and slightly affect the harmonic-frequency modes.

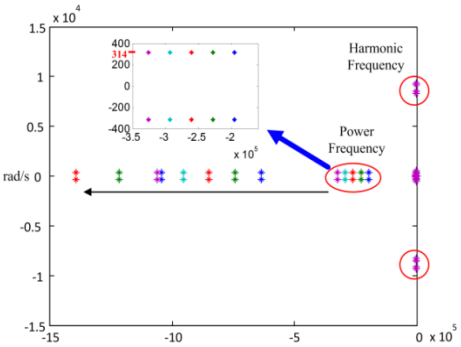

Fig. 3-21. The influence of virtual resistor on system stability when r_n is increased from 600 Ω to 1000 Ω [34].

To further explain the contributions of this work considering digital control delay, a comparison analysis between this work and previous work is provided as shown in Fig. 3-22.

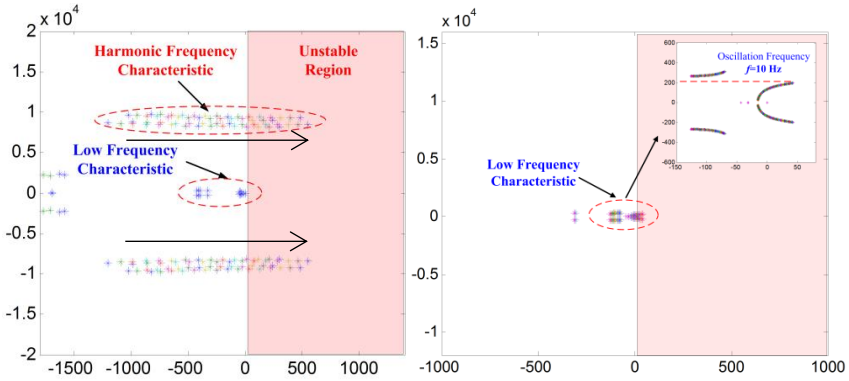

(a) (b)

Fig. 3-22. Comparison explanation of the proposed model and the previous model [34]. *(a) Stability analysis for overall model with considering time delay. (b) Stability analysis for overall model without considering time delay*.

Fig. 3-22(a) depicts that the eigenvalue trajectory of overall model considering digital control delay. It can be observed that the delay model has an essential influence on harmonic-frequency instability with oscillation frequency 10000 rad/s (1.6kHz) [34]. The harmonic-frequency eigenvalues move to unstable range due to increase of proportional coefficients of inner controller. Also, the Fig. 3-22(b) demonstrates the stability analysis result without considering digital control delay, where the harmonic-frequency characteristic is missing completely, and only low frequency modes with oscillation frequency 10Hz are shown here [34]. Hence, the proposed analysis incorporating time delay model provides more complete and accurate oscillation characteristics [34].

3.5.2 Simulation and experiment

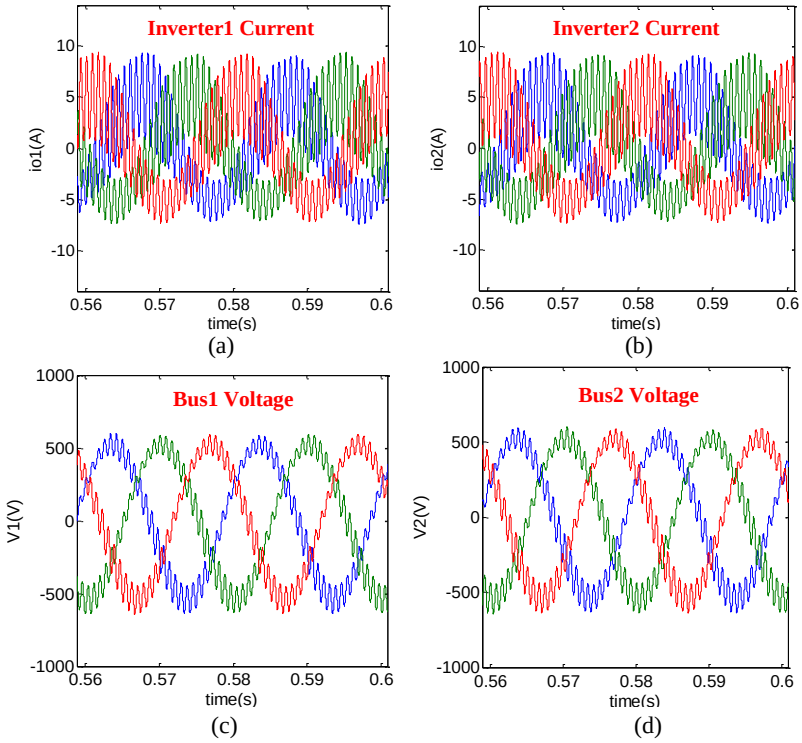

Fig. 3-23. Simulation results of unstable case (K_{pv} = 0.056, K_{pc} = 8) [34]. *(a) Output current of inverter1. (b) Output current of inverter2. (c) Bus1 voltage (phase-to-phase). (d) Bus2 voltage (phase-to-phase).*

Fig. 3-23 depicts that the simulated results of the unstable case. The output current of the inverters and bus voltages are depicted in Fig. 3-23(a)-(b) and Fig.3-23(c)-(d). It can be observed that the harmonic-frequency oscillation phenomenon occurs if the proportional coefficients (K_{pv}) are selected as 0.056 [34].

Once the proportional coefficients (K_{pv}=0.04, K_{pc}=8) are reduced, the output current of DG units and bus voltages are stablized as shown in Fig. 3-24(a)-(b) and Fig. 3-24(c)-(d) [34]. The simulated results, accompanying with analysis results from Fig. 3-11 and Fig. 3-12, explain that the inverter with the high gains of voltage and current loop causes harmonic-frequency oscillation [34].

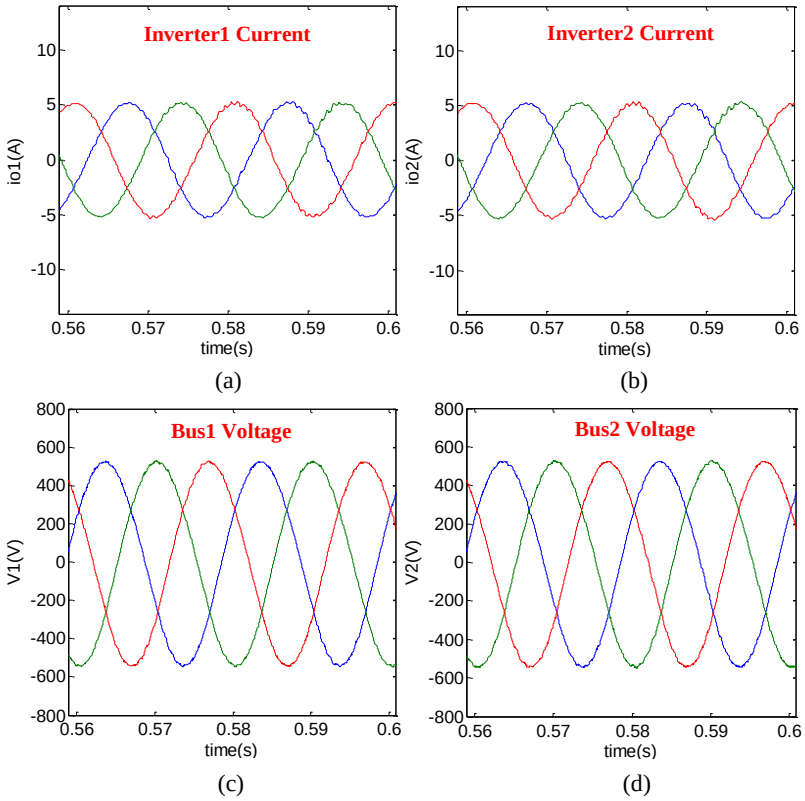

Fig. 3-24. Simulated results of stable case (K_{pv} =0.04, K_{pc} =8) [34]. *(a) Output current of inverter1. (b) Output current of inverter2. (c) Bus1 voltage. (d) Bus2 voltage.*

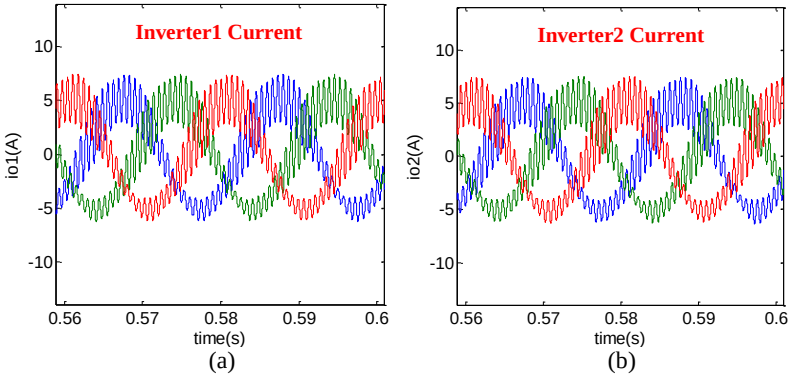

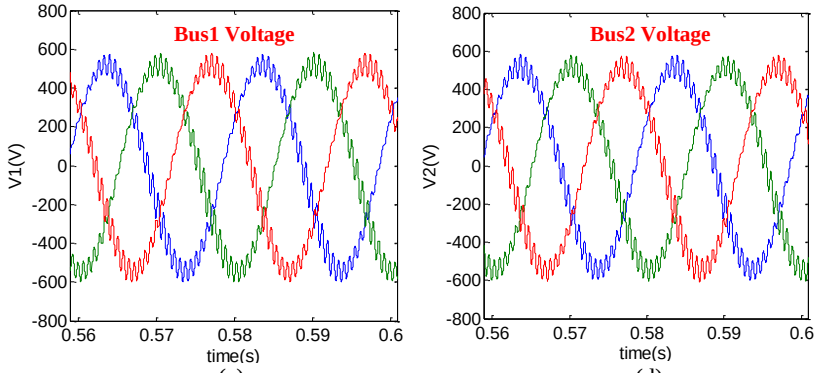

(c) (d)

Fig. 3-25. Simulated results of unstable case if the coefficients of current controller (K_{pi}) are located into unstable region (K_{pv}=0.04, K_{pc}=12) [34]. *(a) Output current of inverter1. (b) Output current of inverter2. (c) Bus1 voltage. (d) Bus2 voltage.*

Fig. 3-25 illustrates that the simulated results of unstable case if the proportional coefficients (K_{pc}) of current controller is selected into unstable region [34]. The output current of DG inverters and bus voltages are denmonstrated in Fig. 3-25(a)-(b) and Fig. 3-25(c)-(d), separately. The high-frequency oscillation occurs when the proportional coefficients (K_{pc}) of current controller are selected as 12 [34].

Fig. 3-26 illustrates the experimental results of unstable case caused by voltage controller. The output current of the inverters and bus voltages are illustrated in Fig. 3-26(a)-(b) and Fig. 3-26(c)-(d), respectively. Then, the harmonic instability phenomenon happens once the proportional coefficient (K_{pv}) of voltage controller is set into unstable region [34].

In contrast, the output current of the inverters and network voltages are stablized as shown in Fig. 3-27(a)-(b) and Fig. 3-27(c)-(d) once the proportional coefficients of the controllers are reduced [34].

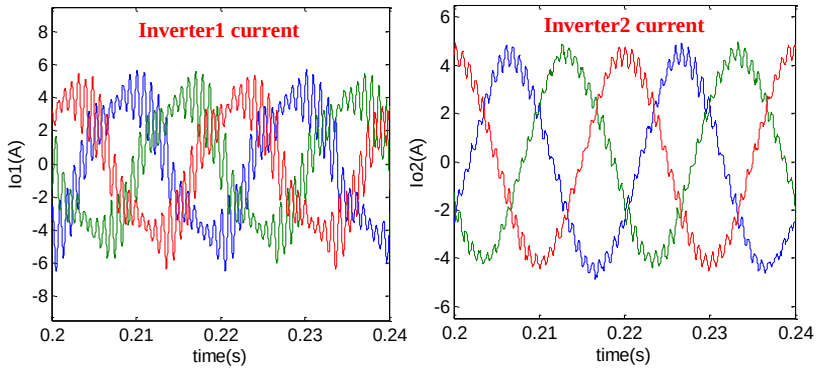

(a) (b)

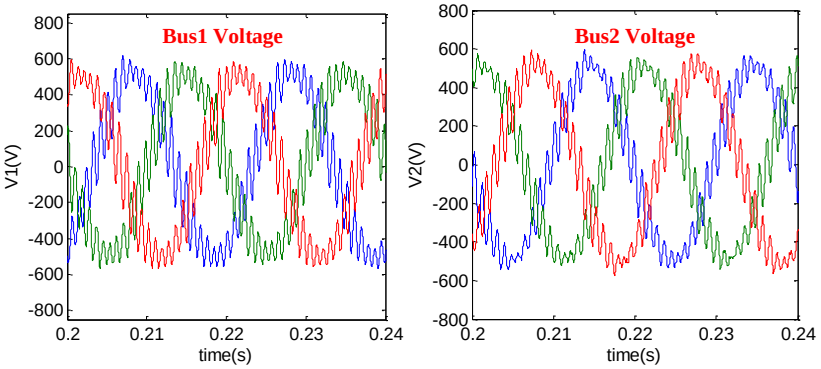

(c) (d)

Fig. 3-26. Experimental results of unstable case (K_{pv}=0.053, K_{pc}=8) [34]. *(a) Output current of DG1. (b) Output current of DG2. (c) Bus1 voltage. (d) Bus2 voltage.*

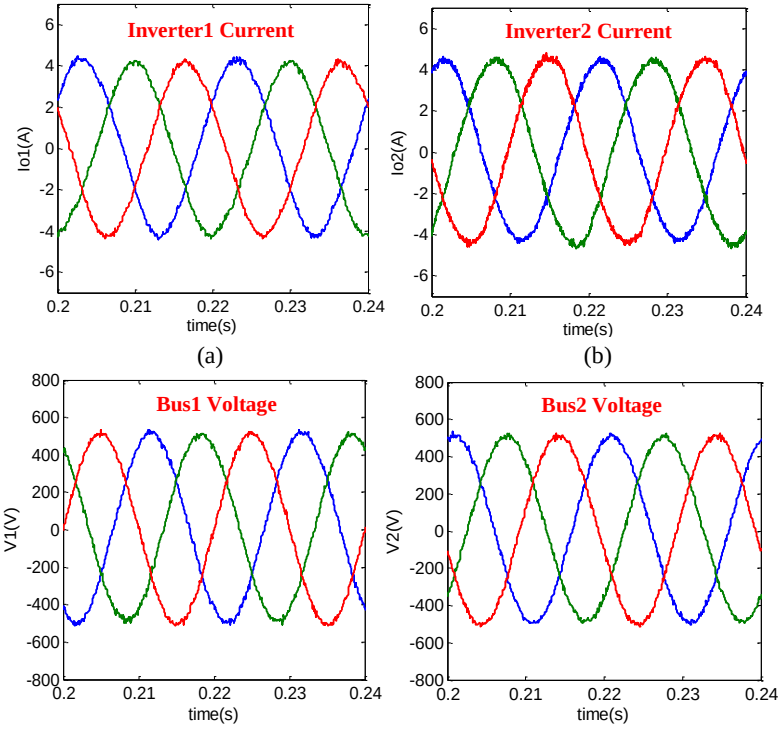

(a) (b)

(c) (d)

Fig. 3-27. Experimental results of stable case (K_{pv}=0.04, K_{pc}=8) [34]. *(a) Output current of DG1. (b) Output current of DG2. (c) Bus1 voltage. (d) Bus2 voltage.*

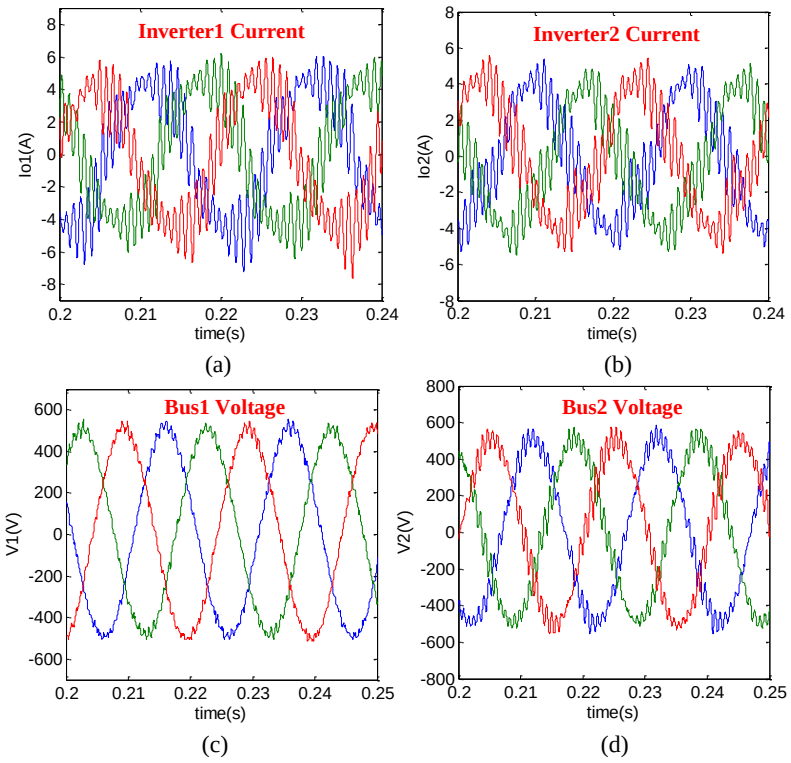

Fig. 3-28 Experimental results of unstable case (K_{pv}=0.04, K_{pc}=12) [34]. *(a) Output current of DG1. (b) Output current of DG2. (c) Bus1 voltage. (d) Bus2 voltage.*

Fig. 3-28 illustrates the experimental results of unstable case. The output current of DG units and bus voltages are depicted in Fig. 3-28(a)-(b) and Fig. 3-28(c)-(d), respectively. The high-frequency instability phenomenon still occurs once the proportional coefficients (K_{pc}) of the current controller are selected as 11 [34].

The simulation, experimental results as well as analysis results demonstrate that the high proportional coefficients of inner control loops cause the high-frequency instability phenomenon [34].

3.6 Conclusion

This chapter develops a CCM-based stability analysis method for inverter-interfaced power system, which is applicable in wide frequency range. The power system is first separated into various components, and the model of each component can be separately built. These component models are then combined to build a composite system model on the basis of interconnection relationship among components [34]. Finally, an eigenvalue-based method is presented to predict low-frequency

oscillation as well as harmonic-frequency oscillation, where the effect of voltage and current controller parameters on system stability is investigated [34]. The conclusion can be drawn that the parameters of inner controllers have essential effects on small-signal stability in different frequency range. Simulation and experimental results are provided to validate the proposed stability analysis approach.

CHAPTER 4. HARMONIC RESONANCE ASSESSMENT OF MULTIPLE PARALLELED GRID-CONNECTED INVERTERS SYSTEM

This chapter focuses on harmonic resonance issue of multiple paralleled grid-connected inverters. An eigenvalue-based impedance stability analytical method of paralleled grid-connected inverters is developed. The proposed method establishes the bridge between the state-space-based modeling and impedance-based stability criterion, which combines the advanced merits of the two methods [111]. Finally, the frequency scanning-based impedance analysis is presented to assess the resonance problem of grid-connected inverters system.

4.1. Small signal modeling of grid-connected inverters

This section first describes the circuit configuration of grid-connected inverters in this study. Then, the state-space model of grid-connected inverter with grid-current feedback and inverter-current feedback is built. Furthermore, the state-space model of paralleled grid-connected inverters is established.

4.1.1 Small signal modeling of single grid-connected inverter

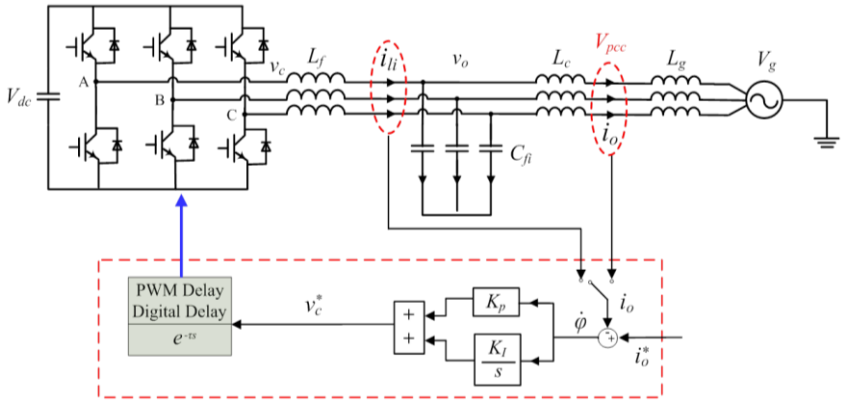

Fig. 4-1. The diagram of a three phase grid-connected inverter with grid-current feedback or converter-current feedback [111].

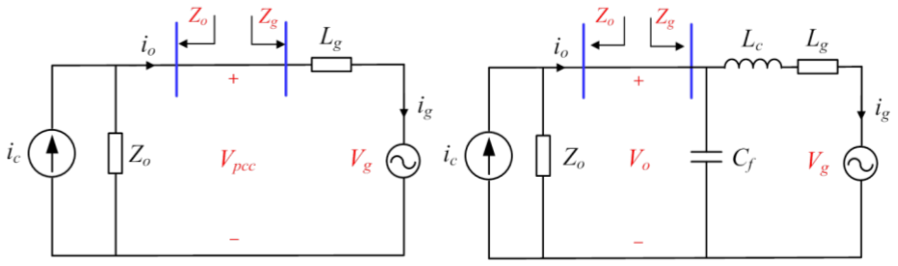

(a) (b)

Fig. 4-2. The equivalent circuit of impedance-based method [111]. *(a) Equivalent circuit of grid-connected inverter with grid-current feedback. (b) Equivalent circuit of grid-connected inverter with converter-current feedback.*

Fig. 4-1 shows the diagram of a grid-tied inverter with grid-current feedback or inverter-current feedback. Fig. 4-2 shows the equivalent impedance model of grid-connected inverter with grid-current feedback and converter-current feedback [111]. The PI-based current control loop is adopted to perform output current control. In this work, the inverter is modeled as linear time-invariant system, where the switching harmonics is disregarded since the switching frequency of inverter is well above the system fundamental frequency [78]. The state equation of current controller with grid-current feedback and converter-current feedback is given according to Fig. 4-1 as (4-1) [111].

$$\text{or} \quad \begin{aligned} \dot{\varphi}_i &= i_{oi}^* - i_{oi} \\ \dot{\varphi}_i &= i_{oi}^* - i_{li} \end{aligned} \tag{4-1}$$

The output equation of current controller is given as (4-2) [111].

$$\begin{aligned} v_c^* &= K_p(i_{oi}^* - i_{oi}) + K_I\varphi_i \\ v_c^* &= K_p(i_{oi}^* - i_{li}) + K_I\varphi_i \end{aligned} \tag{4-2}$$

As shown in Fig. 4-1, time delay is caused by sampling, computation and zero-order-hold effect of the pulse-width modulation [72]. The time delay of digital control system may be modeled as (4-3).

$$v_c = e^{-\tau \bullet s} v_c^* \tag{4-3}$$

where v_c^* and v_c are the demanded voltage and inverter output voltage, respectively. τ=1.5T_s is delay time resulting from digital computation delay (T_s) and the pulse width modulation (PWM) delay (0.5T_s), T_s is the sampling period of digital control system [78]. The delay plant (4-3) is converted into the state-space-model as (4-4) and (4-5) by Pade approximation [111].

$$\dot{x}_d = A_d x_d + B_d v_c^* \tag{4-4}$$

$$v_c = C_d x_d + D_d v_c^* \tag{4-5}$$

where A_d, B_d, C_d, D_d are parameter matrices. $A_d = \begin{bmatrix} 0 & 1 & 0 \\ 0 & 0 & 1 \\ -120/\tau^3 & -60/\tau^2 & -12/\tau \end{bmatrix}$, $B_d = [0 \quad 0 \quad 1]^T$, $C_d = [240/\tau^3 \quad 0 \quad 24/\tau]^T$, $D_d = [-1]^T$.

The differential equations of *LCL*-filter are represented according to Fig. 4-1 as (4-6)-(4-8) [111].

$$\dot{i}_L = -\frac{R_{f1}}{L_{f1}} i_L + \frac{1}{L_{f1}} v_c - \frac{1}{L_{f1}} v_o \tag{4-6}$$

$$\dot{v}_o = \frac{1}{C_{fi}} (i_L - i_o) \tag{4-7}$$

$$\dot{i}_o = -\frac{R_{c1}}{L_{c1}} i_o + \frac{1}{L_{c1}} v_o - \frac{1}{L_{c1}} V_{pcc} \tag{4-8}$$

Then, the state space model of single grid-tied inverters is formulated by combining (4-1), (4-4) and (4-6)-(4-8) as (4-9)-(4-10) [111].

$$\dot{x}_{invi} = A_{invi} x_{invi} + B_{invi} u_{invi} \tag{4-9}$$

$$y_{invi} = C_{invi} x_{invi} \tag{4-10}$$

where $x_{invi} = [i_L, v_o, i_o, \varphi, x_d]$, $u_{invi} = [i_{oi}^*, V_{pcc}]$, $y_{invi} = [i_{oi}]$. A_{invi}, B_{invi}, C_{invi} are parameter matrices.

For *i*th inverter, there are two input variables. If PCC voltage (V_{pcc}) is selected as input variable and output current is selected as output variable, the terminal characteristic can be represented by the transfer function of output voltage (V_{pcc}) to output current (i_{oi}) as (4-11) according to (4-9) and (4-10), the closed-loop output admittance and impedance are given as (4-11) and (4-12) [111].

$$Y_o = \frac{y_{invi}(s)}{u_{invi}(s)} = C_{invi}(sI - A_{invi})^{-1} B_{invi} \tag{4-11}$$

$$Z_o = -\frac{1}{Y_o} \tag{4-12}$$

4.1.2 Small signal modeling of paralleled grid-connected inverters

The aim of this section is to establish the small signal model of multiple paralleled grid-connected inverters and investigate the resonance phenomenon [111]. The configuration of multiple paralleled grid-connected inverters with *LCL* filter is shown in Fig. 4-3.

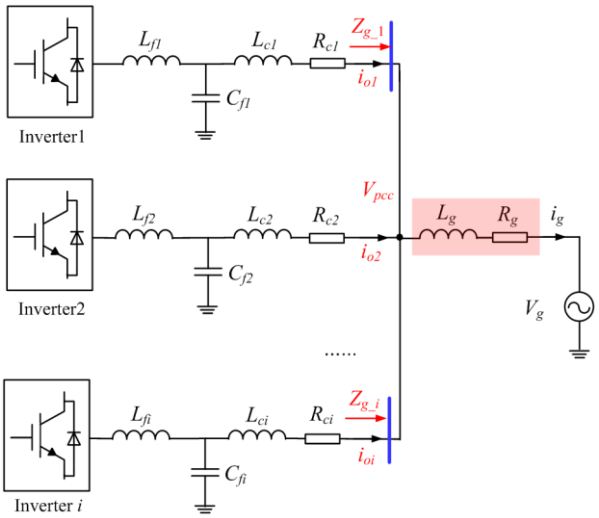

Fig. 4-3. The diagram of multiple paralleled grid-connected inverters with grid-current control [111].

The equivalent circuit of multiple paralleled grid-connected inverters is shown in Fig. 4-4. For *i*th inverter, the equivalent grid impedance (Z_{g_i}) looking from *i*th inverter is reshaped by the grid impedance paralleled with rest of inverters [111].

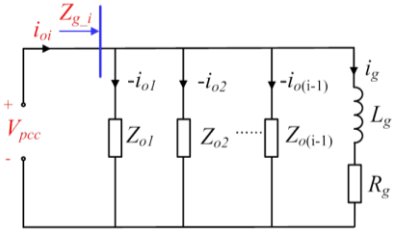

Fig. 4-4 The equivalent circuit of paralleled grid-connected inverters looking from ith inverter [111].

The grid-injected current is given as (4-13).

$$\dot{i}_g = -\frac{R_g}{L_g} i_g + \frac{1}{L_g} V_{pcc} \tag{4-13}$$

The overall state-space model is established by combining (4-9)-(4-10) and (4-13) as (4-14) [111].

$$\dot{x}_{sys} = A_{sys} x_{sys} + B_{sys} V_{pcc} \tag{4-14}$$

where $x_{sys}=\left[x_{invl},\cdots,x_{invi},i_g\right]^T$, $A_{sys}=diag(A_{invl},\cdots,A_{invi},-\frac{R_g}{L_g})$ is diagonal state matrix, $B_{sys}=\left[B_{invl},\cdots,B_{invi},\frac{1}{L_g}\right]^T$

To establish a simplified state-space model, a virtual resistor (R_n) is introduced to define PCC voltage as (4-15) [111].

$$V_{pcc}=R_n(i_{o1}+i_{o2}+\cdots+i_{oi}-i_g) \tag{4-15}$$

where the value of virtual resistor is selected as R_n=1000Ω. The PCC voltage may be rewritten by combining (4-10) and (4-15) as (4-16) [111].

$$V_{pcc}=Nx_{sys} \tag{4-16}$$

where $N=R_n\left[C_{invl},C_{inv2},\cdots,C_{invi},-1\right]$.

$$\dot{x}_{sys}=F_{sys}x_{sys} \tag{4-17}$$

where $F_{sys}=A_{sys}+B_{sys}N$ is state matrix of overall system. The eigenvalue trace of state matrix (F_{sys}) indicates the oscillation characteristic and damping characteristic of the overall system, which can be used to perform system stability assessment [111].

(2) Equivalent impedance derivation of paralleled inverters

It is well-known that the impedance-based analysis is able to perform stability assessment locally at the connection point of components. If state-space model of *i*th inverter is removed from the dynamic model (4-14), a new state equation of paralleled inverters may be formulated as (4-18) [111].

$$\dot{x}_{sys(i-1)}=A_{sys(i-1)}x_{sys(i-1)}+B_{sys(i-1)}V_{pcc} \tag{4-18}$$

Then, the output current of *i*th inverter is selected as system output, which is represented according to Fig. 4-3 as (4-19).

$$i_{oi}=-i_{o1}-i_{o2}-i_{o(i-1)}+i_g \tag{4-19}$$

Then, the equivalent grid impedance can be directly derived by proposed state-space model (4-18). The equivalent grid admittance and impedance looking from *i*th inverter may be derived as (4-20) and (4-21) [111].

$$Y_{g\_i}=\frac{i_{oi}(s)}{V_{pcc}(s)}=C_{invi}(sI-A_{invi})^{-1}B_{invi} \tag{4-20}$$

$$Z_{g\_i}=-\frac{1}{Y_{g\_i}} \tag{4-21}$$

The output impedance of inverter (4-12) and equivalent grid impedance (4-21) may be adopted to perform resonance assessment locally according to impedance stability criterion later.

4.2 Stability assessment of multiple paralleled inverters

4.2.1 Impedance-based stability criterion

As shown in Fig. 4-2, the grid-tied inverter may be modelled as a current source in paralleled with the output impedance [78]. According to the equivalent circuit model, the inverter output current can be represented as (4-22).

$$i_o = \left[i_c(s) - \frac{V_g(s)}{Z_o(s)} \right] \frac{1}{1 + Z_g(s)/Z_o(s)} \tag{4-22}$$

The grid-tied inverter would be stable if the ratio of the grid impedance to the inverter output impedance ($Z_g(s)/Z_o(s)$) satisfies the Nyquist criterion [113]. Assuming the grid impedance intersects with the inverter output impedance at frequency point f_i, the system would be unstable if the phase margin (PM) is less than zero. The phase margin at intersection point f_i could be defined [114]-[115] as (4-23).

$$PM(f_i) = 180^\circ - \left[\angle Z_g(f_i) - \angle Z_o(f_i) \right] \tag{4-23}$$

The criterion can be applied to the following cases to assess system stability characteristic. Fig. 4-5 shows the frequency response of closed-loop output impedance and grid impedance. The stability can be investigated according to phase characteristic at intersect point of output impedance and grid impedance [78]. It can be seen from Fig. 4-5 that the intersection point will move upward as the increase of grid impedance, so that the phase margin is reduced [111].

It can be observed that the intersection points will move upward and the phase margin at intersection points will be reduced as the increase of grid impedance. Once the phase difference is higher than 180^o, which means the negative phase margin will happen, the system would become unstable [111].

The frequency response of converter-current control is shown in Fig. 4-6. With the decrease of grid impedance, the intersection point will move backward, and the system becomes destabilized in this region within which the phase margin of intersection point is negative [111].

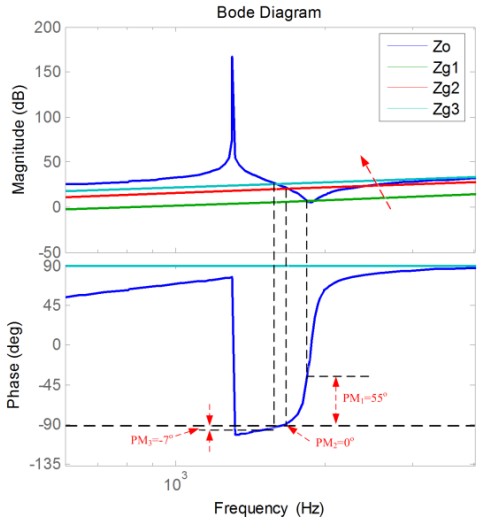

Fig. 4-5 The frequency response of closed-loop output impedance and grid impedance for grid-current feedback. (L_f=3mH, C_f= 5uF, L_c=1.6mH, $Z_{g1}/Z_{g2}/Z_{g3}$=0.2mH, 1mH, 2.5mH) [111].

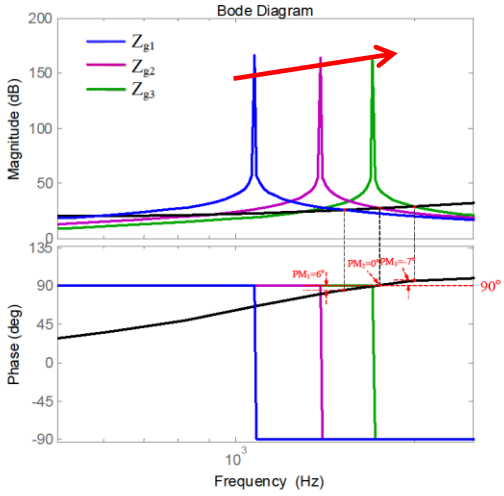

Fig. 4-6 The frequency response of closed-loop output impedance and grid impedance for converter-current control. (L_f=3mH, C_f= 9uF, L_c=2mH, $Z_{g1}/Z_{g2}/Z_{g3}$=1.5mH, 0.9mH, 0.4mH) [111].

Fig. 4-6 shows the frequency response of closed-loop output impedance and grid impedance for converter-current control [111]. It can be seen that the intersection point moves toward right as the decrease of grid impedance, and then the phase margin is reduced.

4.2.2 The Proposed Resonance Assessment Method

Different from stability issue of single inverter, the multiple paralleled grid-connected inverters pose more complex resonance characteristic [111]. Fig. 4-7 shows the frequency response of the equivalent grid impedance with multiple paralleled inverters, which explains how the multiple inverters reshape the grid impedance. It can be observed that the phase difference at intersection points of output impedance and equivalent grid impedance is magnified as the increase of inverter number [111]. The system would become unstable once the phase margin is negative.

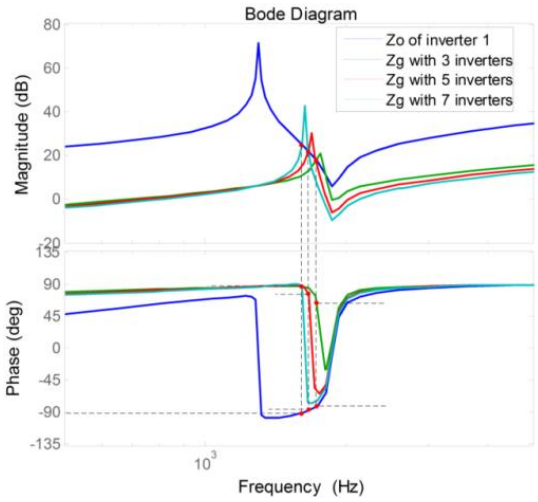

Fig. 4-7. The stability assessment for paralleled grid-connected inverters with grid-current feedback. (L_g=0.5mH) [111].

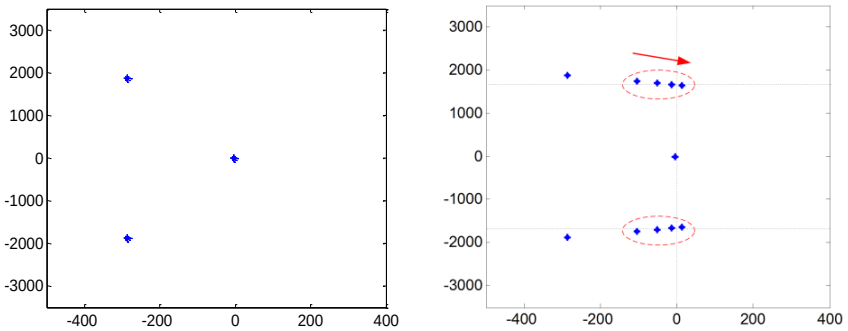

Fig. 4-8. The eigenvalue trace of grid-connected inverters. (a) The eigenvalue trace of individual grid-connected inverter. (b) The eigenvalue trace as the increase of paralleled inverter number from 2 to 5 [111].

To investigate comprehensive oscillation and damping characteristic, the eigenvalue analysis is performed according to the proposed state-space model (4-17). Fig. 4-8(a) depicts the eigenvalue trace of individual inverter, which are located in left-half plane and indicates that individual inverter is able to operate stably. Assuming all the inverters have equipped identical *LCL* filters, the Fig. 4-8(b) shows the eigenvalue trace of multiple paralleled inverters system as the increase of inverter number, where the paralleled inverters are coupled due to grid impedance [111]. It can be seen that a complex pole pair with oscillation frequency 1.8 kHz occurs, which indicates the coupling phenomenon among paralleled inverters. With the increase of inverter number (from 2 to 5), the coupling conjugate pair moves toward right-half complex plane (unstable region). Hence, the impedance stability analysis from Fig. 4-7 and the eigenvalue-based stability analysis from Fig. 4-8 obtain the same results.

To explain the effects of multiple inverters with different *LCL* filters on equivalent grid impedance, the frequency response of paralleled grid-connected inverters with different *LC* filter is given in Fig. 4-9, where the parameters of case I and case II are listed in Table 4-1. It can be observed that the paralleled inverters with different *LC* resonance frequency reshape the equivalent grid impedance, which shows that the case I has a positive phase margin (stable case), while the case II has a negative phase margin (unstable). Thus, the different *LC* filters give different contributions on grid impedance shaping and system resonance behavior [111]. The phase difference at intersection points of output impedance and equivalent grid impedance can be changed as the variation of *LC* filters.

TABLE 4-1
LCL FILTER PARAMETERS [111].

	Case I	**Case II**
Inverter 1	C_{f1}=5uF, L_{c1}=2mH	C_{f1}=5uF, L_{c1}=2mH
Inverter 2	C_{f2}=5uF, L_{c2}=2mH	C_{f2}=5uF, L_{c2}=2mH
Inverter 3	C_{f3}=5uF, L_{c3}=2mH	C_{f3}=9uF, L_{c3}=0.4mH
Inverter 4	C_{f4}=5uF, L_{c4}=2mH	C_{f4}=9uF, L_{c4}=0.4mH

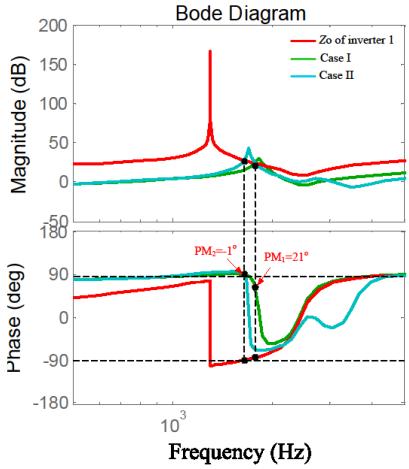

Fig. 4-9. The frequency response of paralleled grid-connected inverters (Case I and Case II) [111].

Similarly, Fig. 4-10 shows that the eigenvalue trace of single inverter and paralleled inverters, where the Fig. 4-10(a) depicts the terminal oscillation characteristic of inverter 1 and inverter 2, and the Fig. 4-10(b) shows the terminal characteristic of inverter 3 and inverter 4 with different *LC* filter. Fig. 4-10(c) shows the eigenvalue trace of paralleled inverters system. It can be seen that the paralleled inverters system produces a conjugate pole pair that indicates the coupling effect and dominates system dynamics [111]. The impedance analysis from Fig. 4-9 and eigenvalue analysis from Fig. 4-10 obtain the identical results.

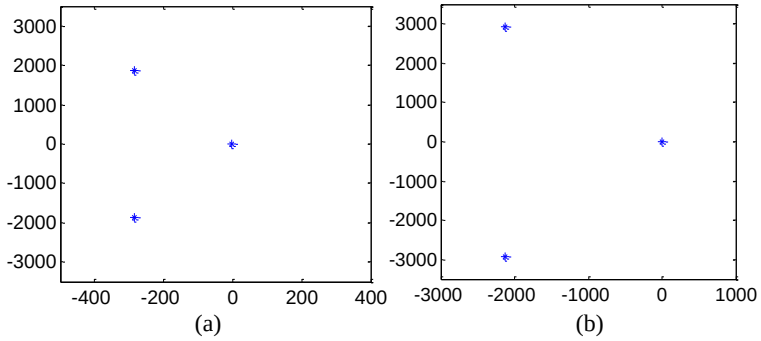

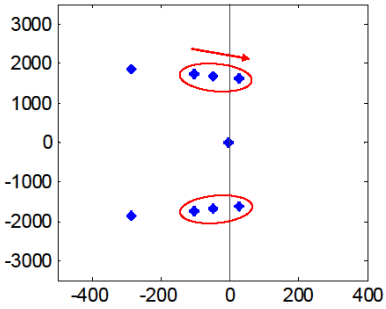

(c)

Fig. 4-10. The high-frequency oscillation mode ($\lambda_{1\text{-}2}$) of grid-connected inverters. (a) The eigenvalues of inverter 1 and inverter 2. (b) The eigenvalues of inverter 3 and inverter 4. (c) The eigenvalues of paralleled grid-connected inverter from 2 inverters to 4 inverters [111].

As a superior feature of state-space-method, the participation analysis may be adopted to identify origins of oscillation modes. The aim of it is to establish the relationship between state variables and oscillation modes, and identify the origin of oscillation phenomenon [111]. The participation factor p_{ki} of the k th state variable and i th eigenvalue is defined as [72]

$$p_{ki} = \frac{\partial \lambda_i}{\partial a_{kj}} = u_{ik} v_{ji} \tag{4-24}$$

where the sensitivity of eigenvalue λ_i to the element α_{kj} of the state matrix is equal to the product of the left eigenvector element u_{ik} and the right eigenvector element v_{ji} [72].

The participation analysis result for oscillation modes of paralleled grid-connected inverters with identical filter can be seen in Table. 4-2, where only the magnitudes of the participation factors are shown due to the angles do not provide any useful information [111]. It can be observed that the harmonic oscillation modes $\lambda_{1\text{-}2}$ are highly sensitive to the states of current controller and time delay of the inverter, which induces the harmonic-frequency instability [111]. The participation analysis results for paralleled inverters with different filters are shown in Table 4-3.

TABLE 4-2

PARTICIPATION ANALYSIS FOR INVERTER WITH SAME FILTER (CASE I) [111]

$\lambda_{1\text{-}2}$ (coupled oscillation mode)			
State	Participation	State	Participation
i_{l1}/i_{l2}	0.06/0.06	i_{l3}/i_{l4}	0.06/0.06
x_{p1}/x_{p2}	0.04/0.04	x_{p3}/x_{p4}	0.04/0.04
v_{o1}/v_{o2}	0.13/0.13	v_{o3}/v_{o4}	0.13/0.13
i_{o1}/i_{o2}	0.03/0.03	i_{o3}/i_{o4}	0.03/0.03
i_g	0.08		

TABLE 4-3
PARTICIPATION ANALYSIS FOR INVERTER WITH DIFFERENT FILTER (CASE II) [111]

$\lambda_{1\text{-}2}$ (coupled oscillation mode)			
State	Participation	State	Participation
i_{l1}/i_{l2}	0.03/0.03	i_{l3}/i_{l4}	0.04/0.04
x_{p1}/x_{p2}	0.01/0.01	x_{p3}/x_{p4}	0.09/0.09
v_{o1}/v_{o2}	0.05/0.05	v_{o3}/v_{o4}	0.2/0.2
i_{o1}/i_{o2}	0.005/0.005	i_{o3}/i_{o4}	0.07/0.07
i_g	0.11		

Fig. 4-11 shows that the frequency response of inverter output impedance for converter-current feedback and equivalent grid impedance shaped by multiple paralleled inverters [111]. As the increase of inverter number, the intersection point moves leftward, which indicates phase margin is increased. Fig. 4-12 shows that the eigenvalue traces of grid-connected inverters with converter-current feedback, where the eigenvalue traces of individual inverter and paralleled inverters are shown in Fig.4-12(a)-(b) [111]. It can be observed that the paralleled system produces a conjugate pole pair that indicates the coupling effect of paralleled inverters. The coupling pole pair moves toward left-half plane (stable region) as the increase of inverter number, which slightly dominates system dynamics [111].

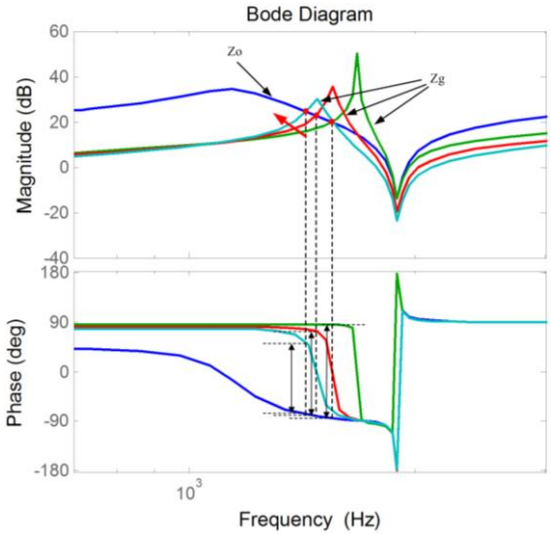

Fig. 4-11. The frequency response of equivalent grid impedance of paralleled grid-connected inverters. (L_f=3mH, C_f=10uF, L_c=1mH, Z_g=0.5mH) [111].

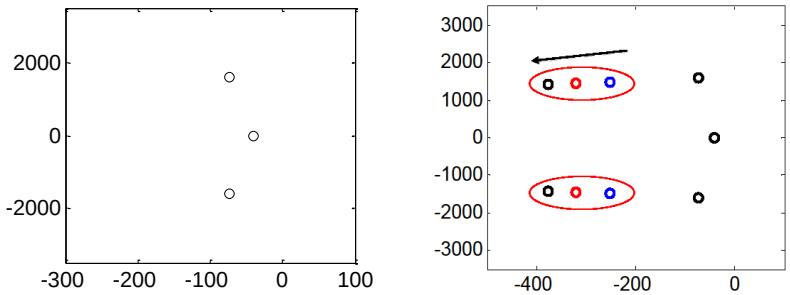

(a) (b)

Fig. 4-12. The high-frequency oscillation mode of system. (a)The eigenvalues of individual inverter (A_{invi}). (b)The eigenvalues trace of paralleled inverters as the increase of inverter number from 2 to 4 [111].

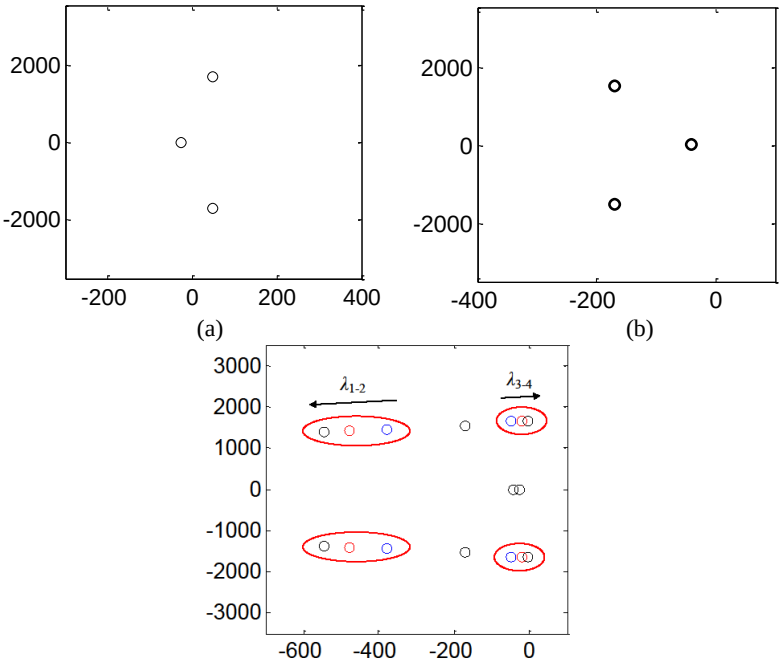

(a) (b) (c)

Fig. 4-13. The high-frequency oscillation mode of system. (a) The eigenvalue trace of inverter 1 (A_{inv1}). (b) The eigenvalues of other inverters. (c) The eigenvalues trace of paralleled inverters as the increase of inverter number from 2 to 4 [111].

Unlike the grid current-controlled inverters system, the converter current-controlled paralleled system is slightly affected by equivalent grid impedance, which mainly depends on the certain inverters with underdamping characteristic [111]. If the *LCL* filter parameter is changed due to aging or external disturbances in real plant, the underdamping behavior of inverters will occur and cause system unstable. It can be

observed from Fig. 4-13 that the new underdamping pole pair ($\lambda_{3\text{-}4}$) occurs, which dominates paralleled system dynamic performance.

4.2.3 The proposed frequency-scanning-based impedance analysis for grid-connected inverter

A. The procedure of frequency-scanning method

The objective of frequency scanning analysis is to compute the equivalent impedance looked from the grid into inverter, and the equivalent grid impedance looked from the grid into inverter. The application of current injection techniques for the determining the harmonic impedance is shown in Fig. 4-14. In the current injection method, the small current disturbance is injected into grid-connected inverter system in particular frequency range. The measurements may be performed at the same point as the injection point or at a different point [112].

The grid impedance looked from the inverter into the network (Z_g), and output impedance of inverter looked from the network (Z_o) can be computed by measuring the voltage and current at the measuring point, the impedance seen from the point at different frequencies can be estimated based on Fourier analysis [112]. The equivalent impedance of the inverter and grid impedance are calculated as (4-25) and (4-26).

$$Z_o = \frac{F\left[V_{pcc\_s} + V_{pcc\_dis}\right]}{F\left[-i_{oi\_s} - i_{oi\_dis}\right]} \tag{4-25}$$

$$Z_g = \frac{F\left[V_{pcc\_s} + V_{pcc\_dis}\right]}{F\left[i_{g\_s} + i_{g\_dis}\right]} \tag{4-26}$$

where F denotes the Fourier transformation, V_{pcc_s} denotes the PCC (Point of common) voltage in fundamental frequency, V_{pcc_dis} denotes the voltage response excited by disturbance current in harmonic frequency, i_{oi_s} and i_{oi_dis} are output current of inverter in fundamental frequency and in harmonic frequency, i_{g_s} and i_{g_dis} are grid-injected current in fundamental frequency and in harmonic frequency.

B. Frequency scanning for grid-connected inverter with grid-current feedback

Fig. 4-14 shows the principle of frequency-scanning method for computing the equivalent impedance of grid-connected inverter system, where the high-frequency current disturbances (700Hz-2200Hz) are injected into system [112]. Fig. 4-14 (a) shows the diagram of current injection for single grid-connected inverter with grid-current feedback.

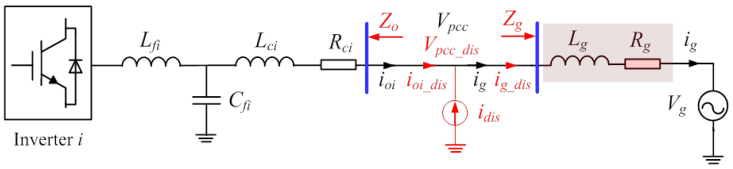

(a)

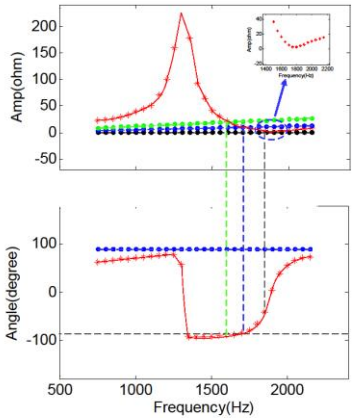

(b)

Fig. 4-14. Frequency scanning for single grid-connected inverter with grid-current feedback. (a) The diagram of current injection. (b) Frequency-scanning-based stability analysis ($Z_{g1}/Z_{g2}/Z_{g3}$=0.1mH, 1mH, 2mH) [112].

The frequency-scanning result is shown in Fig. 4-14(b). The intersection point of output impedance and grid impedance will move upward as the increase of grid impedance, and the system would be destabilized in this region within which the phase margin of intersection point is negative [112]. It can be seen that the impedance analysis obtained from frequency scanning agrees with the stability analysis shown in Fig. 4-5.

C. Frequency scanning for grid-connected inverter with converter-current feedback

Fig. 4-15 shows the frequency-scanning method for grid-connected inverter with converter-current feedback, where the current disturbances (700Hz-2200Hz) are injected into system [112]. The diagram of current injection for single grid-connected inverter with converter-current feedback is shown in Fig. 4-15(a). And the frequency response results are shown in Fig. 4-15(b). It can be seen that the impedance performance obtained from frequency scanning agrees with the stability analysis from small signal model as shown in Fig. 4-6.

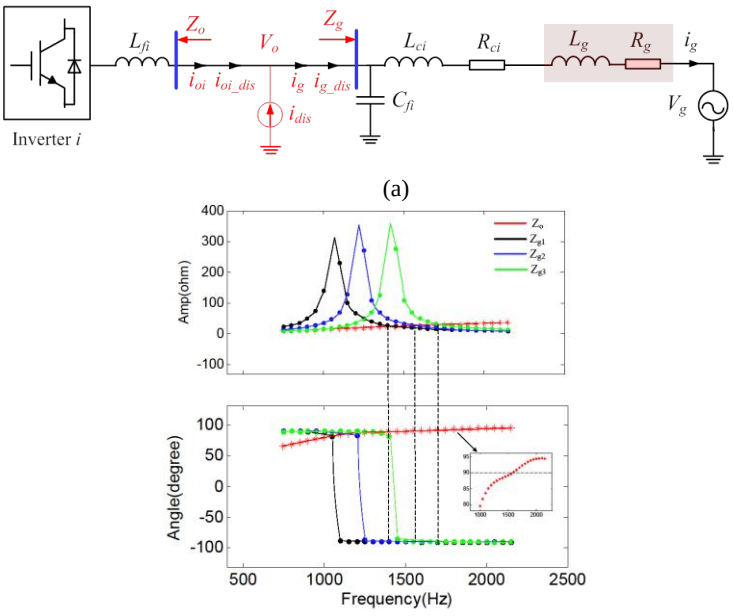

Fig. 4-15. Frequency scanning-based impedance analysis for the converter-current feedback (L_f=3mH, C_f=9uF, L_c=2mH, Z_{g1}/Z_{g2}/ Z_{g3}=1.5mH, 0.9mH, 0.4mH) [112].

D. Frequency-scanning-based impedance analysis for paralleled grid-connected inverter

Fig. 4-16 shows the frequency-scanning-based impedance analysis of multiple paralleled grid-connected inverters with grid-current feedback. The diagram of current disturbance injection is shown in Fig. 4-16(a). Different from single grid-connected inverter, the equivalent grid impedance of paralleled inverters is reshaped. For the *i*th inverter, the equivalent grid impedance (Z_{g_i}) is reshaped by the grid impedance (Z_g) paralleled with the rest of inverters [112]. The frequency response of inverter impedance (Z_o), grid impedance (Z_g) and equivalent grid impedance (Z_{g_i}) is shown in Fig. 4-16(b). Z_{g1} and Z_{g2} are equivalent grid impedance with 1 inverter and two inverters. It can be seen that the phase margin at intersection points is reduced as the increase of inverter number.

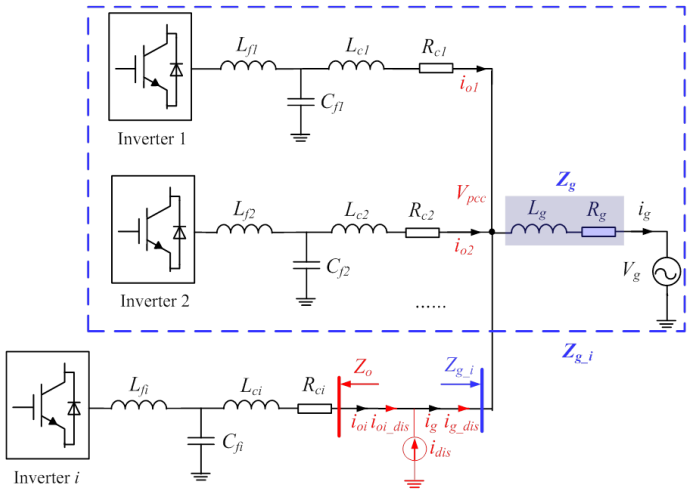

(a)

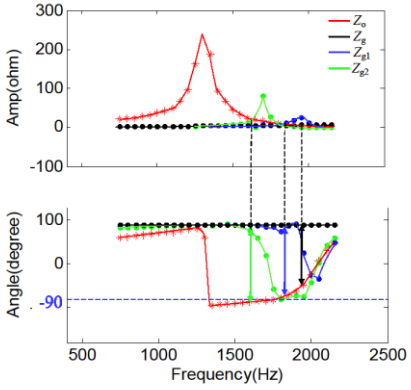

(b)

Fig. 4-16. Frequency scanning results for multiple paralleled grid-connected inverters with grid-current feedback (Z_o, Z_{g_i}). (a) The diagram of current injection. (b) Frequency-scanning-based stability analysis (L_f=3mH, C_f=5uF, L_c=2mH, Z_g=0.6mH) [112].

4.3 Simulation Verification

To validate the frequency scanning-based impedance stability analysis, the simulation and experimental verification are performed in this section.

A. Stability assessment of single grid-connected inverter

Fig. 4-17 depicts the simulation results of single grid-connected inverter with grid-current feedback in the unstable case. The output current of inverter and PCC voltage are shown in Fig. 4-17(a) and Fig. 4-17(b). Fig. 4-18 shows the simulation

results of single grid-connected inverter with grid-current feedback in unstable case. It can be seen that the resonance phenomenon happens when the grid impedance (Z_g) is 1mH. On the contrary, the output current of inverter is stabilized as shown in Fig.4-18 if the grid impedance is decreased to 0.4mH, then the intersection point of inverter output impedance and grid impedance is within stable region.

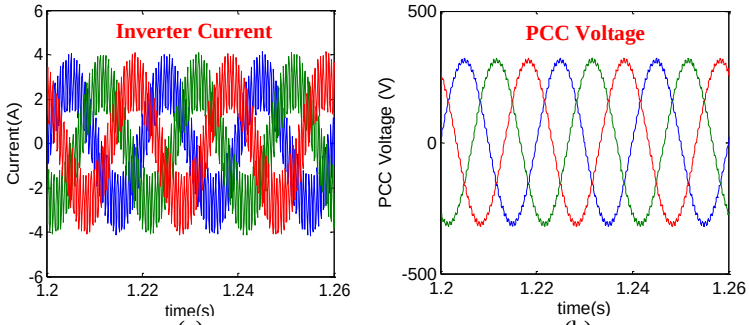

(a) (b)

Fig. 4-17. The unstable case of single grid-connected inverter with grid-current feedback (L_f=3mH, C_f=5uF, L_c=2mH, L_g=1mH) [112]. *(a) The output current of inverter. (b) PCC voltage.*

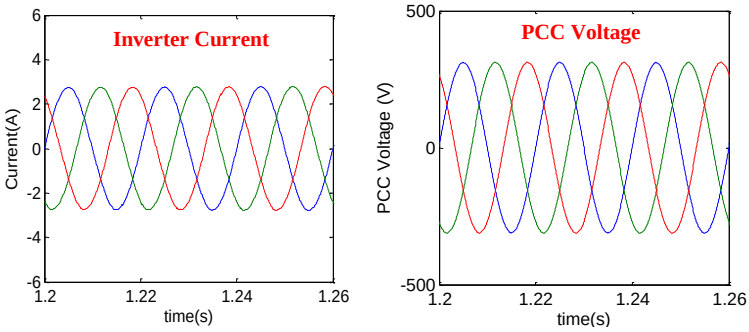

(a) (b)

Fig. 4-18. The stable case of single grid-connected inverter with grid-current feedback (L_f=3mH, C_f=5uF, L_c=2mH, L_g=0.4mH) [112]. *(a) The output current of inverter. (b) PCC voltage.*

B. Stability assessment for single grid-connected inverter with converter-current feedback

Fig. 4-19 shows the simulation results in unstable case for single grid-connected inverter with converter-current feedback. The output current and PCC voltage are shown in Fig. 4-19(a) and Fig. 4-19(b). As the decrease of grid impedance, the resonance phenomenon will happen (L_g=1.6mH). On the contrary, the output current of inverter and PCC voltage are stabilized as shown in Fig. 4-20 when the grid impedance is increased (L_g=2mH) [112]. The simulation results match the stability analysis shown in Fig. 4-8(a).

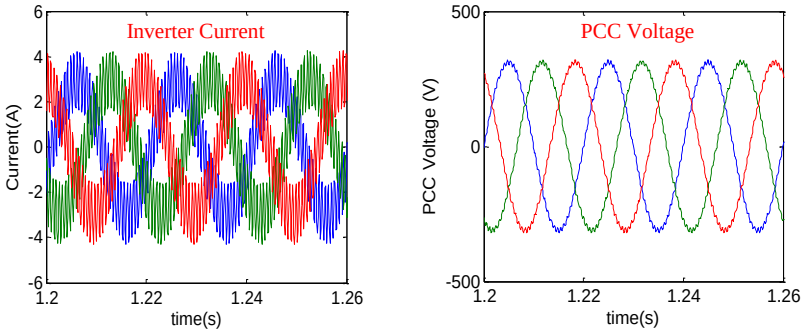

(a) (b)

Fig. 4-19. The unstable case of grid-connected inverter with converter-current feedback (L_f=3mH, C_f=9uF, L_c=1mH L_g=1.6mH) [112]. *(a) The output current of inverter. (b) PCC voltage.*

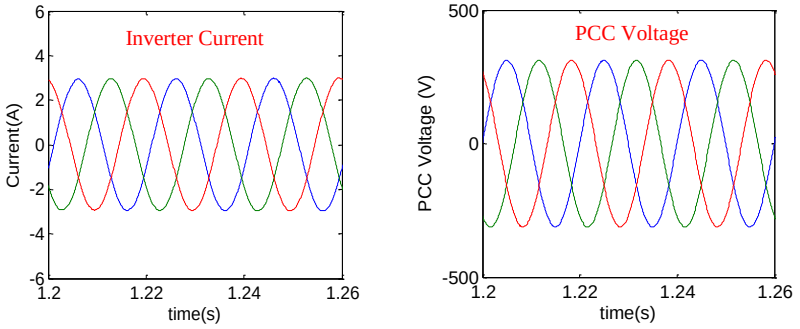

(a) (b)

Fig. 4-20. The stable case of grid-connected inverter with converter-current feedback (L_f=3mH, C_f=9uF, L_c=1mH, L_g=2mH) [112]. *(a) The output current of inverter. (b) PCC voltage.*

C. Stability assessment for paralleled grid-connected inverters with grid-current feedback

The simulation results of paralleled grid-connected inverters with grid-current feedback (Case I) are shown in Fig. 4-21. The inverter 1 and inverter 2 are paralleled stably. Once the inverter 3 is activated and paralleled into system at 0.25s, the resonance behavior in output currents and voltages is observed [112]. When the inverter 4 is activated and connected to grid, the resonance behavior is aggregated and the whole system becomes unstable. The simulation results agree with the analytical results from impedance analysis and eigenvalue analysis as shown in Fig. 4-7 - Fig. 4-8.

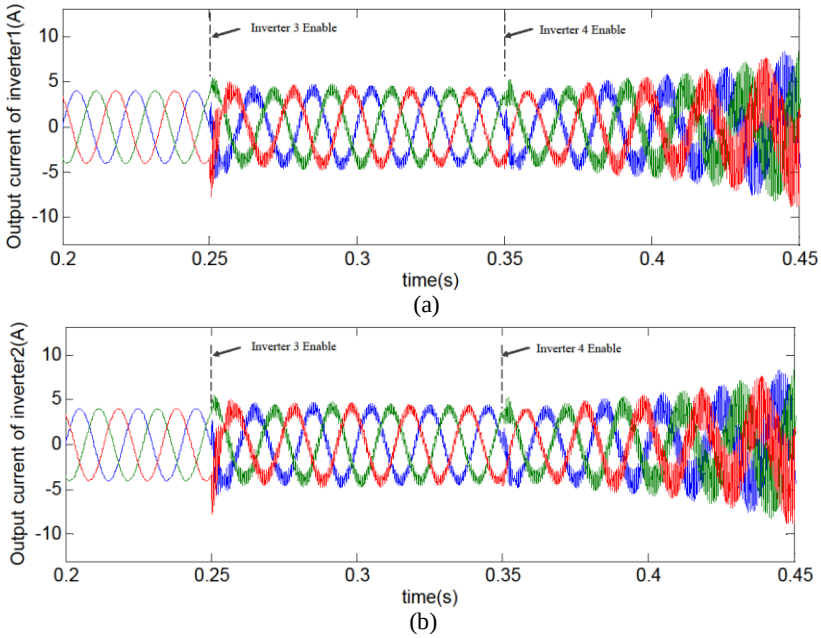

Fig. 4-21. The simulation results of paralleled grid-connected inverter with grid-current feedback. (a) The output current of inverter 1. (b) The output current of inverter 2.

D. Stability assessment of paralleled inverters with different *LCL* filters

Fig. 4-22 shows the simulation results of paralleled inverters with identical *LCL* filters. The overall grid-connected inverter system is stable even if the inverter3 and inverter4 are paralleled at 0.25s, whereas different *LCL* resonance characteristic will change system stability region [112].

Fig. 4-23 shows the simulation results of paralleled inverters with different *LCL* filters. The inverter1 and inverter 2 are stably paralleled. Once the inverter 3 and inverter 4 is paralleled at 0.25s, the system would become unstable that agrees with the stability analysis results from Fig. 4-9- Fig. 4-10.

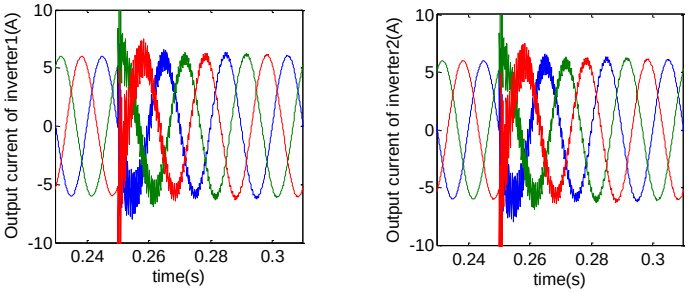

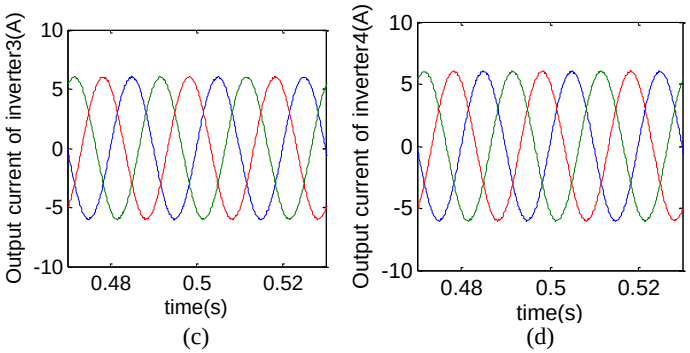

Fig. 4-22. The stable case of paralleled grid-connected inverters with same LCL filters (Case II) [112]. *(a) The output current of inverter 1. (b) The output current of inverter 2. (c) The output current of inverter 3. (d) The output current of inverter 4.*

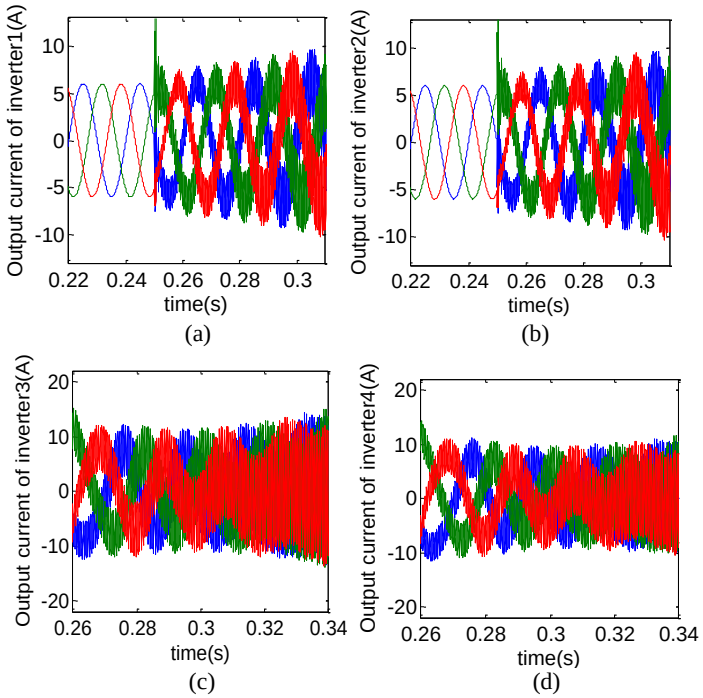

Fig. 4-23. The unstable case of paralleled grid-connected inverters with LCL filters (Case III) [112]. *(a) The output current of inverter 1. (b) The output current of inverter 2. (c) The output current of inverter 3. (d) The output current of inverter 4.*

E. Stability assessment for paralleled grid-connected inverters with converter-current feedback

Fig. 4-24 shows the stable case of paralleled grid-connected inverters with converter-current feedback. In this case, the inverter1 and inverter2 operate stably,

the paralleled system still keeps stable after the inverter 3 and inverter 4 is connected into system. The simulation results agree with the resonance analysis from Fig. 4-11- Fig. 4-12.

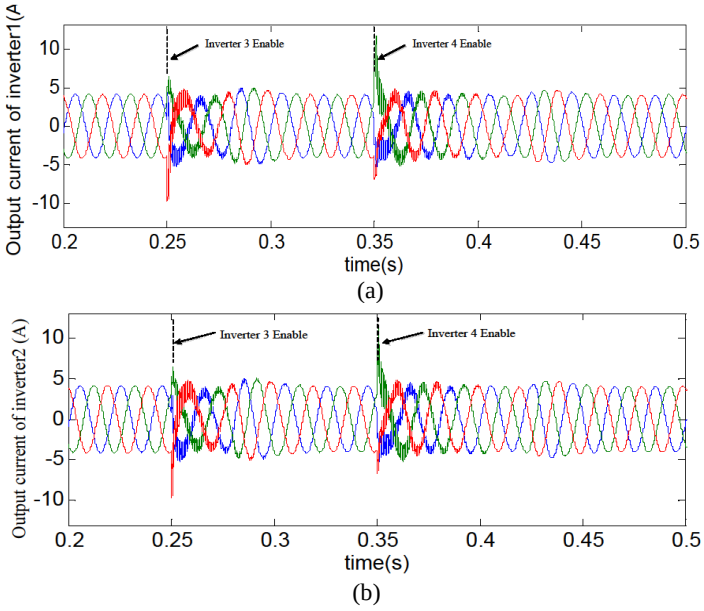

Fig. 4-24. The stable case of paralleled grid-connected inverters with converter-current feedback [112]. *(a) The output current of inverter 1. (b) The output voltage of inverter 2. (c) The output voltage of inverter 3.*

Fig. 4-25 shows the unstable case of paralleled system with converter-current feedback. At the beginning, the paralleled inverters system operates stably. Once the inverter 4 gives rise to oscillation behavior due to self-underdamping at 0.2s, the oscillation phenomenon will happen in current response. Then, the resonance behavior is propagated to the whole paralleled system and finally causes system instability [112]. The simulation results agree with the stability analysis from Fig. 4-13.

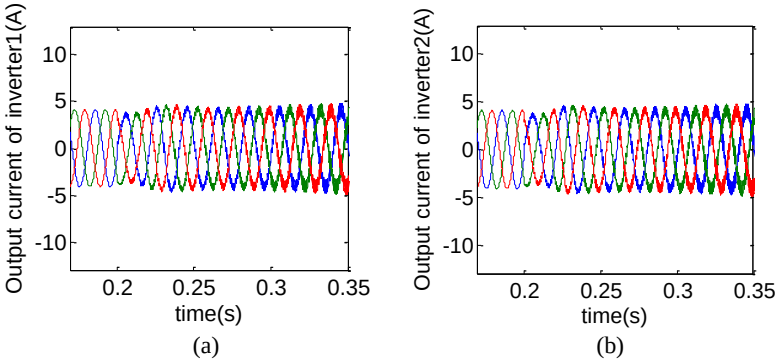

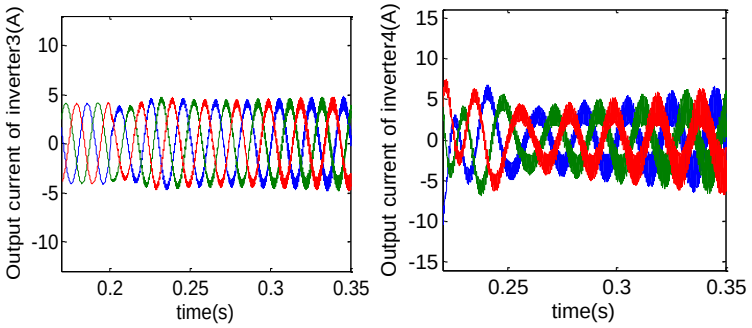

(c) (d)

Fig. 4-25. The unstable case of paralleled grid-connected inverters with converter-current feedback [112]. *(a) The output current of inverter 1. (b) The output current of inverter 2. (c) The output current of inverter 3. (d) The output current of inverter 4.*

4.4 Experimental verification

Fig. 4-26 shows the circuit configuration and experimental setup of the paralleled grid-connected inverters in this work, which is composed of three Danfoss converters (5kW), DC power source (750V), isolated transformers and *LCL* filters. The whole platform is controlled by dSPACE 1006 with a sampling period (T_d) of 100μs. The grid-side filter inductance includes line inductance (L_{c1}) and leakage inductance of the isolation transformer (L_{TF1}).

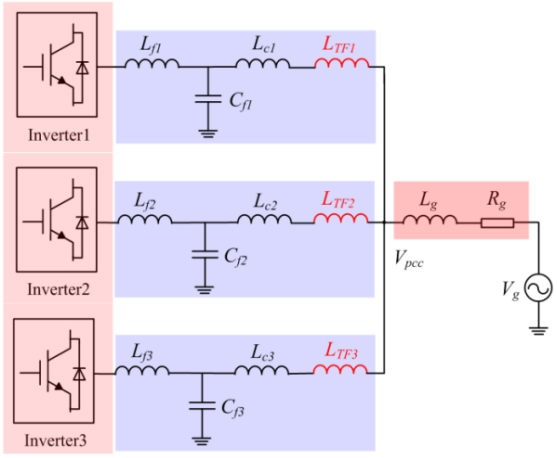

(a)

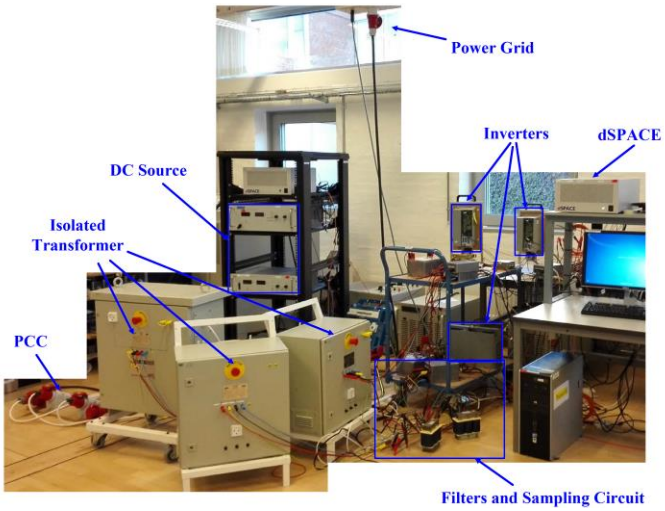

(b)

Fig. 4-26. The experimental setup. (a) System configuration. (b) Photo of experimental setup [112].

A. Stability assessment of single grid-connected inverter

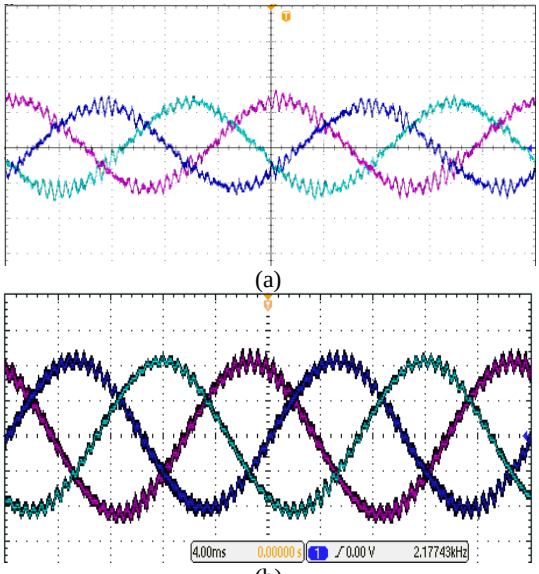

(a)

(b)

Fig. 4-27. The experimental results in unstable case for single grid-connected inverter with grid-current feedback (L_f=3mH, C_f=5uF, L_c=2mH, L_g=0.8mH) [112]. *(a) The output current of inverter. (b) PCC voltage.*

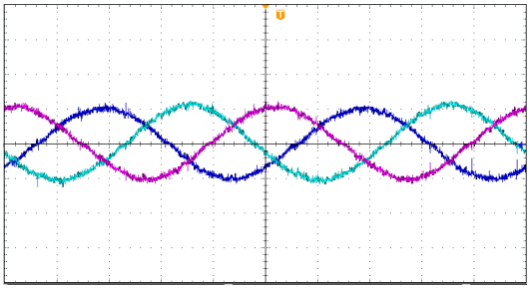

(a)

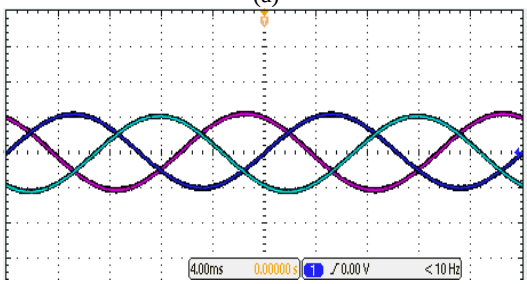

(b)

Fig. 4-28. The experimental results in stable case for single grid-connected inverter (L_f=3mH, C_f=5uF, L_c=2mH, L_g=0.3mH) [112]. *(a) The output current of inverter. (b) PCC voltage.*

Fig. 4-27 shows the experimental results of unstable case for single grid-connected inverter with grid-current feedback, and Fig. 4-28 shows the experimental results of stable case for single grid-connected inverter.

B. Stability assessment of multiple paralleled inverters system

The experimental results of paralleled grid-connected inverters with grid-current feedback control in weak grid (1mH) are shown in Fig. 4-29. Fig. 4-29(a) shows the inverter1 can operate stably. Once the inverter 2 is activated and paralleled into grid, the resonance phenomenon in output currents is observed as shown in Fig. 4-29(b). When the inverter 3 is connected into grid, the resonance outputs are aggravated as shown in Fig. 4-29(c). Hence, the resonance behavior of inverters is induced due to the increase of inverter number. The experimental results verify the analytical results from stability analysis from Fig. 4-7- Fig.4-8.

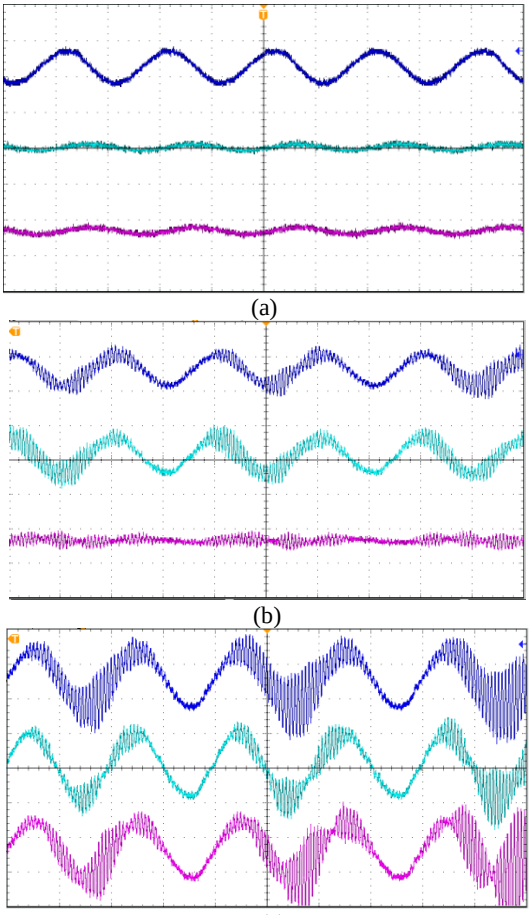

(a)

(b)

(c)

Fig. 4-29. The resonance phenomenon of paralleled grid-connected inverters. (a) The A phase output current of single inverter. (b) The A phase output current of two paralleled inverters. (c) The A phase output current of three paralleled inverters. [112]

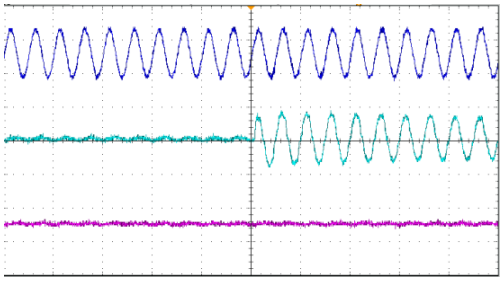

(a)

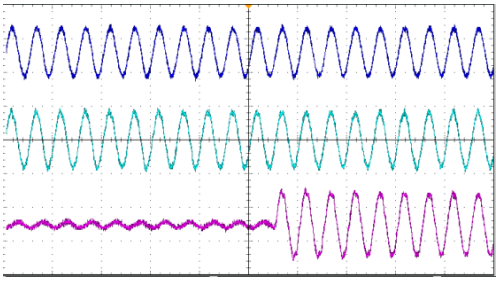

(b)

Fig. 4-30. The experimental results of paralleled inverters with same LC filters. ($L_{f1}/L_{f2}/L_{f3}$=3mH/3mH/3mH, $C_{f1}/C_{f2}/C_{f3}$=5uF/5uF/5uF, $L_{c1}/L_{c2}/L_{c3}$=2.6mH/2.6mH/2.6mH) [112]. *(a) The A-phase output currents (5A/div) of inverters when inverter2 is connected to grid. (b) The A-phase output currents (5A/div) of inverters when inverter 3 is connected to grid.*

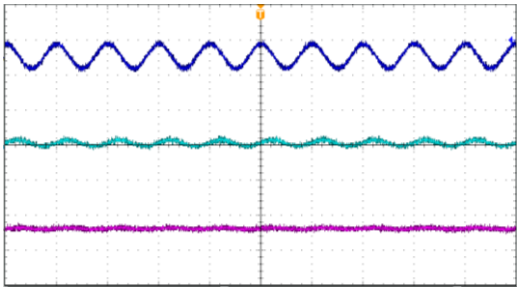

(a)

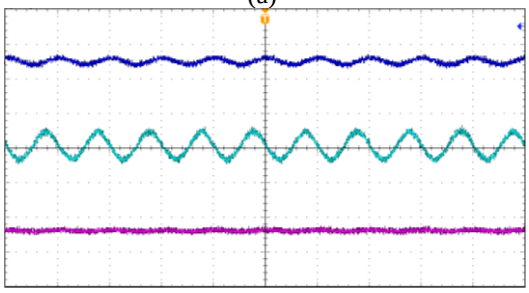

(b)

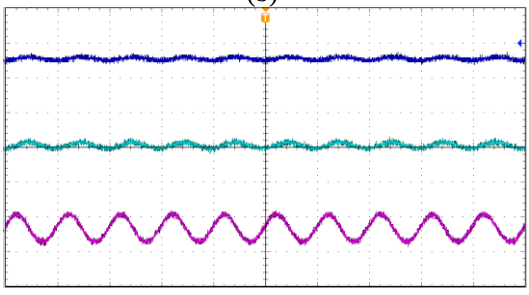

(c)

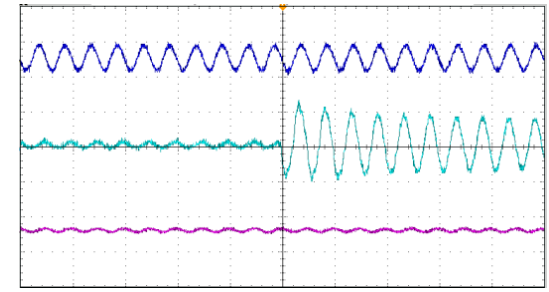

(d)

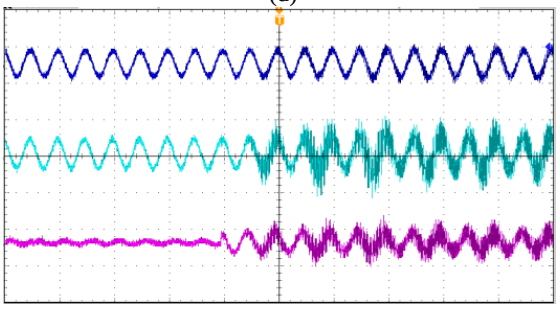

(e)

Fig. 4-31. The experimental results of paralleled inverters with different LCL filters. ($L_{f1}/L_{f2}/L_{f3}$=3mH/3mH/3mH, $C_{f1}/C_{f2}/C_{f3}$=5uF/10uF/10uF, $L_{c1}/L_{c2}/L_{c3}$=0.3mH/0.3mH/0.3mH) [112]. *(a) The A-phase current of inverter 1 independent operation. (b) The A-phase current of inverter 2 independent operation. (c) The A-phase current of inverter 3 independent operation. (d) The A-Phase output currents (10A/div) of inverters when inverter 2 is connected to grid. (e) The A-Phase output currents (10A/div) of inverters when inverter 3 is connected to grid.*

Fig. 4-30 shows the experimental results of paralleled inverters with same *LCL* filters. The inverter1 operates stably at the beginning. After the inverter2 and inverter3 is activated and connected to grid, the whole system still keeps stable.

Fig. 4-31 shows the experimental results of paralleled inverters with different *LCL* filters. Fig. 4-31(a)-(c) shows that the individual inverter is able to operate stably in weak grid. Fig. 4-31(d)-(e) shows that the inverter1 and inverter 2 can be paralleled stably, once the inverter 3 is activated and connected to grid, the resonance behavior among paralleled inverters will happen [112]. In the case, the participation of inverter 3 cause the system resonance, which agrees with the resonance analysis results from Fig. 4-9-Fig. 4-10.

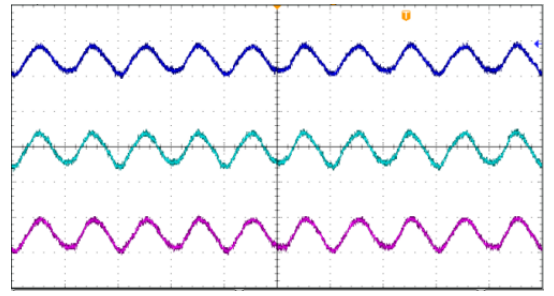

(a)

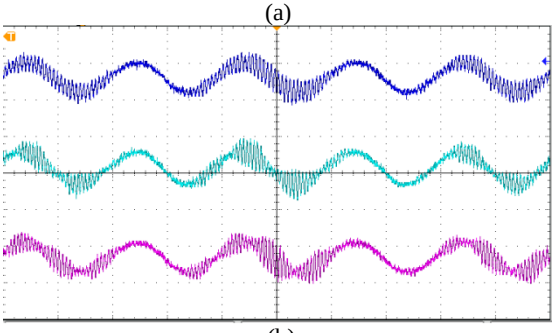

(b)

Fig. 4-32. The experimental results of paralleled inverters with converter-current feedback. ($L_{f1}/L_{f2}/L_{f3}$=3mH/3mH/3mH, $C_{f1}/C_{f2}/C_{f3}$=5uF/10uF/10uF, $L_{c1}/L_{c2}/L_{c3}$=2.6mH/2.6mH/2.6mH) [112]. *(a) The A-phase current of inverters in stable case. (b) The A-phase current of 3 inverters if the 3th inverter operation with underdamping.*

Fig. 4-32 shows the experimental results of paralleled inverters with converter-current feedback. Fig. 4-32(a) shows that the individual inverter can operate stably, even if the inverter 2 and inverter 3 are activated and connected into grid, the system still is stable. Fig. 4-32(b) shows that the underdamping behavior of inverter 3 will cause the oscillation of whole paralleled inverters system, which agrees with the stability analysis from Fig. 4-32.

4.5 CONCLUSION

A state-space-based impedance stability analysis for multiple paralleled grid-connected inverters is presented. State-space model of multiple paralleled grid-connected inverter system is established, where the derivation of equivalent grid impedance looked from each inverter is explained. Furthermore, the resonance origin of paralleled inverters system with grid-current feedback and converter-current feedback is investigated. The proposed method is able to perform stability assessment locally at the connection points of component. Also, the eigenvalue-based participation analysis can be performed to identify the root causes of oscillation modes. The proposed method establishes the bridge between the state-space modelling and impedance stability criterion and combines the advanced merits of the two methods to perform resonance analysis [112]. Simulations and

experimental results are provided to validate the effectiveness of the proposed method.

CHAPTER 5. CONCLUSIONS

The aim of this chapter is to give a summary about the Ph. D project and emphasize the main contributions. The main work and contributions can be described as following.

5.1 Conclusions

(1) A state-space-based harmonic stability analytical method in inverter-interfaced power systems is proposed. An overall state space model combining DG inverters, network dynamics and loads is first developed. Then, harmonic oscillation characteristic is assessed by analyzing eigenvalue traces, where the contribution of each state variable on harmonic oscillation modes is evaluated through participation analysis. In addition, a reduced-order model for harmonic instability analysis is presented according to participation analysis results. The analytical results show that inner current controller, voltage controller and digital control delay have essential effects on harmonic instability in inverter-fed power systems.

(2) A component connection method-based modeling and small-signal stability analysis is proposed for inverter-fed power system. First, the power system is partitioned into different components, and each component is independently modeled. Then, all the component models are assembled to form a composite system model according to terminal interconnection relationship. The terminal characteristic of inverter is investigated by means of frequency response and eigenvalue trace analysis. Finally, an eigenvalue-based approach is proposed to assess low-frequency and high-frequency instability, the influence of controller parameters on small-signal stability are assessed through eigenvalue trace diagram. The analytical results show that both low-frequency and high-frequency instability may happen in inverter-fed power system, which indicates the parameters of multiple control loops have different contributions on instability phenomena in a wide frequency range.

(3) A state-space-based impedance stability analysis for multiple paralleled grid-connected inverters is presented. State-space model of multiple paralleled grid-connected inverter system is established, where the derivation of equivalent grid impedance looked from each inverter is explained. Furthermore, the resonance origin of paralleled inverters system with grid-current feedback and converter-current feedback is investigated. The proposed method is able to perform stability assessment locally at the connection points of components. Also, the eigenvalue-based participation analysis can be performed to identify the root causes of oscillation modes. The proposed method establishes the bridge between the state-space modeling and impedance stability criterion and combines the advanced merits of the two worlds to perform resonance analysis.

5.2 Outlook

In this project, stability assessment methods of inverter-fed power system and paralleled grid-connected inverters have been proposed, which is suitable for different situations. But there are still further topics should be addressed in this research field. On the basis of contributions in this Ph. D project, some potential research topics are given as following.

(1) Stability assessment methods of inverter-fed power system with inverter-fed active load and constant power load should be developed. In modern distribution network, the inverter-fed generators and loads will play important roles. Hence, stability issues should be further investigated. Also, the control technologies for oscillation damping also should be developed.

(2) Although the stability issues have been developed in this project, active damping methods of multiple paralleled grid-connected inverters should be addressed in future research work.

(3) Stability issues with consideration of the intermittent of renewable energy sources should be addressed.

LITERATURE REFERENCE

[1] European Commission, “Europe 2020,” [Online]. Available: http://ec.europa.eu/, Mar. 2010.

[2] J. T. Bialasiewicz, ‘‘Renewable energy systems with photovoltaic power generators: operation and modeling,’’ *IEEE Trans. Ind. Electron*., vol. 55, no. 7, pp. 2752-2758, Jul, 2008.

[3] F. Blaabjerg, R. Teodorescu, M. Liserre, and A. V. Timbus, ‘‘Overview of control and grid synchronization for distributed power generation systems,’’ *IEEE Trans. Ind. Electron*., vol. 53, no. 5, pp. 1398-1409, Oct, 2006.

[4] J. S. Hill, (2015), Mercom Forecasts 2015 Global Solar Installations To Reach 57.4GW [Online], Available: http://cleantechnica.com/2015/06/17/mercomforecasts-2015-global-solar-installations-reach-57-4-gw/.

[5] B. Lehner, G. Czisch, and S. Vassolo, ‘‘The impact of global change on the hydropower potential of Europe: a model-based analysis,’’*Energy Policy*., vol. 33, no. 7, pp. 839-855, May, 2005.

[6] J. S. Hill, (2016), Global Revenue From Solar PV Installations Expected to reach more than 1.2 trillion [Online], Available: https://cleantechnica.com/2016/01/25/global-revenue-solar-pv-installations-expected-reach-1-2-trillion/

[7] Q. Li, W. Chen, Y. Li, S. Liu, and J. Huang, ‘‘Energy management strategy for fuel cell/battery/ultracapacitor hybrid vehicle based on fuzzy logic,’’ *International Journal of Electrical Power & Energy Systems*., vol. 43, no. 1, pp. 514-525, Dec, 2012.

[8] O. Ozgener, and A. Hepbasli, ‘‘Experimental performance analysis of a solar assisted ground-source heat pump greenhouse heating system,’’ *Energy and Buildings*, vol. 37, no. 1, pp. 101-110, Jan, 2005.

[9] O. Ellabban, H. Abu-Rub, F. Blaabjerg, “Renewable energy resources: Current status, future prospects and their enabling technology.” *Renewable and Sustainable Energy Reviews*, Vol.39, November, 2014.

[10] H. Kanchev, D. Lu, F. Colas, V. Lazarov, and B. Francois, ‘‘Energy management and operational planning of a microgrid with a PV-Based active generator for smart grid applications,’’ IEEE Trans. Ind. Electron., vol. 58, no. 10, pp. 4583-4592, Oct, 2011.

[11] R. H. Lasseter, ‘‘Smart distribution: Coupled microgrids,’’ *Proc. IEEE,* vol. 99, no. 6, pp. 1074-1082, Jun. 2011.

[12] Y. Wang, Z. Chen, X. Wang, Y. Tian, Y. Tan, and C. Yang, “An estimator-based distributed voltage-predictive control strategy for AC islanded microgrids,” *IEEE Trans. on Pow. Electron*, vol. 30, no. 7, Jul, 2015.

[13] P. C. Loh, D. Li, Y. K. Chai, F. Blaabjerg, “Hybrid AC-DC Microgrids With Energy Storages and Progressive Energy Flow Tuning ,” *IEEE Transactions on Power Electroncis*, vol. 28, no. 4, Apr, 2013.

[14] J. M. Guerrero, J. Matas, L. G. D. Vicuna, M. Castilla, J. Miret. “Decentralized Control for Parallel Operation of Distributed Generation Inverter Using Resistive Output Impedance.” *IEEE Transactions on Industrial electronics*, vol. 54, no.2, April,2007.

[15] R.H. Lasseter, “MicroGrids.” in Proc. of Power Engineering Society Winter Meeting, 2002.

[16] T. Ackermann, G. Andersson, L. Soder, “Distributed generation: a definition.” Electric Power Systems Research,Vol. 57, no. 3, pp 195–204, April 2001.

[17] F. Blaabjerg, A. Consoli, J. Ferreira, J. D. V. Wyk, “The Future of Electronic Power Processing and Conversion,” *IEEE Transactions on Industry Application*, vol. 41, no. 1, January/Februry 2005.

[18] Q. C. Zhong, ‘‘Robust droop controller for accurate proportional load sharing inverters operated in parallel,*’’ IEEE Trans. Ind. Electron*., vol. 60, no.4, pp. 1281-1290, Apr, 2013.

[19] Y. Wang, Y. Tian, X. Wang, Z. Chen, and Y. Tan, "Kalman-filter-based state estimation for system information exchange in a multi-bus islanded microgrid," in *Proc. 7th IET int. Conf. Power Electron, Mach, Drives*, Apr. 8-11, 2014, pp. 1-6.

[20] Y. Abdel-Rady, I. Mohamed, and E. F. El-Saadany, "Adaptive decentralized droop controller to preserve power sharing stability of paralleled inverters in distributed generation microgrids," *IEEE Trans. Power Electron.*, vol. 23, no. 6, pp. 2806-2816, Nov. 2008.

[21] N. Pogaku, M. Prodanovic, and T. C. Green, "Modeling, analysis and testing of autonomous operation of an inverter-based microgrid," *IEEE Trans. Pow. Electron*., vol.22, pp. 613-625, Mar, 2007.

[22] A. Singh, and A. K. Kaviani, and B. Mirafzal, "On Dynamic Models and Stability Analysis of Three-Phase Phasor PWM-Based CSI for Stand-Alone Applications," *IEEE Trans. Ind Electron.*, vol. 62, no. 5, pp. 2698-2707, May, 2015.

[23] M. Cespedes, L. Xing, and J. Sun, "Constant-power load system stabilization by passive damping," *IEEE Trans. Pow. Electron.*, vol. 26, no. 7, pp. 1832–1836, Jul. 2011.

[24] L. Harnefors, M. Bongiorno, and S. Lundberg, "Input-admittance calculation and shaping for controlled voltage-source converters," *IEEE Trans. Ind. Electron*., vol. 54, no. 6, pp. 3323-3334, Dec, 2007.

[25] B. Wen, D. Boroyevich, P. Mattavelli, Z. Shen, and R. Burgos, "Influence of phase-locked loop on input admittance of three-phase voltage-source converters," in *Proc 28th Annu. IEEE Appl. Power Electron. Conf. and Expo*., 2013, pp. 897-904.

[26] J. H. Enslin, and P. J. Heskes, ''Harmonic interaction between a large number of distributed power inverters and the distribution network,'' *IEEE Trans. Pow. Electron*., vol. 19, no. 6, pp. 1568-1593, Nov, 2004.

[27] X. Wang, F. Blaabjerg, and W. Wu, "Modeling and analysis of harmonic stability in an AC power-electronics-based power system," *IEEE Trans. on Pow. Electron.*, vol. 29, no. 7, Jul, 2015.

[28] X. Wang, F. Blaabjerg, P. C. Loh, "Virtual RC damping of *LCL*-filtered voltage source converters with extended selective harmonic compensation," *IEEE Trans. Power Electron*., vol. 30, no. 9, pp. 4726-4737, Sep, 2015.

[29] IEEE/Cigre Joint Task Force on Stability Terms and Definitions, "Definition and classification of power system stability," *IEEE Trans. Power System*., vol. 19, no. 2, pp. 1387-1401, May, 2004.

[30] P. Kundur, Power System Stability and Control. New York: McGrawHill, 1994.

[31] T. Van Cutsem and C. Vournas, Voltage Stability of Electric Power Systems. Norwell, MA: Kluwer, 1998.

[32] J. M. Guerrero, J. C. Vasquez, J. Matas, L. G. D. Vicuna, and M. Castilla, "Hierarchical control of droop-controlled AC and DC microgrids- A general approach toward standardization," *IEEE Trans. Ind Electron*., vol. 58, no. 1, pp. 158-1033, Feb, 2015.

[33] Y. B. Wang, X. Wang, F. Blaabjerg, and Z. Chen, "Eigenvalue-based harmonic stability analysis method in inverter-fed power systems," in *Proc. of IEEE Industrial Electronics Society 41st Annual Conference*, (IECON, 2015), pp. 3277-3282, 9-12 November, 2015.

[34] Y. B. Wang, X. Wang, Z. Chen and F. Blaabjerg, ''Small-signal stability analysis of inverter-fed power systems using component connection method,'' *IEEE Trans. Smart. Grid* (Early Access).

[35] E. A. A. Coelho, P. C. Cortizo, and P. F. D. Garcia, ''Small-signal stability for parallel-connected inverters in stand-alone AC supply systems,'' *IEEE Trans. Ind. App*., vol. 38, no. 2, pp. 533-542, Mar, 2002.

[36] N. Bottrell, M. Prodanovic, and T. C. Green, "Dynamic stability of a microgrid with an active load," *IEEE Trans. Pow. Electron.*, vol. 28, no.11, pp. 5107-5119, Nov, 2013.

[37] M. Marwali, J. W. Jung, andA.Keyhani, "Stability analysis of load sharing control for distributed generation systems," *IEEE Trans. Energy Convers.*, vol. 22, no. 3, pp. 737–745, Sep. 2007.

[38] B.Wen, D. Boroyevich, P. Mattavelli, Z. Shen, and R. Burgos, "Influence of phase-locked loop on input admittance of three-phase voltage-source converters," in *Proc. 28th Annu. IEEE Appl. Power Electron. Conf. and Expo*., 2013, pp. 897–904.

[39] T. Messo, J. Jokipii, A. Makinen, and T. Suntio, "Modeling the grid synchronization induced negative-resistor-like behavior in the output impedance of a three-phase photovoltaic inverter," in *Proc. IEEE Fourth Intl. Symp. Power Electron. for Distributed* Generations System, 2013, pp. 1–8.

[40] L. Harnefors, M. Bongiorno, and S. Lundberg, "Input-admittance calculation and shaping for controlled voltage-source converters," *IEEE Trans. Ind. Electron*., vol. 54, no. 6, pp. 3323–3334, Dec. 2007.

[41] J. H. Enslin and P. J. Heskes, "Harmonic interaction between a large number of distributed power inverters and the distribution network," *IEEE Trans. Power Electron.*, vol. 19, no. 6, pp. 1586–1593, Nov. 2004.

[42] X. Wang, F. Blaabjerg, Z. Chen, and W. Wu, "Resonance analysis in parallel voltage-controlled distributed generation inverters," in *Proc. Annu. IEEE Appl. Power Electron. Conf. and Expo*., 2013, pp. 2977–2983.

[43] M. Corradini, P.Mattavelli, M. Corradin, and F. Polo, "Analysis of parallel operation of uninterruptible power supplies loaded through long wiring cables," *IEEE Trans. Power Electron.*, vol. 25, no. 4, pp. 1046–1054, Apr. 2010.

[44] S. Zhang, S. Jiang, X. Lu, B. Ge, and F. Z. Peng, "Resonance issues and damping techniques for grid-connected inverters with long transmission cable," *IEEE Trans. Power Electron*., vol. 29, no. 1, pp. 110–120, Jan. 2014.

[45] L. H. Kocewiak, J. Hjerrild, and C. L. Bak, "Wind turbine converter control interaction with complex wind farm systems," *IET Renewable Power Generation*, vol. 7, no. 4, pp. 380–389, Jul. 2013.

[46] E. Mollerstedt and B. Bernhardsson, "Out of control because of harmonics—An analysis of the harmonic response of an inverter locomotive," *IEEE Control Syst. Mag*., vol. 20, no. 4, pp. 70–81, Aug. 2000.

[47] X. Wang, F. Blaabjerg, and P. C. Loh, "Proportional derivative based stabilizing control of paralleled grid converters with cables in renewable power plants," in *Proc. ECCE* 2014, 4917-4924, 2014.

[48] S. G. Parker, B. P. McGrath, and D. G. Holmes, "Regions of active damping control for *LCL* filters," *IEEE Trans. Ind. Application*., vol. 50, no. 1, pp. 424-432, Jan, 2014.

[49] Z. Xin, P. C. Loh, X. Wang, F. Blaabjerg, and Y. Tang, "Highly accurate derivatives for *LCL*-filtered grid converter with capacitor voltage active damping," *IEEE Trans. on Power Electron.*, vol. 31, no. 5, pp. 3612-3625, May, 2016.

[50] Y. Tang, P. C. Loh, P. Wang, F. H. Choo, and F. Gao, "Exploring inherent damping characteristic of *LCL*-filters for three-phase grid-connected voltage source inverters," *IEEE Trans. Power. Electron*., vol. 27, no. 3, pp. 1433-1443, Mar. 2012.

[51] Z. Xin, X. Wang, P. C. Loh, and F. Blaabjerg, "Grid-current-feedback control for *LCL*-filtered grid converters with enhanced stability," *IEEE Trans. on Power Electron.*, vol. 32, no. 4, pp. 3216-32287, Apr, 2017.

[52] M. Liserre, R. Teodorescu, and F. Blaabjerg, "Stability of photvoltaic and wind turbine grid-connected inverters for a large set of grid impedance values," *IEEE Trans. Power. Electron*., vol. 21, no. 1, pp. 263-272, Jan. 2006.

[53] G. Shen, X. Zhu, J. Zhang, and D. Xu, "A new feedback method for PR current control of *LCL*-filter-based grid-connected inverter," *IEEE Trans. Ind. Electron*., vol. 57, no. 6, pp. 2033–2041, Jun. 2010.

[54] F. Cavazzana, P. Xattavelli, M. Corradin, and I. Toigo, "Grid sensitivity considerations on multiple parallel inverters systems." in *Proc. of the 8th International Conference on Power Electronics – ECCE Asia* (ICPE 2016-ECCE Asia), pp. 1-8, 22-26 May, 2016.

[55] M. Lu, X. Wang, P. C. Loh, and F. Blaabjerg, "Interaction and aggregated modeling of multiple paralleled inverters with LCL filter," IEEE Energy conversion congress and exposition (ECCE), 2015.

[56] M. Lu, X. Wang, F. Blaabjerg and P. C. Loh, "An analysis method for harmonic resonance and stability of multi-paralleled LCL-filtered inverters," in *Pro. of the IEEE 6th international symposium on power electronics for distributed generation systems*, (PEDG), 2015, pp. 1-6.

[57] J. Sun, W. Hu, H. Zhou, Y. Jiang, and X. Zha, "A resonant characteristics analysis and suppression strategy for multiple parallel grid-connected inverters with *LCL* filter," *Journal of Power Electronics*., vol. 16, no. 4, pp. 1483–1493, Jul. 2016.

[58] J. L. Agorreta, M. Borrega, J. Lopez, and L. Marroyo, "Modeling and control of *N*-paralleled grid-connected inverters with *LCL* filter coupled due to grid impedance in PV plants," *IEEE Trans. Power Electron*., vol. 26, no. 3, pp. 770-785, Mar, 2011.

[59] M. Lu, X. Wang, P. C. Loh, and F. Blaabjerg, "Resonance interaction of multi-parallel grid-connected inverters with *LCL*-filter," *IEEE Trans. Power Electron*., vol. 32, no. 2, pp. 894-899, Feb, 2017.

[60] Y. B. Wang, X. Wang, Z. Chen, and F. Blaabjerg, "State-space-based harmonic stability analysis for paralleled grid-connected inverters," *in Proc. 42th Annu. Conf. IEEE Industrial Electronics Society*, 2016, pp. 1-6.

[61] S. Lefebver and R. Dube, "Control system analysis and design for an aerogenerator with eigenvalue methods," *IEEE Trans. Power Syst*., vol. 3, no. 4, pp. 1600–1608, Nov. 1988.

[62] J. M. Undrill, "Dynamic stability calculations for an arbitrary number of interconnected synchronous machines," *IEEE Trans. Power Apparat. Syst*., vol. PAS-87, no. 3, pp. 835–845, Mar. 1968.

[63] T. Li, A. M. Gole, and C. Zhao, "Harmonic instability in MMC-HVDC converters resulting from internal dynamics," *IEEE Trans. Power Delivery*., vol. 31, no. 4, pp. 1738–1747, Aug. 2016.

[64] B. Gao, G. K. Morison, and P. Kundur, "Voltage stability evaluation using modal analysis," *IEEE Trans. Power Systems*., vol. 7, no. 4, pp. 1529–1542, Nov. 1992.

[65] L. A. Montestruque, and P. Antsaklis, "Stability of model-based networked control systems with time-varying transmission times," *IEEE Trans. Automatic Control*., vol. 49, no. 9, pp. 1562–1572, Sep. 2004.

[66] D. Hertz, "The extreme eigenvalues and stability of real symmetric interval matrices," *IEEE Trans. Automatic Control*., vol. 37, no. 4, pp. 532–535, Apr. 1992.

[67] Z. Xin, X. Wang, P. C. Loh, and F. Blaabjerg, "Realization of digital differentiator using generalized integrator for power converters,"*IEEE Trans. Power Electron*., vol. 30, no. 12, pp. 6520-6523, 2015.

[68] J. Wang, J. D. Yan, L. Jiang, and J. Zou, " Delay-dependent stability of single-loop controlled grid-conneted inverters with LCL filters," *IEEE Trans. Power Electron*., vol. 30, no. 12, pp. 6520-6523, Feb, 2015.

[69] Y. Zhang, H. Ma, C. Yang, and L. Dong, "Joint scheduling analysis of time-delay impact on networked control system for multi-inverter parallel operation," *in Proc. 36th Annu. Conf. IEEE Industrial Electronics Society*, 2010, pp. 2162-2167.

[70] P. Cortes, J. Rodriguez, C. Silva, and A. Flores, "Delay compensation in model predictive current control of a three-phase inverter," *IEEE Trans. Ind Electron*., vol. 59, no. 2, pp. 1323-1325, Feb, 2012.

[71] Z. Xin, X. Wang, P. C. Loh, and F. Blaabjerg, "Enhanced stability of capacitor-current feedback active damping for LCL-filtered grid converters," in *Pro. of the Energy Conversion Congress and Exposition*, (ECCE), pp. 4729-4736, 2015.

[72] Y. B. Wang, X. Wang, F. Blaabjerg, and Z. Chen, "Harmonic instability assessment using state-space modeling and participation analysis in inverter-fed power systems," *IEEE Trans. Ind Electron*., vol. 64, no. 1, pp. 806-816, Jan, 2017.

[73] J. R. C. Orillaza, and A. R. Wood, "Harmonic state-space model of a controlled TCR," *IEEE Trans. Pow. Delivery.*, vol. 28, no. 1, pp. 197-205, Apr. 2013.

[74] J. B. Kwon, X. Wang, C. L. Bak, F. Blaabjerg, "Harmonic interaction analysis in grid connected converter using harmonic state space (HSS) modeling," *Proceedings of the 30th annual IEEE applied power electronics conference and exposition*, 2015.

[75] J. E. Ormrod, "Harmonic State Space Modelling of Voltage Source Converters," Master, Department of Electrical Computer Engineering, University of Canterbury, 2013.

[76] J. R. Orillaza, M. S. Hwang, and A. R. Wood, "Switching Instant Variation in Harmonic State-Space modelling of power electronic devices," in Universities Power Engineering Conference (AUPEC), 2010 20th Australasian, 2010, pp. 1-5.

[77] R. Middlebrook, "Input filter considerations in design and application of switching regulators," in *Proc. IEEE Ind. Appl. Soc. Annu. Meet.*, pp. 366– 382, 1976.

[78] J. Sun, "Impedance-based stability criterion for grid-connected inverters," *IEEE Trans. Power Electron*., vol. 26, no. 11, pp. 3075-3078, Nov. 2009.

[79] R. Turner, S. Walton, and R. Duke, ''A case study on the application of the nyquist stability criterion as applied to interconnected loads and sources on grids,'' *IEEE Trans. Ind. Electron*., vol. 60, no. 7, pp. 2740-2749, Jul, 2013.

[80] X. Wang, F. Blaabjerg, and P. C. Loh, "An impedance-based stability analysis method for paralleled voltage source converters." in *Proc. of the International Conference on Power Electronics – ECCE Asia* (ICPE 2014-ECCE Asia), pp. 1529-1535, 18-21 May, 2014.

[81] M. Cespedes, and J. Sun, "Impedance modeling and analysis of grid-connected voltage-source converters*," IEEE Trans. Power Electron*., vol. 29, no. 3, pp. 1254-1261, 2014.

[82] W. Du, J. Zhang, Y. Zhang, and Z. Qian, "Stability criterion for cascaded system with constant power load*," IEEE Trans. Power Electron*., vol. 28, no. 4, pp. 1843-1851, 2014.

[83] S. Vesti, T. Suntio, J. A. Oliver, R. Prieto, and J. A. Cobos, "Impedance-based stability and transient-performance assessment applying maximum peak criteria*," IEEE Trans. Power Electron*., vol. 28, no. 5, pp. 2099-2104, May, 2013.

[84] Amr Ahmed A. Radwan, and Yasser Abdel-Rady I. Mohamed, "Assessment and mitigation of interaction dynamics in hrbrid AC/DC distribuion generation systems," *IEEE Trans. Smart Grid*., vol. 3, no. 3, pp. 1382-1393, Sep, 2012.

[85] L. Harnefors, X. Wang, A. G. Yepes, and F. Blaabjerg, "Passivity-based stability assessment of grid-connected VSCs---An overview," *IEEE Journal on emerging and selected topics in power electronics*.

[86] M. Huang, X. Wang, P. C. Loh, and F. Blaabjerg, "LLCL-filtered grid converter with improved stability and robustness*," IEEE Trans. Power Electron*., vol. 31, no. 5, pp. 3958-3967, 2016.

[87] L. Harnefors, A. G. Yepes, A. Vidal, and J. D-Gandoy, "Passivity-based controller design of grid-connected VSCs for prevention of electrical resonance instability," *IEEE Trans. Ind Electron*., vol. 62, no. 2, pp. 702-710, Feb, 2015.

[88] M. Perez, R. Ortega, and J. R. Espinoza, "Passivity-based PI control of switched power converters." *IEEE Trans. Control Systems Technology*., vol. 12, no. 6, pp. 881-890, Nov, 2004.

[89] A. Riccobono, and E. Santi, "Comprehensive review of stability criteria for DC power distribution systems," *IEEE Trans. Ind Application*., vol. 50, no. 5, pp. 3525-3535, Sep/Oct, 2014.

[90] X. Jiang, and A. M. Gole, "A frequency scanning method for the identification of harmonic instabilities in HVDC systems," *IEEE Trans. Power Delivery*., vol. 10, no. 4, pp. 1875-1881, Oct, 1995.

[91] M. Elfayoumy, and C. G. Moran, "A comprehensive approach for sub-synchronous resonance screening analysis using frequency scanning technique," in *Proc. of power tech conference*, pp. 1-5, 23-26 June, 2003.

[92] T. Thiringer, "Frequency scanning for power system property determination – applied to a wind power grid," *IEEE Trans. Power System*., vol. 21, no. 2, pp. 702-708, May, 2006.

[93] B. L. Agrawal, and R. G. Farmer, "Use of frequency scanning techniques for subsynchronous resonance analysis," *IEEE Trans. Power Apparatus and Systems*., vol. PAS-98, no. 2, pp. 341-349, Mar/Apr, 1979.

[94] N. Johansson, L. Angquist, and H. P. Nee, "A comparison of different frequency scanning methods for study of subsynchronous resonance," *IEEE Trans. Power System*., vol. 26, no. 1, pp. 356-363, Feb, 2011.

[95] P. S. B. Nascimento, H. E. P. de. Souza, F. A. S. Neves, and L. R. Limongi, "FPGA implementation of the generalized delayed signal cancelation-phase locked loop method for detecting harmonic sequence components in three-phase signals ,"*IEEE Trans. Ind Electron*., vol. 60, no. 2, pp. 645-658, Feb, 2013.

[96] S. Buso, and P. Mattavelli, Digital Control in Power Electronics. CA, USA: Morgen & Claypool Publishers, 2006.

[97] K. Natori, and K. Ohnishi, "A design method of communication disturbance observer for time-delay compensation, taking the dynamic property of network disturbance into account," *IEEE Trans. Ind Electron*., vol. 55, no. 5, pp. 2152-2168, May, 2008.

[98] Y. Xia, P. Shi, G. P. Liu, D. Rees, and J. Han, "Active disturbance ejection control for uncertain multivariable systems with time-delay," *IET Control Theory & Applications*., vol. 1, no. 1, pp. 75-81, Jan, 2007.

[99] M. K. Kazimierczuk, "Transfer function of current modulator in PWM converters with current-mode control," *IEEE Trans. Circuits and Systems*., vol. 47, no. 9, pp. 1407-1412, Sep, 2000.

[100] H. A. Mohammadpour, and E. Santi, "Modeling and control of gate-controlled series capacitor interfaced with a DFIG-based wind farm," *IEEE Trans. Ind Electron*., vol. 62, no. 2, pp. 1022-1033, Feb, 2015.

[101] A. Kahrobaeian, and Y. A. I. Mohamed, "Analysis amd mitigation of low-frequency instabilityies in autonomous medium-voltage converter-based microgrids with dynamic loads," *IEEE Trans. Ind Electron*., vol. 61, no. 4, pp. 1643-1658, Apr, 2014.

[102] D. Gautam, V. Vittal, and T. Harbour, ''Impact of increased penetration of DFIG-Based wind turbine generators on transient and smalll signal stability of power systems,'' *IEEE Trans. Power Syst*., vol. 24, no. 3, pp. 1426-1434, Aug. 2009.

[103] F. Katiraei, and M. R. Iravani, ''Power management strategies for a microgrid with multiple distributed generation units,'' *IEEE Trans. Power Syst*., vol. 21, no. 4, pp. 1821-1831, Nov. 2006.

[104] D. L. H. Aik, and G. Andersson, "Use of participation factors in modal voltage stability analysis of multi-infeed HVDC systems," *IEEE Trans. Power Delivery*., vol. 13, no. 1, pp. 203-211, Jan, 1998.

[105] G. Gaba, S. Lefebver, and D. Mukhedkar, ''Comparative analysis and study of the dynamic stability of AC/DC systems,'' *IEEE Trans. Power Syst*., vol. 3, no. 3, pp. 978-985, Aug. 1988.

[106] S. Lefebvre, D. P. Carroll, and R. A. Decarlo, ''Decentralized power modulation of multiterminal HVDC systems,'' *IEEE Trans. Power Apparatus and Systems*., vol. PAS-100, no. 7, pp. 3331-3339, Jul. 1981.

[107] S. Arabi, G. J. Rogers, D. Y. Wong, P. Kundur, and M. G. Lauby, ''Small signal stability program analysis of SVC and HVDC in AC power systems,'' *IEEE Trans. Power Syst*., vol. 6, no. 3, pp. 1147-1153, Aug. 1991.

[108] M. A. Choudhry, A. S. Emarah, K. A. Ellithy, and G. D. Galanos, ''Stability analysis of a modulated AC/DC system using the eigenvalue sensitivity approach,'' *IEEE Trans. Power Syst*., vol. PWRS-1, no. 2, pp. 128-136, May. 1986.

[109] H. K. Khalil, "Nonlinear System," 3rd ed. Englewood Cliffs, NJ: Prentice-Hall, 2002.

[110] G. Hou, and V. Vittal, "Trajectory sensitivity based preventive control of voltage instability considering load uncertainties," *IEEE Trans. Power Syst*., vol.27, no. 4, pp. 2280-2288. Nov. 2012.

[111] Y. B. Wang, X. Wang, Z. Chen, and F. Blaabjerg, "Eigenvalue-based impedance stability analysis for multiple paralleled grid-tied inverters system." The 10th International Conference on Power Electronics – ECCE Asia (ICPE 2017-ECCE Asia). (Accepted).

[112] Y. B. Wang, X. Wang, Z. Chen, and F. Blaabjerg, "Frequency scanning-based impedance stability criterion for grid-connected inverters system." The 10th International Conference on Power Electronics – ECCE Asia (ICPE 2017-ECCE Asia). (Accepted).

[113] X. Feng, J. Liu, and F. C. Lee, "Impedance specifications for stable DC distributed power systems," *IEEE Trans. Power. Electron*., vol. 17, no. 2, pp. 157-162, Mar. 2002.

[114] D. Yang, X. Ruan, and H. Wu, "Impedance shaping of the grid-connected inverter with LCL filter to improve its adaptability to the weak grid condition," *IEEE Trans. Power. Electron*., vol. 29, no. 11, pp. 5795-5805, Nov. 2014.

[115] F. Wang, J. L. Duarte, M. A. M. Hendrix, and P. F. Ribeiro, " Modeling and analysis of grid harmonic distortion impact of aggregated DG inverters," *IEEE Trans. Power Electron*., vol. 26, no. 3, pp. 786-797, Mar, 2011.

ISSN (online): 2446-1636
ISBN (online): 978-87-7112-971-7

AALBORG UNIVERSITY PRESS